MONTAN
UNIVERSITÄT
LEOBEN

Chair of Geology and Economic Geology

Master's Thesis

Sulfide Geochemistry of the Hohen Tauern Historic Gold Districts (Austria)

Eileen Göbel, B.Sc.

September 2024

MONTANUNIVERSITÄT LEOBEN
www.unileoben.ac.at

AFFIDAVIT

I declare on oath that I wrote this thesis independently, did not use any sources and aids other than those specified, have fully and truthfully reported the use of generative methods and models of artificial intelligence, and did not otherwise use any other unauthorized aids.

I declare that I have read, understood and complied with the "Good Scientific Practice" of the Montanuniversität Leoben.

Furthermore, I declare that the electronic and printed versions of the submitted thesis are identical in form and content.

Date 18.09.2024

Signature Author
Eileen Göbel

ACKNOWLEDGEMENT

This project was written in collaboration with Geosphere Austria at the Chair of Geology and Economic Geology at Montanuniversität Leoben. First of all, I would like to thank my supervisor Dr. Phillip Gopon, not only for the great support and expertise, but also for always being understanding and kind throughout this whole process. Your enthusiasm always gave me a push forward in finishing this thesis. I would also like to thank Dr. Thomas Angerer from Geosphere Austria for his support and expertise specifically during the sampling campaigns in July and October 2023. Lots of thanks especially to Geosphere Austria who financed the project and the master thesis through the VLG funding scheme and thus made it possible for me to be part of this project.

I would also like to thank the staff of the Chair of Geology and Economic Geology and the Chair of Resource Mineralogy at Montanuniversität Leoben. Therefore, thanks to Dr. Viktor Bertrandsson Erlandsson for showing me how to use and for carrying out the LA-ICP-MS measurements. Also, many regards to Dr. Monika Feichter for all the good words and the performance of all the EPMA mappings. I want to thank Prof. David Misch and Gerhard Hawranek for giving me the opportunity to use the shared SEM of the Chair of Energy Geosciences and the Department of Material Science. Finally, I am grateful to Dr. Robert Arato for his patience and help in creating illustrations via Python.

The path to completing my master's thesis and thus the end of my studies was not always easy. That's why the people close to me, such as friends and family, also deserve a word of gratitude. Thank you to all my friends who have always given me good advice and for distracting me when I needed it. Many thanks to my family for their backup, emotional support and the opportunity to shape my own life. Above all, I would like to thank you Dad, not only for the financial support that made my studies possible, but also for the patience and trust you put in me. Most importantly, I would like to express my greatest appreciation to you, Richard! Thank you, for your never-ending support and sacrifices during this time. Whenever I felt lost, you were there for me, supporting me and motivating me not to give up.

ABSTRACT

The Hohe Tauern mountains in Austria are both historically and scientifically significant. They play a special role in the evolution of the Alps and the evolution of geologic knowledge related to mountain building processes. The ore deposits in the Hohen Tauern are significant in the evolution of our knowledge of the formation of gold deposits, as well as having been one of the largest sources of revenue for the Archbishopdom of Salzburg and later the Austrian Empire.

The gold mineralization in the Hohen Tauern mountains is associated with the uplift of the mountain range and can be generally characterized as vein hosted orogenic gold. Gold occurs as electrum and the host rocks vary widely, but are often high-grade metamorphic rocks, especially orthogneisses. Sulfide minerals are known to be associated with the gold mineralization but have generally been understudied and underappreciated as a potential carrier of gold.

These sulfides minerals within the mineralization, as well as the exposed nappes of the Penninic Ocean and the European continental margin, provide the opportunity to better understand the development of the Alpine orogeny and the ore deposits therein. The sulfide mineral pyrite is a common sedimentary, metamorphic, and hydrothermally formed mineral. Its ubiquitousness as well as its unique ability to incorporate an array of trace elements (ex. Au, Ag, As Co, Cu, Ga, Ge and Ni) makes it a crucial record of a number of geologic processes, especially the formation of ore deposits.

This thesis investigates the sulfide geochemistry of the historic gold districts in the Hohen Tauern mountains, with a focus on the geochemistry of pyrite and gold. The aim is to provide a regional comparison of the sulfide minerals associated with the gold mineralization, in the hopes of better understanding these deposits in a more wholistic fashion as well as the relationships between the individual deposits. Special attention is paid to understanding the morphology of the pyrite, its relationships with other ore minerals, and its association with the gold mineralization.

By analyzing 24 samples from 12 mining districts with a combination of reflected light microscopy, scanning electron microscopy, laser ablation inductively coupled plasma mass spectrometry, and electron probe microanalysis, this work offers insights into the trace element composition of pyrite and gold. The findings contribute to understanding the origin of the mineralizing fluids, potential correlations between the trace elements in gold and pyrite, and the complex nature of the region's metallogenic history.

KURZFASSUNG

Die Hohen Tauern in Österreich sind sowohl historisch als auch wissenschaftlich bedeutsam. Sie spielen eine besondere Rolle bei der Entstehung der Alpen und bei der Entwicklung des geologischen Wissens über Gebirgsbildungsprozesse. Die Erzvorkommen in den Hohen Tauern sind für die Entwicklung unseres Wissens über die Entstehung von Goldvorkommen von Bedeutung und waren eine der größten Einnahmequellen für das Erzbistum Salzburg und später für das österreichische Kaiserreich.

Die Goldmineralisierung in den Hohen Tauern steht im Zusammenhang mit der Hebung des Gebirges und kann im Allgemeinen als orogene Goldadern charakterisiert werden. Das Gold kommt als Elektrum vor, und die Wirtsgesteine variieren stark, sind aber oft hochgradige metamorphe Gesteine, insbesondere Orthogneise. Es ist bekannt, dass Sulfidminerale mit der Goldmineralisierung in Verbindung stehen, aber im Allgemeinen wurden sie als potenzielle Goldträger nicht ausreichend untersucht und gewürdigt.

Diese Sulfidminerale innerhalb der Mineralisierung sowie die freiliegenden Decken des penninischen Ozeans und des europäischen Kontinentalrandes bieten die Möglichkeit, die Entwicklung der alpinen Orogenese und die darin enthaltenen Erzlagerstätten besser zu verstehen. Das Sulfidmineral Pyrit ist ein weit verbreitetes sedimentäres, metamorphes und hydrothermal gebildetes Mineral. Seine Allgegenwärtigkeit sowie seine einzigartige Fähigkeit, eine Reihe von Spurenelementen (z. B. Au, Ag, As, Co, Cu, Ga, Ge und Ni) einzubinden, machen es zu einem wichtigen Zeugnis einer Reihe geologischer Prozesse, insbesondere der Bildung von Erzlagerstätten.

In dieser Arbeit wird die Sulfidgeochemie der historischen Goldvorkommen in den Hohen Tauern untersucht, wobei der Schwerpunkt auf der Geochemie von Pyrit und Gold liegt. Ziel ist es, einen regionalen Vergleich der mit der Goldmineralisierung assoziierten Sulfidminerale zu erstellen, in der Hoffnung, diese Lagerstätten in einer ganzheitlicheren Weise sowie die Beziehungen zwischen den einzelnen Lagerstätten besser zu verstehen. Besonderes Augenmerk wird auf das Verständnis der Morphologie des Pyrits, seiner Beziehungen zu anderen Erzmineralien und seiner Verbindung mit der Goldmineralisierung gelegt.

Durch die Analyse von 24 Proben aus 12 Bergbaurevieren mit einer Kombination aus Auflichtmikroskopie, Rasterelektronenmikroskopie, Massenspektrometrie mit induktiv gekoppeltem Plasma und Elektronensondenmikroanalyse bietet diese Arbeit Einblicke in die Spurenelementzusammensetzung von Pyrit und Gold. Die Ergebnisse tragen zum Verständnis des Ursprungs der mineralisierenden Flüssigkeiten, möglicher Korrelationen zwischen den Spurenelementen in Gold und Pyrit und der komplexen Natur der metallogenen Geschichte der Region bei.

TABLE OF CONTENTS

1. INTRODUCTION

The Hohe Tauern is a geological masterpiece. Due to their geological and tectonic structure, the Hohe Tauern have been, and continue to be, the focus of interest for geoscientists. The exposed nappes of the Penninic Ocean and the European continental margin provide a unique opportunity to better understand the development processes of the Alpine orogeny. Mining of rich ore bodies, associated with the uplift of the Hohe Tauern, played a significant historic role in the region. As early as the 6th century BC, people were aware of the presence of valuable minerals such as gold and exploited them (Moosleitner, 1994).

1.1 HISTORICAL BACKGROUND

The first uses of Tauern gold date back to 600 BC from relicts containing gold from graves of the salt workers on the Dürrnberg close to Hallein provide evidence for this (Hartmann, 1978; Moosleitner, 1994). Spectral analysis, a method to determine the chemical composition of solids, of these artefacts showed that they were possibly made with Tauern gold (Hartmann, 1978). It is believed that the gold was extracted from places deposits in gold-bearing streams. Finds of molds for gold ingots made of marble on the Magdalensberg indicate that gold was mined in Roman times (Ertl, 2007). It is believed that gold and silver were mined in the Fuschertal by slaves under Roman administration as early as 15 BC (Brandmaier, 1989). The focus here was on the supergene altered zones in which the precious metals were already enriched and easier to process. There was an increase in gold mining in the Gastein Valley until the 14th century due to the production of placer gold in streams by the Count of Pleistein (Brandmaier, 1989). The mines of the Sonnblick group were apparently brought into operation in 719. Since then, Tauern gold was increasingly important for the use of gold coins in the Alps (Ertl, 2007). In 1342, the first mining regulations were issued by the Archbishop of Salzburg, in which many legal issues were dealt with. From this century onwards, the primary deposits, i.e. the solid rock, began to be mined. Mining in the Gastein and Rauris areas in particular experienced a massive boom during this time (Cech, 2015).

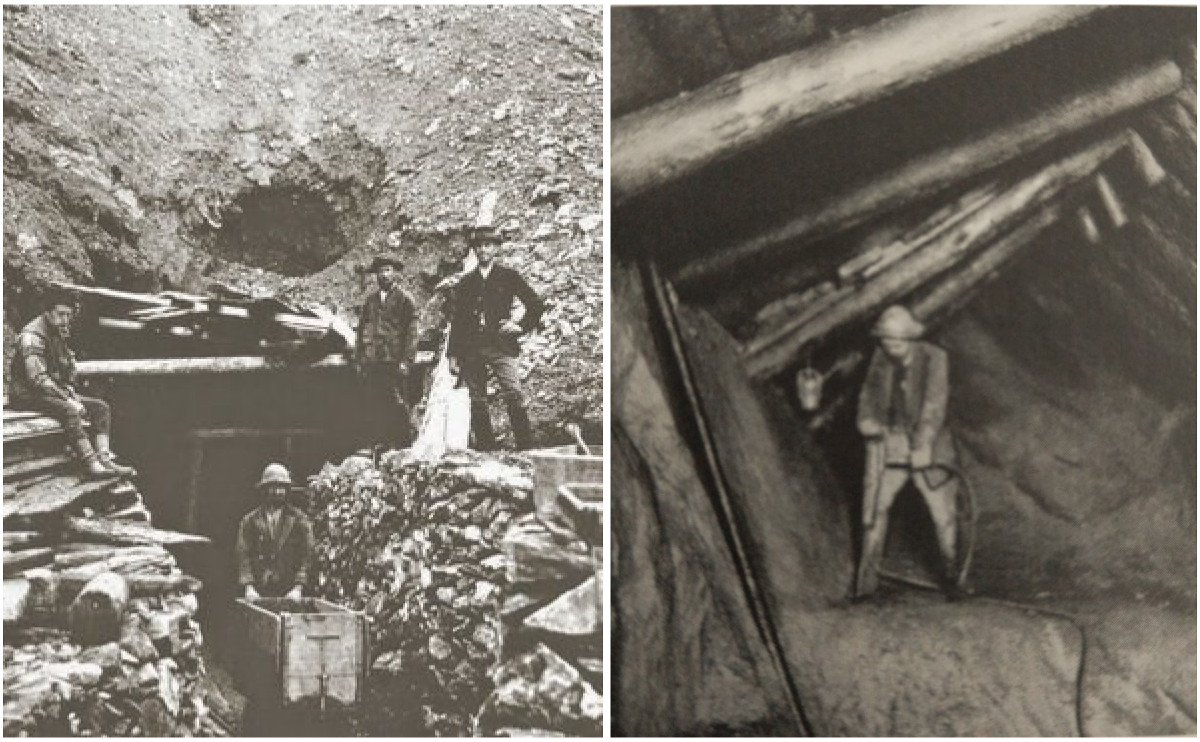

Figure 1: Left: Construction of the Augustinerstollen (Hohen Goldberg) in 1906. Right: Mining the ore body using jackhammers in the deeper level of the Geißler vein in the Georg adit mining area (Imhof adit) in 1914 (Paar et al., 2006)

The Hirzbach and Schiedalpe mining districts in the Fuschertal reached their first productive phase between 1460 and 1550. The gold and silver ores were extracted from underground mines. While the mines in the Fuschertal had a declining profitability up from 1550, technical innovations in terms of transportation and the smelting process led to a second heyday around 1557 in the Gastein and Rauris mining districts. This second boom led to an annual production of up to 830 kg of gold and 272 kg of silver (Brandmaier, 1989; Paar et al., 2006). Shortly afterwards, however, there was a steady decline in production numbers, with an average of just 10 g of gold and 50 g of silver being extracted per ton of mine output at Radhausberg in 1850. In the 20th century, attempts were made to put some mining districts back into operation, but without long-term success. Finally, in the 19th century, all mining in the Hohe Tauern came to a standstill (Cech, 2015).

1.2 GEOLOGICAL SETTING

1.2.1 GEOLOGY OF THE ALPS

In general, the Alps can be divided into four major geological units: 1) The Austroalpine, a composite nappe system originating from the distal passive continental margin of the Adriatic plate; 2) The Helvetic, which represents the European continental margin and mainly consists of shallower basement slices and décolled cover units; 3) The Penninic can be divided into relicts of the Valais Ocean and the Piemont-Liguria Ocean and represents the oceanic crust as well as the overlaying oceanic sediments; 4) The Southern Alps, a minor, shallower and non-metamorphic part of the Adratic plate, separated from the other three units by the Periadriatic lineament. (Höck et al., 1994; Piaz et al., 2003; Schuster et al., 2013). These subdivisions are dominated by diverse paleogeographic features that were assimilated at various phases of Alpine tectonic evolution, creating unique geological structures and geomorphology (Schuster et al., 2013).

Put simply, the Alpine mountains are a result of a more or less continuous subduction of the Adriatic plate under the European plate followed by a continent-continent collision (Höck et al., 1994; Schuster et al., 2013). The During the Jurassic period, around 165 million years ago, between the European plate in the north and the Adriatic plate in the south and east the Penninic Ocean (Alpine Tethys) formed as a continuation of the early Atlantic Ocean (Schuster and Stüwe, 2010). Volcanism led to the formation of a mid-ocean ridge resulting in the formation of an oceanic crust (Höck et al., 1994). This represented the depositional area for some of the rocks found largely in the central and western alps and the Hohen Tauern (Höck et al., 1994; Schuster and Stüwe, 2010). The eastward movement of the African Plate and thus the northward movement of the Adriatic Plate led to the formation of rift systems during the Lower Cretaceous and to the formation of the Valais Ocean. This also caused the Iberia-Brianconnais microcontinent to split off from the European plate, dividing the Penninic Ocean into the Valais Ocean (North Penninic Ocean) in the north and the Piedmont-Liguria Ocean (South Penninic Ocean) in the south (Schmid et al., 2013; Schuster and Stüwe, 2010; Walter, 2016). The extension was followed by a collisional phase, in which the oceanic crust was subducted beneath the continental plate consisting of the Austroalpine nappe stack and successively led to the closure of the Penninic Ocean about 50 million years ago (Höck et al., 1994; Schmid et al., 2013; Schuster and Stüwe, 2010). In the process, the oceanic crust, as well as parts of the European continental margin, were subducted to depths of up to 60 km (Höck et al., 1994; Schuster and Stüwe, 2010).

In this process, the rocks of the Penninic Ocean were pushed over the European and overthrust by the eastern Alps (Höck et al., 1994; Piaz et al., 2003; Schmid et al., 2013; Schuster and Stüwe, 2010). Just about 30 million years ago, the subducted lithospheric plate broke off, leading in an uplift of the asthenospheric mantle forming melts that intruded upwards to form the Periadriatic Plutons. After the slab break-off of the European plate, the NE-directed subduction of the Adriatic plate under the young Alps began (Schmid et al., 2013; Schuster and Stüwe, 2010).

The Helvetic and Penninic nappes are mainly exposed in the Swiss Central Alps as well as in the French-Italian Western Alps. In the Eastern Alps, these units are only found in a few so-called geological windows, including the Tauern Window. The Helvetic nappes can also be found in a few scales and layers of moderate thickness in the north of the Eastern Alps (Höck et al., 1994; Schmid et al., 2004). The alpine orogeny can be divided into two phases. First, the Eoalpine orogenic episode at around 80-90 Ma in which a E-SE dipping subduction zone (subducting the Penninic Ocean under the European Plate) formed (Fitzsimons and Veit, 2001; Pfiffner, 1992). Second, the Neoalpine orogeny which took place during the Late Eocene and Oligocene in which the Adriatic and European Plates collided due to N-S plate movements. During this period the Alpine Tethys vanished and the Alps began to be lifted (Fitzsimons and Veit, 2001).

1.2.2 GEOLOGY OF THE TAUERN WINDOW

With a length of around 160 km and a width of 40 to 60 km, including the mountain ranges of the Hohen Tauern and the Zillertal Alps, the Tauern Window is by far the largest tectonic window in the Eastern Alps. It represents the largest tectonic occurrence of the Penninic in the Eastern Alps (Höck et al., 1994; Pestal, 2005). In the Tauern Window, the exposed nappes represent the European continental margin as well as the Alpine Thethyan oceans (Bertrand et al., 2017). In an older categorization, the Tauern were divided into two tectonic units: the central gneisses and the schistose shell. The schistose shell, in turn, was divided into five distinct formations. Frasl (1958) classifies the schist shell into (1) Altkristallin, (2) Habachserie, consisting of a black slate ophiolite series, (3) Wustkogelserie, (4) Triadic carbonate rock series and (5) Bündnerschieferserie which contains ophiolites.

Schmid (2013) redefined the classification of the Tauern window and split it into three units: the Venediger duplex, the Subpenninic nappes (units derived from the distal European margin), and the Penninic nappes (Figure 2).

The Venediger duplex consists of (1) the Variscan Basement which was refed formerly to as the “Altes Dach.” It is build up of Variscan and pre-Variscan metamorphic formations older than the Zentralgneise (central gneiss). (2) The Permo-Carboniferous intrusions which represent the central gneiss of the different nappes including the Göss, Tux-Granatspitz, Hochalm, Zillertal-Riffl, Sonnblick-Romate and Mureck-Storz nappes. They are post-Variscan in age (310-270 Ma) and discordantly intrude Variscan and/or older metamorphic formations. The intrusions were only overprint by the Alpine orogeny. The only exception is the “Zentralgneis” of the Ahorn nappe which intruded more likely during the Variscan orogeny. (3) The post-Variscan cover, also referred to as the “Untere Schieferhülle” (lower schist cover). It consists of late Carboniferous to Permo-Triassic sediments such as clastic continental sediments which are intercalated with meta-volcanic layers, deposited in small basins (Schmid et al., 2013).

The Subpenninic nappes represent the distal European margin and is divided into the Wolfendorn nappe, the Eclogite zone, and the Modereck nappe system. The Eclogite zone is structurally located between the Venederiger duplex laying above and the Modereck nappe system laying below. It formed due to the subduction of the most distal European passive continental margin which reached depths of at least 80km. Since this nappe contains also layers and lenses of mafic eclogites, it is likely that mafic intrusions existed at the most distal margin at the continent-ocean transition (Schmid et al., 2013).

The Penninic nappes, which consists of oceanic lithosphere fragments, include the Matrei Zone, the Reckner Ophiolithic Complex and the Glockner Nappe System. (Favre and Stampfli, 1992; Lammerer and Weger, 1998; Schmid et al., 2013). The Glockner nappe system mainly comprises relicts of the Valais Ocean. The Reckner ophiolite complex consists of sequences derived from the Piemont-Liguria-Ocean~~,~~ overlain by Jurassic radiolarites and younger pelagic sediments. This complex underwent blueschist facies metamorphism, during Early Cenozoic (Schmid et al., 2013).

At the contact between the Tauern Window to the Austroalpine units, we find the Matrei zone. It represents an accretionary prism that formed during the subduction of the Piemont-Liguria-Ocean in front and below the Austroalpine. Peak metamorphic conditions in this unit, range from blueschist facies in the south to greenschist facies in the north. The heterogenous lithology comprises calcareous-clayey sediments, mafic-ultramafic rocks with pelagic cover, and sediments from the Adriatic margin (Schmid et al., 2013).

The exhumation of the Tauern Dome, which occurred for most of the Miocene, was primarily controlled by upright folding and erosion processes (Bertrand et al., 2017). During the Miocene, the exhumation rates of the western subdome where faster compared to the eastern subdome until after 6 Ma where the exhumation rates became similar and slowed down (Bertrand et al., 2017). Several metamorphic events can be observed in the rocks of the Tauern Window. The metamorphic events of the Variscan orogeny, which range from greenschist-facies to amphibolite-facies, can be dated to an age of approx. 300 to 320 million years (Höck et al., 1994; Schmid et al., 2013). The Alpine orogeny led to a wide range of metamorphic imprints, which can be divided into three distinct metamorphic events. The first one lead to the formation of Mesozoic eclogites. Based on the magnesium and iron distribution between garnet and clinopyroxene, pressures of 20 kbar and temperatures ranging from 550 to 600°C could be reconstructed (Höck et al., 1994; Schmid et al., 2013). The second event is characterized by the formation of blueschists, which, however, can only be detected in a few rocks.

Petrographic investigations indicate that this event is younger than the eclogite formation and probably occurred at pressures and temperatures of 7-9 kbar and 450°C. The third and most recent formative event is the greenschist to amphibolite-facies metamorphism, which overprint the entire Tauern Window (Höck et al., 1994). The degree of metamorphism increases from the edge to the center, which is confirmed by indicator minerals. The maximum temperature conditions for the greenschist facies ranged between 400 and 450°C, whereas the amphibolite facies reached up to 550°C. (Frank, 1987; Höck et al., 1994). The pressure conditions varied between 4-8 kbar, corresponding to a depth of 12-20 km (Höck et al., 1994).

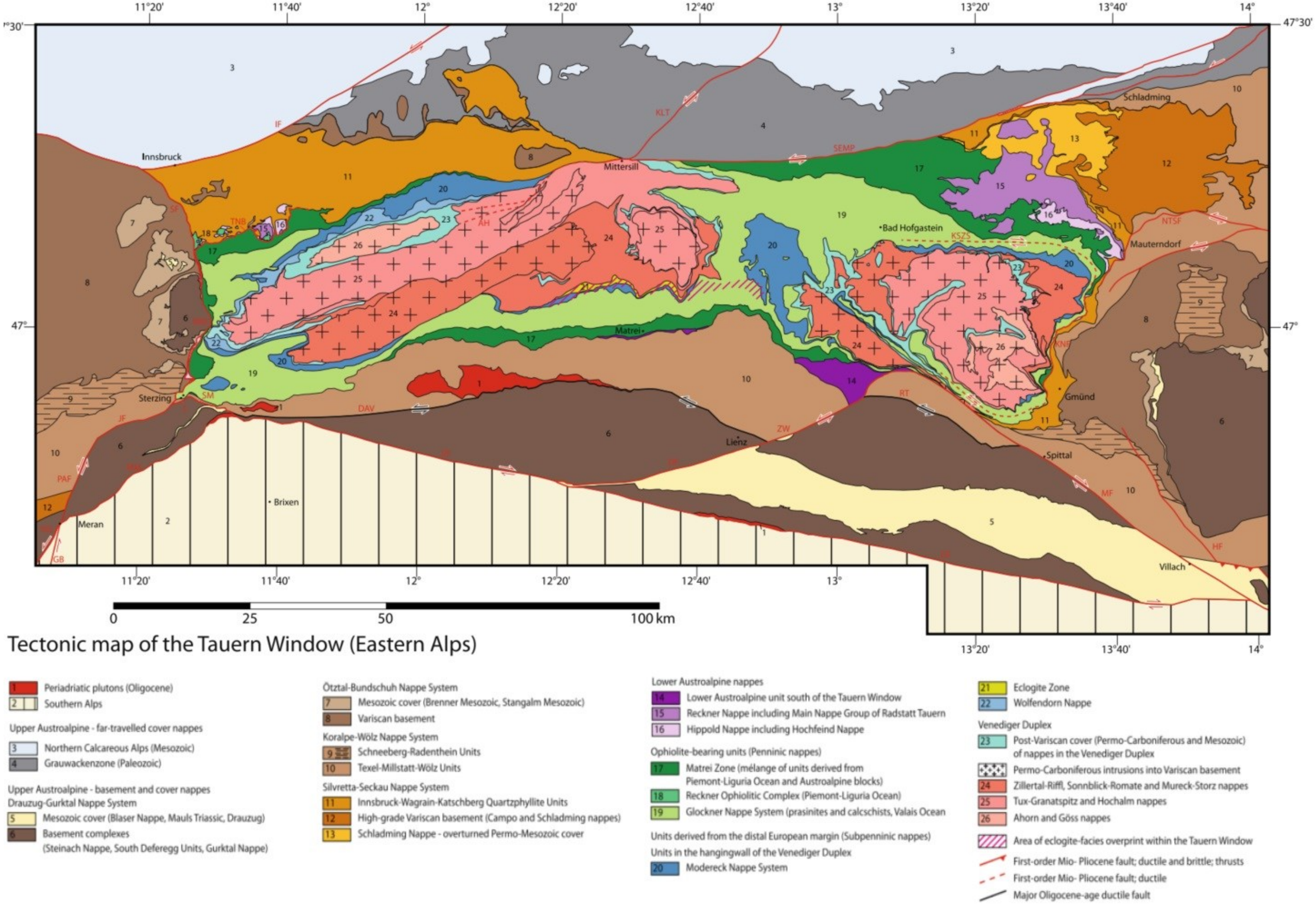

Figure 2: Tectonic map of the Tauern window, representing the different nappes (Schmid et al., 2013).

The tectonic evolution of the Tauern Window can be described with several stages starting with the subduction of the Piemont-Liguria Ocean under the Adratic plate (Austroalpine) and formation of an accretion wedge of oceanic material. Followed by the subduction of the Valais-Ocean including the Glockner nappe system as well as parts of the most distal European margin (Eclogite zone and parts of the Modereck nappe system) under the Adriatic plate (Schmid et al., 2013). Emplacement onto the European margin led to isoclinal folding between the Glockner nappe system and the Modereck nappe system, as well as exhumation of the high-pressure units and initial accretion of European crust. The breaking off of the subducted European plate and formation of the Venediger duplex were followed by the Tauern crystallization, locally reaching amphibolite facies (0.3-1 GPa und ca. 500-700ºC). Finally, the start of the Adratic slab subduction and indentation of the southern alpine into the Eastern alps resulted in a N-S shortening of the Tauern Window north of the Peradriatic line. Additional subduction of the southern alpine lithospheric base under the eastern alps led to rapid doming as well as lateral extrusion on the eastern alps (Schmid et al., 2013).

1.2.3 DEPOSIT GEOLOGY

The mesothermal mineralized Tauern gold veins, which formed 30 million years ago during the cooling phase of alpine regional methamorphism, tend to strike NNE-SSW and have a steep (70-85°) dip to the ESE (Bergmaier, 1991; Brandmaier, 1989; Paar et al., 2006). These mineralized shear zones can sometimes be traced for several kilometers at the surface (Brandmaier, 1989). The alteration zones of the host rocks surrounding these veins are just a few meters thick. (Bergmaier, 1991; Brandmaier, 1989). The vein fillings are almost always polymineralic and rarely monomineralic (Paar et al., 2006). The most frequently encountered minerals are sulfides such as pyrite, arsenopyrite, galena, chalcopyrite, pyrrhotite and sphalerite (Bergmaier, 1991; Brandmaier, 1989). Many other incidental and accessory minerals can also be observed, such as Pb-Ag-Bi sulfosalts, marcasite, electrum and polybasite (Bergmaier, 1991; Brandmaier, 1989; Paar et al., 2006). Other minerals encountered can be found in the literature mentioned. The gold veins reach thicknesses of a few centimeters, up to 3 meters (Bergmaier, 1991).

Basically, the former mining ore or gold veins can be categorized into several areas. These include Hirzbach-Schiedalpe, Kloben and Pasterze as the westernmost province of the Tauern gold veins of the central Hohe Tauern (Brandmaier, 1989). The Gastein-Rauris area, which from west to east consists of the Goldzeche, Hoher Goldberg, Siglitz-Bockhart-Erzwies and Radhausberg districts and from a geological point of view is part of the Sonnblick Group (Exner, 1964; Paar et al., 2006). The Rotgülden district, which occupies a special position compared to the others, as the precious metal deposits are largely bound to the marbles of the Silbereck Formation. Only a small part can be found in the central gneisses of the Hölltor-Rotgüldenkern (Friedrich, 1934; Paar et al., 2006). The last and easternmost district, Schellgaden, shows some differences to the classic Tauern gold veins and thus represents a separate type in terms of formation history (Friedrich, 1935; Friedrich and Matz, 1939; Paar et al., 2006).

1.2.3.1 Western area

In contrast to the other districts, these have no connection to the rocks of the Venediger duplex but lie exclusively within the Mesozoic shale cover (Penninic and subpenninic nappes; Brandmaier, 1989). The Kloben, Schiedalpe, Hirzbach and Mesenatten districts are located within dark and light-colored phyllites, some of which are chlorite-bearing (Brandmaier, 1989; Weber et al., 2019). The latter district is located at the edge of the Modereck nappe system and is also widely carbonate-bearing; talc schist and brown ankeritic schist with nodules of the light green mica mineral fuchsite (Cr-mica) can be found. Eclogitic rocks, prasinite and serpentinite can also be found near the western end of the small stream (Cornelius and Clar, 1939; Griesmeier, 2021; Weber et al., 2019) . However, only a few literatures are available in relation to the Mesenatten district. The Fuscher Wegscheide district lies within the Modereck nappe system and, in contrast to the other surrounding districts, represents a silver-rich Pb-Zn deposit localized in limestone and dolomite marble and cellular dolomite (Cornelius and Clar, 1939; Paar et al., 1978). The microstructure is typical for oxidation or cementation zones of Ag-bearing Pb-Zn mineralization, with galena, sphalerite and sulfosalts as primary components (Paar et al., 1978). The Pasterze district is surrounded by calcareous mica schists, prasinite and amphibolite, rocks of the Glockner nappe (Weber et al., 2019). The mineralized quartz veins exposed in front of the glacier tongue are probably part of the deposit, which was mined around 1446 before the “glaciation” (Cornelius and Clar, 1935, 1939). These quartz veins contain only sparse amounts of pyrite and chalcopyrite (Cornelius and Clar, 1939). However, the exact location of the former mine has not yet been determined, but it is assumed that the exposed quartz veins continue under the glacier and that this glacier also covers the traces of the former mine (AKK Ackerbau-Ministerium, 1895; Canaval, 1896; Cornelius and Clar, 1939).

1.2.3.2 Gastein-Rauris

From west to east, this area includes the Hochwurten, Goldzeche, Hoher Goldberg, Siglitz-Bockhart-Erzwies and Radhausberg districts. From a geological perspective, these are located within the

Sonnblick-Romate nappe, which is part of the Venediger Duplex and is divided into two parts by the Mölltal fault (Exner, 1964; Schmid et al., 2013). The host rocks of the Siglitz-Bockhart-Erzwies and Radhausberg districts are part of the Romate nappe, while those of the Goldzeche, Hochwurten and Hoher Goldberg districts belong to the Sonnblick nappe (Griesmeier, 2021; Kreuss, 2021). The main rock of the Romate nappe is the so-called Siglitz gneiss, a fine- to medium-grained hybrid granite gneiss with albite as the dominant component and distinct banking (Bergmaier, 1991; Kreuss, 2021). The main rock of the Sonnblick-nappe is a porphyritic granite gneiss with characteristic potassium feldspar eyes up to centimeters in size (Feitzinger, 1989; Feitzinger and Paar, 1991; Kreuss, 2021). In the Erzwies area, the gneiss is overlain by Upper Jurassic marble and calcareous mica schist with a shallow, northern dip (AKK Ackerbau-Ministerium, 1895; Griesmeier, 2021). A change in mineralization can also be observed within this district. In the lower part of the Erzwies the mineralized veins are rich in pyrite and arsenopyrite with increased gold contents which are similar to the mineralization of Siglitz while in the upper, last third of the Silberpfenning the mineralization of galena and sphalerite becomes richer with higher silver content and lower gold content (AKK Ackerbau-Ministerium, 1895; Feitzinger and Paar, 1991; Vavtar, 1982). In addition to the gneisses at the Hoher Goldberg, Goldzeche and Hochwurten districts, there are also occasional elongated amphibolite nodules. In the area of the Hoher Goldberg, paragneiss nodules are also present (Feitzinger, 1989; Griesmeier, 2021; Paar et al., 2006). The mineralogical composition and the quantity ratio of the ores often vary considerably within individual districts, with particular fluctuations in the precious metal content. For example, different types of ore can be found within the Radhaus district. A distinction can be made between *Derbkiese*, which consists mainly of pyrite and arsenopyrite with fluctuating precious metal contents, *Quarzkiese*, which contains fine inclusions of chalcopyrite, galenite and pyrite in quartz and *Glaserz* a blue-grey quartz which contains finely impregnated silver-containing Bi-Pb sulfosalts, galenite and the highest gold contents (Paar and Topa, 1998; Paar et al., 2006; Posepny, 1880). These special glass ores are not only to be found on the Radhausberg, but also in other districts of the Hohe Tauern (Paar and Topa, 1998).

1.2.3.3 Rotgülden

The Rotgülden mining district is a special case compared to the others, as it is the only one geologically bound to a large extent to the metasediments of the Silbereck formation, which is part of the post-Variscan cover (Horner et al., 1997; Paar et al., 2006). These mainly include marble, calcareous mica schist and black schist (Häusler et al., 1995; Horner et al., 1997; Paar et al., 2006). The metasediments are underlain by granite gneisses and migmatites of the Hölltor-Rotgüldenkern (Exner, 1982). The deposits of the Rotgülden district are characterized by high silver contents in visible gold, a dominance of arsenopyrite, paragenesis with non-ferrous metals of which chalcopyrite is locally very enriched and frequent occurrence of silver-lead-bismuth sulfosalts (Horner et al., 1997; Putz, 2000; Putz et al., 2003). It should be emphasized that the quantity of pyrrhotine is increased in the marbles, while it occurs less frequently in the gneisses. (Paar et al., 2006; Putz et al., 2003). The most important silver carriers of this deposit are silver-rich sulfosalts such as Freibergite, but also other silver-lead-bismuth sulfosalts (Horner et al., 1997; Paar et al., 2006; Putz et al., 2003).

1.2.3.4 Schellgaden

The ore deposits in Schellgaden are located in the easternmost part of the Tauern window within the Storz-Kareck complex, consisting of highly dispersed paragneiss, migmatites and amphibolite (Exner, 1971; Häusler et al., 1995). Based on structural conditions, four ore types can be distinguished. Ore type 1 is characterized by concordant quartz mylonites and generally consists of a large number of sulfide-bearing quartz layers, which are often only a few cm thick. This type of mineralization shows in particular ore enrichments in the fold cores and is the dominant one within the distribution area (Amann et al., 1997; Paar et al., 2006). Ore type 2 is quite similar to the first, but has coarser-grained gold and considerable amounts of tourmaline (Amann et al., 1997; Paar et al., 2006). Ore type 3 is characterized by discordant quartz veins, wherein the sulfides tend to be distributed in nests and coarse-grained gold being present (Amann et al., 1997; Paar et al., 2006). Ore type 4 represents feldspar-bearing sulfide deposits, which are only found in the Knappenstube (Amann et al., 1997; Paar et al., 2006). A special feature of this deposit is the rarity of bismuth minerals and the absence of arsenopyrite, which is abundant in all other Tauern gold veins (Amann et al., 1997; Friedrich, 1968; Krenn et al., 2011). In addition, microscopic gold tellurides occur which act as gold carriers (Paar et al., 2006). Other frequently identified minerals are pyrite, pyrrhotite, chalcopyrite, galenite, scheelite and sphalerite (Friedrich, 1968). It is assumed that this type of deposit is older than the others in the Hohe Tauern, but there is structural evidence that parts of the mineralization are of Alpidic age (Amann et al., 1997; Krenn et al., 2011).

1.3 MINERAL GEOCHEMISTRY

1.3.1 PYRITE

Pyrite (FeS_2) belongs to the metal sulfides, a group of common minerals with a high economic. It is the most abundant sulfide mineral in the earth's upper crust and is found in numerous geological settings

(Deer et al., 2013; Rickard and Luther, 2007). Pyrite is a cubic mineral with a NaCl-type structure and a unit-cell edge of ~ 5.42 Å. As seen in Figure 3 the S atoms are arranged as disulfide groups, placed at the midpoints of cube edges and at the cube´s center, while the Fe(II) atoms are located at the corners and face centers (Deer et al., 2013; Ramdohr and Strunz, 1967; Rickard and Luther, 2007).

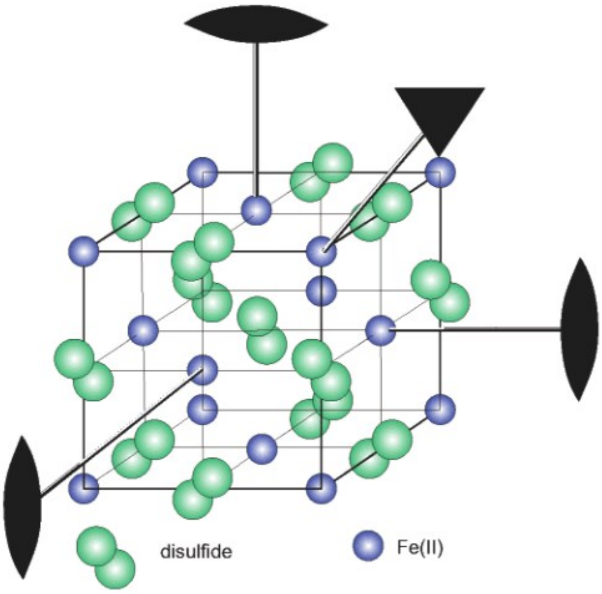

Figure 3: Crystal structure of Pyrite (Rickard and Luther, 2007).

Pyrite has a Mohs hardness of 6 - 6.5 and a density of 4.95 - 5.02 g/cm^3. The mineral, colloquially called "fool's gold" (z.Dt.” Katzengold”), is easy to identify macroscopically in rocks due to its morphology, metallic luster and pale brass or golden yellow coloration. Microscopically, pyrite is easy to recognize due to its high reflectivity and pale-yellow color. Although it is cubic, a subtle anisotropy can often be recognized which is caused by several different possibilities, such as impurities (Deer et al., 2013; Ramdohr and Strunz, 1967). Not only does pyrite have a wide range of stability over a broad pH and temperature range up to 742 °C at low pressure (Craig et al., 1998), but it also forms almost everywhere where S_2^{2-} activity is present and reducing conditions enable the presence of iron(II) (Rickard and Luther, 2007).

Pyrite is suitable as an indicator of the fluid development of a hydrothermal system not only because of its extraordinary stability to pressure, temperature and fluid chemistry changes, but also because of its high growth rates and ability to act as a sink for many elements (Deditius et al., 2011; Keith et al., 2016; Mukherjee and Large, 2016; Palenik et al., 2004). The iron sulfide associated elements such as Au, Ag, As, Bi, Co, Cr, Cu, Hg, Ni, Pb, Sb, Se, Te and Zn can be incorporated in the crystal lattice in solid solution and/or as nanoparticles or nanoinclusions (Deditius et al., 2011, 2009, 2008; Ramdohr and

Strunz, 1967; Reich et al., 2013, 2005). Some of these elements show an isovalent substitution for Fe^{2+} (including Co, Ni, Cu, Zn, Hg and Pb), isovalent substitution for S (including As, Sb, Te) or are incorporated into the crystal structure by complex substitution mechanism that are often unassociated with Fe (Deditius et al., 2008; Gopon et al., 2019; Xie et al., 2024).

Arsenian pyrite, an arsenic-rich pyrite, can contain up to a few weight percent amounts of As and can contain, compared to “normal” pyrite, additional trace elements like W, U and significant amounts of Au (Cook and Chryssoulis, 1990; Reich et al., 2005). In pyrite, arsenic can both substitute iron as a cation (As^{2+} or As^{3+}) or replace sulfur in the crystal lattice as an anion (As^{-}). This depends on the Eh values and the O_2 activity present in the fluid during crystallization (Deditius et al., 2008). In most sulfide deposits, reducing conditions prevail, meaning that As tends to occur as a anion, and more readily replaces for the S- is replaced by As-. This in turn causes the S-S bonds within the pyrite lattice to break, resulting in point defects and local charge within the crystals structure (Gopon et al., 2019; Keith et al., 2018; Reich et al., 2005). Even if arsenian pyrite is of economic and scientific interest due to its often-higher content of gold and other important metals, it also poses a significant risk to humans and the environment. This is due to the fact that arsenic is harmful to health and carcinogenic, especially As^{3+}, the most toxic form of arsenic, which can substitute for Fe ($(Fe, As^{3+}) S_2$) (Deditius et al., 2008; Smith and Smith, 2004). As pyrites beak down under oxidizing conditions the As which is not incorporated as As^{3+} oxidizes to such as well. It is assumed that this can also form at very low temperature conditions in sedimentary-diagenetic and groundwater systems and is therefore a source of arsenic pollution (Deditius et al., 2008).

1.3.2 GOLD

Gold has a very high value in our society due to its excellent materials properties including high electrical conductivity, non-corrosive and non-toxic behavior. It is a siderophile element with a Mohs hardness of 2.5 - 3 (most ductile element) and a density of 19.3 g/cm^3 for pure gold (with a higher silver content, the density also falls to approximately 16 g/cm^3 (Ramdohr, 1975). With its electron configuration Xe $4f^{14}5d^{10}6s^1$, the element also holds a special position in row 11 of the periodic table and can be present in various oxidation states (-1, 0, +1, +2, +3, +4, +5 and +6), with Au^+ and Au^{3+} being the most common oxidation states in nature (Foster and Seward, 1991; Pokrovski et al., 2019).

Gold can be put in solution as a complex. This depends on several factors such as pH, temperature, pressure, salinity, acidity redox conditions and H_2S fugacity (Pokrovski et al., 2019). The most important ligands include $S_2O_3^{2-}$, HS^- and Cl^-, with the HS^- ligand being common for a range of deposit type formation (Foster and Seward, 1991; Pokrovski et al., 2019; Williams-Jones et al., 2009; Zhu et al., 2011).

$Au(HS)_2^-$ and $AuHS^0$ are the dominant aqueous phase at temperatures up to 350°C, an almost neutral to slightly acidic environment, reducing conditions and the presence of adequate HS- with $AuHS^0$ occurring preferably under more acidic conditions (Stefánsson and Seward, 2004; Williams-Jones et al., 2009; Zhu et al., 2011). If there is insufficient H_2S available, the hydrolyzed species $AuOH \cdot H_2O$ is formed. However, in the case of saline and oxidizing waters, like those forming porphyry copper-gold deposits, $AuCl_4^-$ or $AuCl_2^-$ (under somewhat less oxidizing and acidic conditions) is preferably formed, which are particularly stable at temperatures above 350°C (Figure 4) (Williams-Jones et al., 2009). $Au(S_2O_3)_3^{3-}$ can also form in fluids that are oxidizing often as a result of oxidation of sulfides leading to the remobilization of gold (Vlassopoulos and Wood, 1990; Williams-Jones et al., 2009). This complex plays a particular role in the supergene solubility of gold (Williams-Jones et al., 2009).

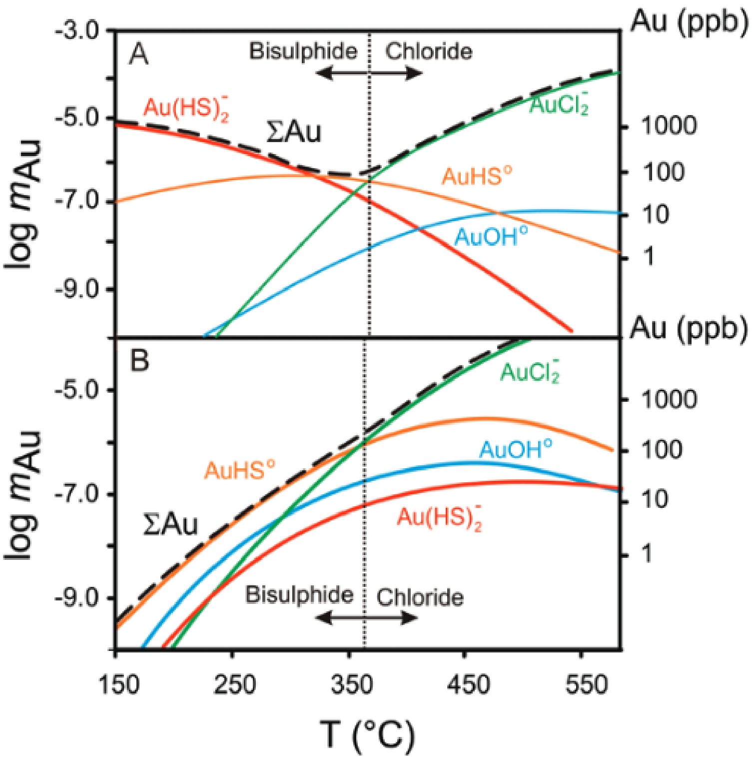

Figure 4: Gold solubility at 1000 bar as a function of temperature for an aqueous solution containing 1.5 molal (m) NaCl and 0.5 m KCl. (A) ΣS (total S) = 0.01 m and f O2 (oxygen fugacity) is buffered by the assemblage hematite–magnetite. (B) ΣS and fO2 are buffered by the assemblage pyrite–pyrrhotite–magnetite (Williams-Jones et al., 2009).

There are several possibilities for gold precipitating, such as boiling, sulfidation or cooling. In the case of $AuCl_4^-$ / $AuCl_2^-$, an increase in pH, a reduction in Cl^- activity and oxygen fugacity leads to a deposition of gold. In addition, this complex is very susceptible to temperature drops, which also lead to gold precipitation (Gibert et al., 1998; Williams-Jones et al., 2009). However, this is different for $Au(HS)_2^-$ / $AuHS^0$. In general, all processes that reduce the activity of reduced sulfur in the hydrothermal ore solution, including the deposition of sulfide minerals, boiling, mixing and oxidation, consequently lead to the precipitation of gold (Foster and Seward, 1991; Gibert et al., 1998; Williams-Jones et al., 2009; Zhu et al., 2011). The most common ways to achieve the reduction of HS^- activity is by boiling and/or the mineralization of sulfide minerals. Boiling promotes the removal of reduced sulfur from the fluid by fractionating H_2S into the vapor and precipitation of base metal sulfides (Foster and Seward, 1991; Williams-Jones et al., 2009). The same can be achieved by fluid mixing with oxygenated meteoric water which can lead to the oxidation of H_2S and HS^- to sulfur and sulphate, resulting in a reduction of the activity (Foster and Seward, 1991). The importance of sulfidation in relation to gold mineralization, is particularly well known in the case of Carlin-type gold deposits. Pyritization by hydrothermal alteration leads to a reduction of sulfur in the fluid and thus to the precipitation of gold (Williams-Jones et al., 2009). These often As bearing Pyrites extract solid solution Au^+ from hydrothermal fluids through adsorption (Zhu et al., 2011).

Whether precipitation occurs also depends partly on the host rock. Carbonate rocks often do not show any visible gold mineralization such in the case of the gold-quartz veins at Brusson, Val d'Ayas in NW. Italy, as the fluid-host rock interaction dissolves calcium carbonate, leading to an increase of pH (Diamond, 1986). However, as the pH increases, the stability of the $Au(HS)_2^-$ complex and thus the solubility of the gold increases as seen in Figure 5 (Foster and Seward, 1991; Pokrovski et al., 2019).

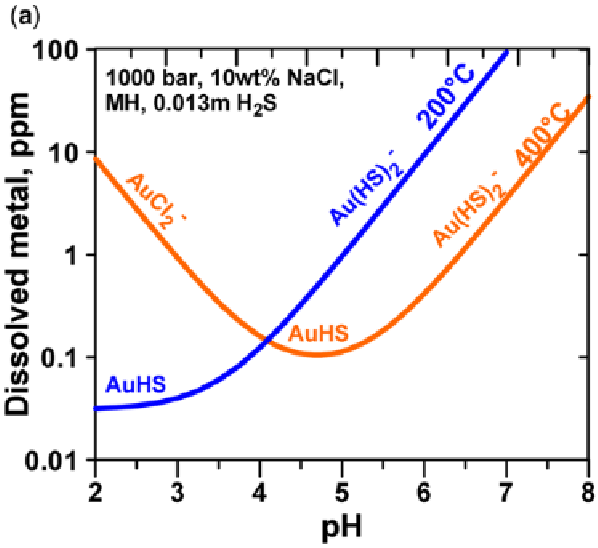

Figure 5: Solubility of native gold as a function of pH at 1000 bar in equilibrium with the magnetite-hematite assemblage and 0.013 m H_2S in solution (Pokrovski et al., 2019).

1.4 GOAL

The aim of this thesis is to carry out a regional comparison of the sulfide and gold mineralization of the eastern Hohe Tauern. Special attention will be paid to the pyrite and their trace elements. In addition, attention will be paid to how the morphology and degrees of intergrowth of the mineral phases are developed and with which minerals the gold is associated. A further aim is to be able to make an estimation on the origin of the fluids that led to the mineralization. Furthermore, the extent to which the trace element chemistry of the sulfide’s changes depending on the surrounding rock is tried to be identified as well as a rough estimation about the mineralization generations. In this study, 26 samples from 14 different former mining districts will be examined using reflected light microscopy, scanning electron microscopy, LA-ICP-MS and EMPA.

2. METHODS

2.1 SAMPLING

Nine of the samples to be analyzed were collected as part of two sampling campaigns (July and October 2023) in the Hohe Tauern. A total of 76 specimens of various sizes were collected from ten different mining districts. The designation of the samples begins with "**PM**", followed by the name of the mining district (eg. **R**adhaus**B**erg) and the sample number (eg. **03**). The two sampling campaigns were accompanied by Dr. Phillip Gopon and Dr. Thomas Angerer. Terrain-compatible tablets with the programs Fieldmove and QField were used to document the sampling.

2.1.1 SAMPLING JULY 2023

The first sampling campaign took place in mid of July for four days. The main focus was sampling multiple mining districts selected with the aid of the Interactive Raw material Information System [IRIS] of the Geosphere Austria (Weber et al., 2019) of the eastern Hohen Tauern including Radhausberg, Mallnitz area (Laserzen/Breitschitzen and Dösener Alm), Pasterze, Palik, Mesenatten and Fuscher Wegscheide/Hochtor. Figure 6 below shows the points of the samples taken and the corresponding mining districts.

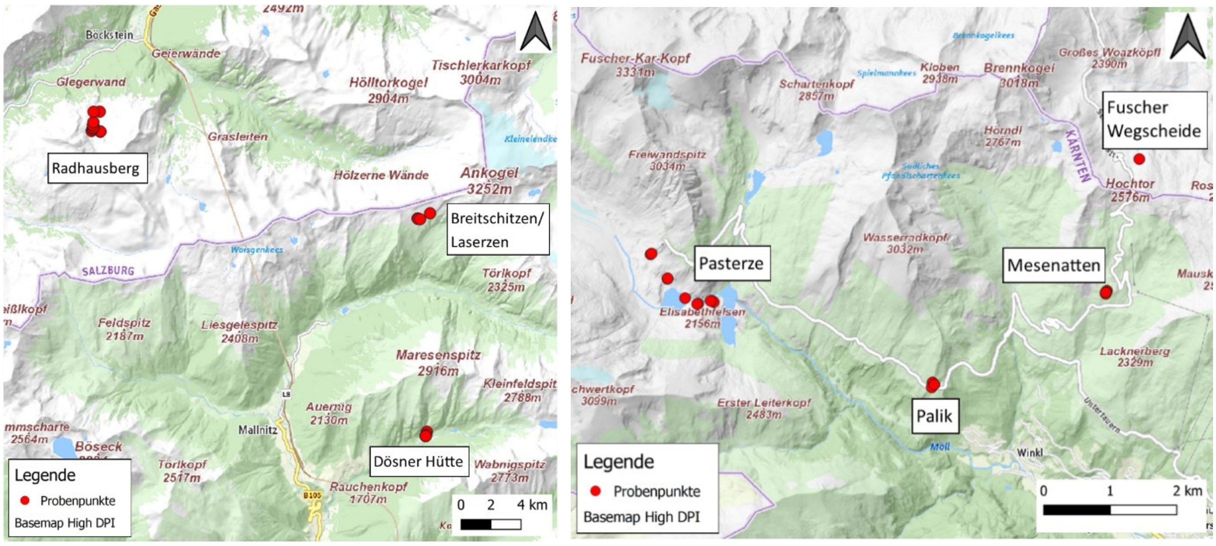

Figure 6: Maps of the sample locations (marked by the red spots) within the different mining districts. Left: Radhausberg and Mallnitz area. Right: Pasterze and Hochtor area (map basis: basemap.at).

2.1.2 SAMPLING OCTOBER 2023

The second sampling campaign took place in the end of October for four days. The main focus was the sampling of different mineralized veins within the Imhofstollen, close to Sportgastein, and finding an adit in the Siglitz mining district to sample the same mineralization within the adit. In addition, the area of the Wasinger E district was also explored and sampled. Figure 7 below shows the points of the samples taken and the corresponding mining districts.

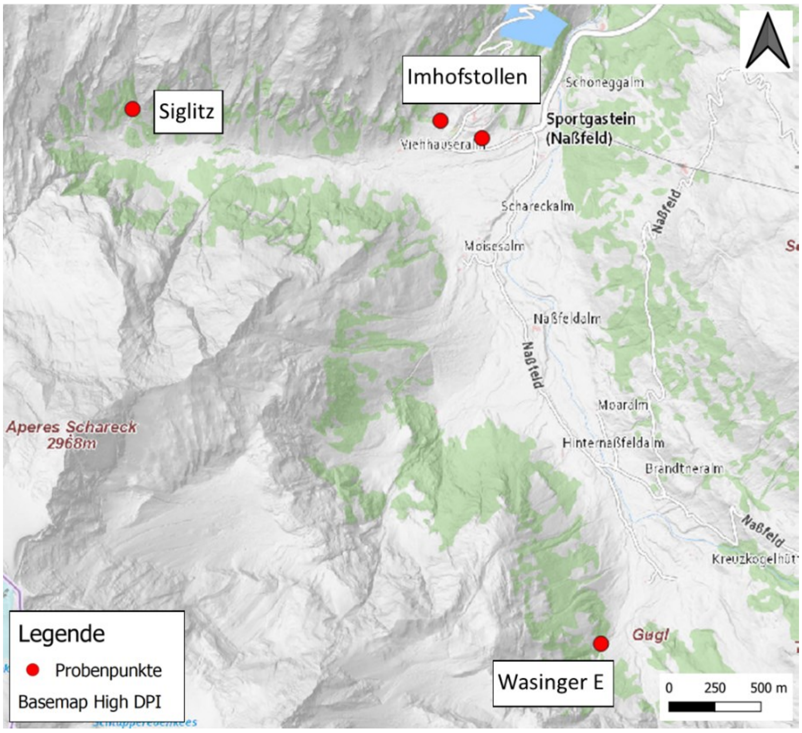

Figure 7: Map of the sample locations (marked by the red spots) of the different mining districts within the Naßfeld valley (map basis: basemap.at).

2.1.3 SAMPLE PREPARATION

The samples were prepared at the Montanuniversität Leoben lab by first cutting the specimens into a 10 – 17 mm thick slices. The area of interest has been marked and the slice has been cut into a round disc with a maximum diameter of 40 mm using a Unipree saw with a diamond embedded blade. These have been imbedded into epoxy and sequentially polished with a 9µm, 3µm and finally 1µm polycrystalline diamond suspension. In total for this thesis 24 samples were analyzed, thereof seven samples are selected from the two sampling campaigns, two samples are from the bachelor thesis of Dominik Kumertz and 15 samples from the Paar-collection (Table 1). Figure 8 displays a geological map showing the mining districts that are included in this thesis.

Table 1: List with Sample ID, mining district, location, sampler, and description of the sample type. Samples of the Paar collection have no distinct coordinates and are described to originate by a mine waste facility.

Sample ID	Mining district	Latitude	Longitude	Sampler	Type
PM-RB-04a	Radhausberg	47.064738	13.100527	Eileen Göbel	Waste dumps
PM-RB-07		47.063763	13.099774	Eileen Göbel	Waste dumps
PM-IM-03	Imhofstollen	47.061951	13.051263	Eileen Göbel	Adit
PM-PA-02	Pasterze	47.070454	12.751332	Eileen Göbel	Float sample
PM-PA-05B		47.067354	12.760402	Eileen Göbel	Outcrop
PM-MS-02	Mesenatten	47.056586	12.803362	Eileen Göbel	Outcrop
PM-SZ-01	Siglitz	47.062537	13.029265	Eileen Göbel	Mineralized vein
21TG27	Bockhart	47.082088	13.038512	Dominik Kumertz	Waste dumps
21TG57		47.082418	13.038047	Dominik Kumertz	Waste dumps
II/873b	Fusch	Paar-collection of the Montanuniversität Leoben (no coordinates or further information available)			Waste dumps
PM-RG-01	Rotgülden				Waste dumps
PM-RG-03					Waste dumps
A1979	Schellgaden				Waste dumps
A1870					Waste dumps
A1514	Hirzbach-Schiedalpe				Waste dumps
A1510					Waste dumps
A1742	Erzwies				Waste dumps
A1740					Waste dumps
A1462	Goldzeche				Waste dumps
A1463					Waste dumps
PM-HW-01	Hochwurten				Waste dumps
A1758					Waste dumps
A1370	Hoher Goldberg				Waste dumps
A1373					Waste dumps

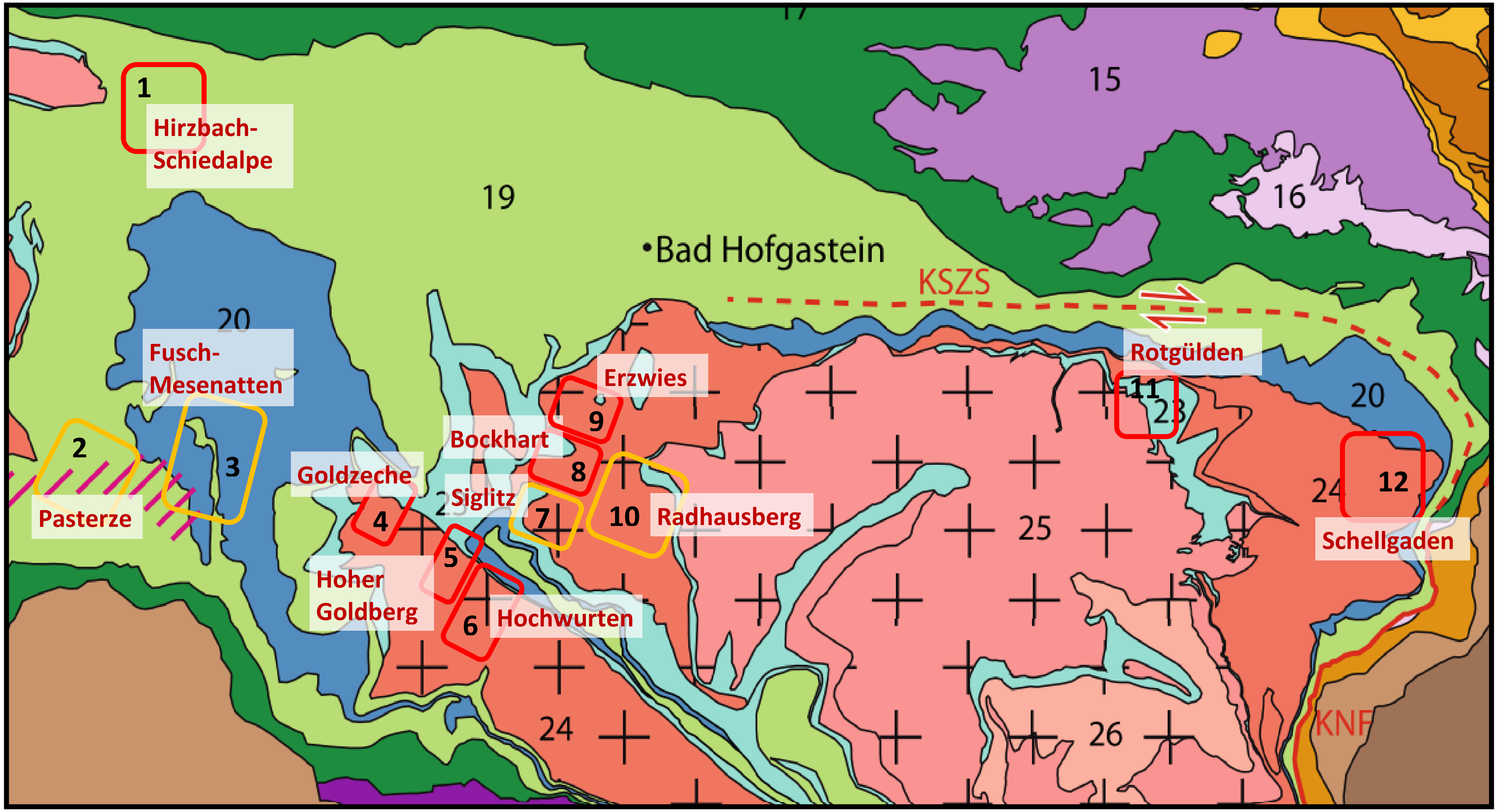

Figure 8: Geological map of the eastern Tauern Window showing the old mining district which are included in this thesis. The Yellow marked squares indicate the districts where samples have been taken as part of the thesis, whereas the red squares represent the districts where the samples were provided by others.

2.2 PETROGRAPHY

2.2.1 REFLECTED LIGHT MICROSCOPY

The reflected light microscopy was used for the identification of minerals which were opaque in thin section, using transmitted light microscopy like mostly ore minerals. In this method, light is projected onto the sample, with a tungsten filament lamp as the most common source. Alternatively, a Xenon discharge lamp can be used. A polarizer is needed to receive liner polarized light. Also, an analyzer is important for further observations. The Illuminator aperture diaphragm is set to field of view to minimize scattering and maximize the contrast.

Minerals can be identified by observing different properties like optical properties either by using plane polarized light or crossed polarizers or properties dependent on the hardness and dependent on structure and morphology. By using only plane polarized light different optical properties can be observed. The color in which a mineral phase appears is dependent on the illumination, on the microscope and the sensitivity on an individual’s eye. Minerales can also appear in slightly different color varieties depending on the mineral phases surrounding it (Gribble, 2012). The reflectance (R) represents the “brightness” of a mineral, the percentage of light reflected from the surface. It can net be measured with the eye, therefor the reflectance value is an estimation by comparison with R of other known common mineral phases. Isotropic opaque minerals like cubic crystals as well as basal sections of non-cubic crystals, have only one reflectance value, no matter the orientation. Whereas, with non-cubic minerals the reflected light is split up into two mutually perpendicular linearly polarized beams whereby these minerals show a change in R (bireflectance) or a change in color (reflection pleochroism) when rotated (Craig and Vaughan, 1994). The same applies under crossed polarizers where color and brightness of non-cubic minerals may change with rotation. Minerals of intermediate opacity may show internal reflection due to light which may penetrate the crystal and be reflected back from below (Gribble, 2012). Observing the polishing hardness helps identifying different mineral phases where due to resistance of a mineral to abrasion (difference in hardness) a polishing relief is formed which can be observed with the kalb light line.

A Leica Polyvar microscope has been used for the detailed optical petrography. A Keyence VHX 6000 digital microscope with the objectives Z20 and Z100 provided by the Chair of Geology and Economic Geology at Montanuniversität Leoben was used to create the detailed images used in this thesis, as well as the panorama overview pictures.

2.2.2 SCANNING ELECTRON MICROSCOPY (SEM)

By using a focused high-energy beam of electrons, the Scanning Electron Microscope (SEM) produces images of the sample. Thereby the electron beam is scanned in a vacuum the surface of the specimen in a raster pattern. When the electrons hit the sample, various signals can be detected and used to create the images (Figure 9). The signals used in this study are backscattered electrons and characteristic X-rays (Zhou and Wang, 2007). To prevent charging of the sample during electron irradiation, the samples were coated a ~20nm layer of graphite.

In case of detecting backscattered electrons some electrons of the primary electron beam are scattered through a large angle by an elastic collision with the specimen's atomic nucleus and leave the surface with an energy that exceeds 50eV. As seen in Figure 9 the signal originates at a shallower depth than the characteristic X-ray. Depending on the atomic number of each element, 10-50% of the primary electrons are backscattered toward their source (Zhou and Wang, 2007).The higher the mean atomic number of the material, the more electrons that get backscattered. This gives the image a higher level of contrast (Vernon-Parry, 2000).

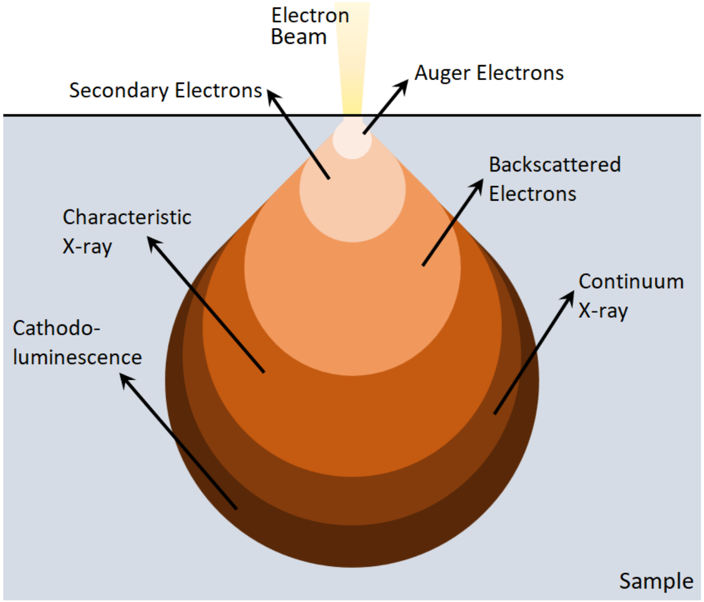

Figure 9: Illustration of the specimen-bean interaction volume with depths from which each signal type may be emitted (Göbel, 2022).

The characteristic X-rays that are emitted during electron bombardment, are used to analyze the specimen and to provide the chemical composition of each mineral. When an inner shell electron gets knocked out by a primary electron, an electron from the outer shell falls into the inner orbit. The result is the emission of an X-ray which can be detected and is specific to a given transition in an element

(Zhou and Wang, 2007). In the case of this thesis the SEM has been used to identify the Minerals within each polished section, small inclusions which are barely visible using a reflected light microscope as well as a rough elemental composition of some Minerals. Additionally, it has been used to identify zonations within the Pyrites.

For scanning electron microscopy (SEM), a Zeiss Evo MA 10 SEM coupled with a Bruker Quantax energy dispersive (EDS) detector at the Chair of Geology and Economic Geology at the Montanuniversität Leoben was used. Electron voltage used was between 15-20kV with beam current between 0.1-1 nA. Backscattered electrons and characteristic X-rays were used to determine the minerals chemical composition. Additionally, a field emission sourced SEM Tescan Clara with SE/BSE imaging and an Oxford Instruments EDS system was used at the Chair of Material Science at the Montanuniversität Leoben.

For the SEM analysis, all polished sections have been coated with an approximately 20 nm thick film of carbon by using a Polaron Emitech K950X sputter coater.

2.2.3 LASER ABLATION (LA-ICP-MS)

The laser ablation inductively coupled plasma mass spectrometry (LA-ICP-MS) is a very versatile method with a high sensitivity. A typical LA-ICP-MS system, as shown in Figure 10, mainly consists of a pulsed laser, an optical microscope an airtight sampling cell, a transport line, an air plasma, ion lenses and a quadrupole mass spectrometer (Durrant, 1999; Koch and Günther, 2017). The functionality is quite simple. A pulsed laser beam is focused on the surface of the solid sample causing a small part of the sample to be ablated. The released particles get transported with an inert carrier gas through the transport line into the plasma of the ICP unit, where the particles get vaporized and ionized. A mass spectrometer, either a multi-collected or quadrupole, is then used to filter and detect the masses of interest (Sindern, 2017; Ulrich et al., 2009).

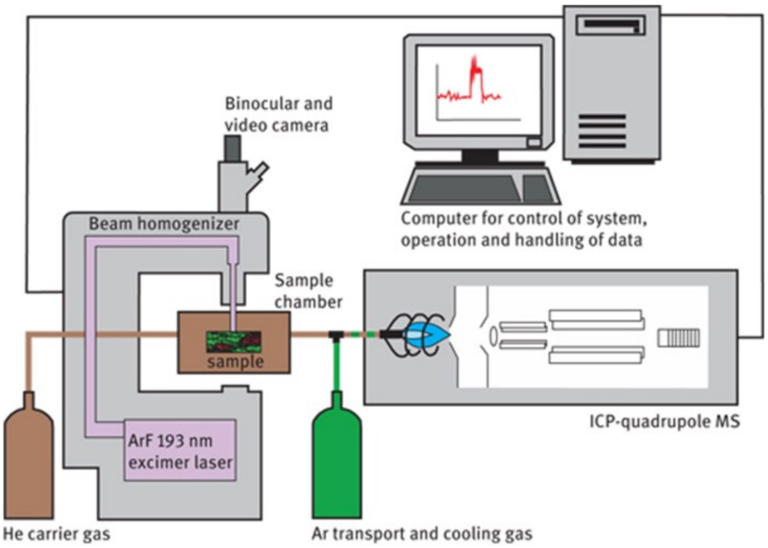

Figure 10: Schematic structure of a common LA-ICP-MS device (Sindern, 2017)

Different variables influence the interaction of the laser and the solid, like the wavelength and energy of the laser. The shorter the wavelength, the higher the ablation rate but the lower the fractionation. The most common and widely used lasers are use a Nd:YAG, excimer or ruby source. Each of those lasers has different wavelengths (Mokgalaka and Gardea-Torresdey, 2006). The size of the ablated spot can vary from 1 µm – 100 µm. The sample is mounted on a, in X,Y and Z direction adjustable, platform within an airtight sample cell under atmospheric pressure The sample chamber is flushed with an inert carrier gas to transport the ablated particles via an transportation line to the ICP-MS. Usually argon or helium is used as a carrier gas, whereat helium is reported to be more effective (Durrant, 1999; Mokgalaka and Gardea-Torresdey, 2006; Sindern, 2017).

In this work in-situ spot analysis of pyrites have been conducted. The analyzed element masses are ^{51}V, ^{52}Cr, ^{55}Mn, ^{59}Co, ^{60}Ni, ^{66}Zn, ^{71}Ga, ^{74}Ge, ^{75}As, ^{82}Se, ^{95}Mo, ^{107}Ag, ^{111}Cd, ^{115}In, ^{118}Sn, ^{121}Sb ^{125}Te, ^{197}Au, ^{201}Hg, ^{205}Tl, ^{208}Pb and ^{209}Bi. An ESI NWR210 Nd:YAG laser ablation system coupled with an Agilent 8800 triple quadrupole ICP-MS (Chair of General and Analytical Chemistry, Montanuniversität Leoben) has been used. An ablation spot size of 50 µm in diameter with a laser of 2-3 J/cm^2 and a repetition rate of about 10 Hz were set. The used carrier gas was Helium with a flowrate of 0.75 L/min. The measurement included a 30 second background collection, followed by 60 seconds of sample laser ablation and data acquisition. Between each ablation cycle a 30-second delay was carried out for cell washout. The data acquisition was conducted over multiple sessions due to technical issues with the instrument.

The standards used for these measurement were MUL-ZnS1 (Onuk et al., 2017) and MASS-1 (Wilson et al., 2002). The standards were re-analyzed every 20th shot for correction of instrumental drift. The reduction of the data was conducted using the software Iolite 4 (Paton et al., 2011).

2.2.4 ELECTRON PROBE MICROANALYSIS (EPMA)

The Electron Probe Microanalysis (EPMA) is just as the SEM an electron microbeam instrument. It uses a combination of high-spectral resolution X-ray wavelength dispersive spectroscopy (WDS), providing greater analytical precision, and energy dispersive spectroscopy (EDS). Just like the SEM the sample surface is bombarded with an electron beam, generating various signals which then are detected and processed (Pownceby et al., 2007; Yang, 2022). An EMPA instrument is mainly used for quantitative analysis and trace elemental mapping (Yang, 2022). Proper sample preparation is essential in EMPA. The samples need to have a flat and well-polished surface to ensure the accuracy of the analytical results. Also, like with the SEM, the samples were with a thin (20nm) conductive film of graphite to prevent charging of the samples surface and sample heating (Yang, 2022).

The EPMA element map analysis was conducted on a JEOL Superprobe JXA 8200 at the MUL Chair of Resource Mineralogy. The EPMA is equipped with a cathodoluminescence detector, 5 WDS spectrometers, and an EDS spectrometer. Map analyses were done on pyrites with strong visible zonation during multiple sessions. Analytical conditions are given in Table 2.

Table 2: EPMA spectrometer adjustments and analytical conditions for element mapping on pyrite.

WDS			**EDS**
spectrometer	Xtal	Element (line/position)	Element (Line)
1	TAP	As (L-α/105,187)	Fe (K-α)
2	TAP	Ag (L-α/132,983)	S (K-α)
3	LIF	Ni (K-α/115,163)	Pb (L-α)
4	LIFH	Co (K-α/124,293)	Cu (K-α)
5	LIFH	Au (L-α/89,067)	Sb (L-β)
			As (K-α)

	Acc. V (kV)	**Probe C (nA)**	**dwell time (ms)**
A1370 (Hoher Goldberg)	25.0	143.0	500.0
A1463 (Goldzeche)	25.0	223.3	500.0
PM-RG-03 (Rotgülden)	25.0	221.9	600.0

3. RESULTS

3.1 FIELD RESULTS

The Radhausberg mining district is characterized by a large number of mine dumps which are distributed over a large area of varying altitude (Figure 11). Most of the mine dumps are above 2000 m and the density of vegetation is reduced in this area. The rocks found in the heaps are brown to blackish in color due to the weathering of the ores. Minerals such as pyrite, chalcopyrite and galena can already be determined macroscopically in some specimens. Two accessible adits were found during our fielwork. The first, located in the south at around 1940 meters above sea level, is probably the Hieronymus adit, which is covered by some rocks, but is basically accessible. The Gottesgab adit to the east is accessible for an estimated 200 meters without major risk. However, past 200 m there is a junction where the roof of the adit is falling in and multiple rock slabs are close to falling. Samples were taken from several mine dumps at different altitudes (see appendix) as well as from a small vein in the Gottesgab adit.

Figure 11: At the Radhausberg with view to SSE and the dumps of the former mining activity (circled in orange).

The three mining districts Laserzen, Breitschitzen and Dösener Alm marked in the IRIS map of Geosphere Austria (Weber et al., 2019) were examined more closely to find indications of mineralization and former mining. No significant mineralization was found in any of the three districts. In the Laserzen/Breitschitzen area, prospecting holes were found in quartz veins that are a maximum of one meter deep. The material extracted here was quartz, which is pure and has no mineralization. Some samples were taken but none of them represents a mineralization.

The area of the Pasterze mining district is, comparative to Laserzen, relatively large. Mineralization was found both within the quartz veins, which are up to 1 meter wide, as well as within several of the float rocks. Two mineralized veins (Figure 12) are visible to the east of the Margaritzen reservoir and can already be seen from the opposite side of the lake. These veins contain up to 2 cm big pyrite aggregates and occasionally chalcopyrite (Figure 12). Two significant lode rocks could be found in this mining area. The first is a large green slate boulder with thin layers of pyrite and chalcopyrite mineralization. The second is a football-sized quartz stone with a layer of pyrite up to two centimeters thick. Several samples were taken from the mineralized quartz vein as well as from the lode rocks.

Figure 12: Left: Pasterze to the west of the Margaritzen reservoir with a view to the west. Two large (up to > 1 m) quartz veins with sulfide mineralization. Right: Close-up of the left quartz vein with visible pyrite mineralization and reddish-brown weathering material covering the quartz.

The Mesenatten mining district, which lies between Pasterze and Hochtor (Figure 6), and differs from the neighboring districts in terms of the host rock. In the area of the former mining operations, fuchsite-rich rocks can be found, which contain small amounts of sulfide ore. An accessible adit was also found (Figure 13). However, this was not entered due to the narrow access and danger of rockfall. However, there are indications that it is/was recently explored. Some samples were taken from the mineralized, fuchsite-rich rock.

The Hochtor mining district, on the other hand, morphologically resembles a karst landscape. The rocks most frequently encountered are carbonate rich and pervaded by holes (Figure 13). Quartz rich rocks can also be found in the more western part of the district (Figure 6). These often show a brownish discoloration, which indicates the weathering of sulfide minerals. Two adit entrances were found. The first is accessible for almost 50 meters until it ends. The second adit is located directly on the pass road and its entrance is partially broken, which is why it could not be walked through. No relevant gold ore-bearing samples, but plenty of lead bearing samples were found in this district.

Figure 13: Left: Mesenatten with view to the north. Entrance to an accessible adit. Right: Hochtor/Fuscher Wegscheide with view to the east. Outcrop of carbonate rock pervaded by holes and with high pososity.

The Imhof adit is a 2500-meter-long undercut adit that uncovers several ore veins. Existing mineralization is difficult to find as it has largely been mined out. The walls, as well as the roof and floor, have a reddish-brown coloration due to the weathering of the ore minerals. Severe sintering can also be observed in some areas. Some drifts are partially collapsed or no longer safe to enter, as the wooden substructures are very decayed. Samples were taken from drifts that represented 3 of the major vein sets, the Dionysvein, the Schareck North vein and the Kupelwieser vein.

The Siglitz area is located at the end of the Siglitz valley west of Sportgastein (Figure 7). Several adit entrances were found. One of them was on the other side of the valley (SSW) which is apparently only accessible via steep terrain. Therefore, this adit was not entered. Two additional adit entrances on the north side of the valley are located at an altitude of around 1900 meters and lie one above the other (Figure 14). The upper adit entrance is accessible for several hundred meters and has sections that were mined upwards and downwards. However, most of the shafts running downwards are flooded. After about 50 meters you pass a dry shaft that connects to the adit below. In this adit, the mineralization is still clearly visible in some areas. The samples that were taken come from the mineralized vein (Figure 14).

Figure 14: Located at the end of the Siglitz valley Left: View to the N. The entrance to an adit can be seen (red square), which can only be reached via difficult terrain. Right: Mineralized vein where the sample has been taken within the adit.

Comparing the location of the accessible adit in Siglitz with the mineralization veins marked in the figure from Paar et al., 2006, it can be assumed that the sample taken from the Siglitz district comes from the Dionys or Saiger vein (Figure 15).

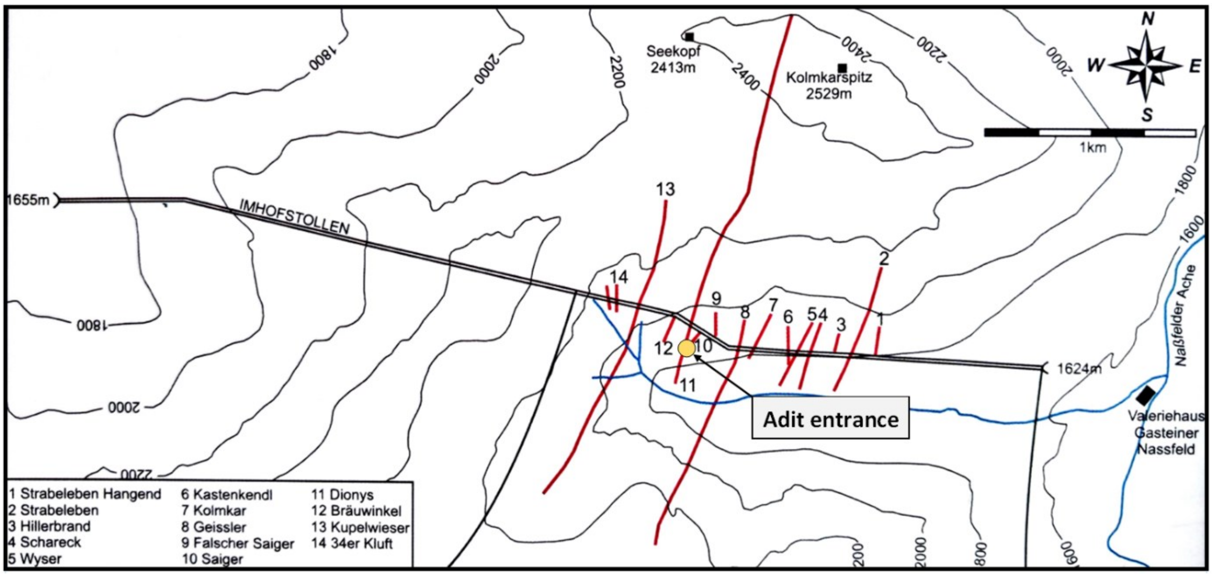

Figure 15: Georeferenced map (Paar et al., 2006) of the Imhof adit showing the different mineralized veins (red lines). The yellow point is marking the location of the Siglitz adit entrance.

At the end of the Nassfeld valley south of Sportgastein (Figure 7) is the Wasinger E / Gugl mining district. An adit entrance was found within this district, but it was flooded due to the weather conditions and therefore not accessible. In addition, the weathering cover at the surrounding area of the adit entrance was too thick to take a representative sample. Samples were therefore taken from the nearby stream bed, which showed sulfide mineralization.

3.2 REFLECTED LIGHT MICROSCOPY AND SCANNING ELECTRON MICROSCOPY (SEM)

In general, pyrite was present in 22 of 24 sections, of which the proportion was significant in 20 samples. Chalcopyrite and galena were present in 19 of 24 specimens, of which the proportion was significant in only 5 specimens. Galena and chalcopyrite are often found as fine inclusions within the pyrites. The Siglitz, Hochwurten, Bockhart and Radhausberg mining districts are the only ones with significant amounts of arsenopyrite. Visible gold can be found in 8 of 24 specimens in sizes from < 15 µm to 500 µm. These gold particles are mostly in contact with galena. These are always electrum with an approximate Ag:Au ratio of 1:2, with the exception of sample PM-RG-01 (Rotgülden) from the Kupferkieskaverne of the Rotgülden mining district where the Ag:Au ratio is almost 1:1. This is also the only specimen where silver and higher amounts of silver-bearing minerals are present and thus differs significantly from the others. The samples of the Erzwies mining district differs greatly from the others due to the high sphalerite content, which outweighs the pyrite content. Fe-Mn oxides were also found here as alteration products. Even though the mineral content of the Fusch/Knappenstube district is very similar to the other districts, it still differs due to the texture/shape of the minerals. Sulfosalts, including Sb, Ag, Cu, Pb, Bi, were also observed in four of the 24 samples. However, these are only in contact with arsenopyrite or galena. Section A1979 of the Schellgaden mining district is the only one in which barite can be found as fine inclusions within pyrite. Other minerals that were accessory in some samples are zircon, thorite, monazite, boulangerite, apatite and xenotime. In Table 3 below all relevant minerals contained in the polished sections are listed with the color representing the relative amounts of the minerals in each sample.

Table 3: Most abundant minerals in the different epoxide mounts; (xxx, dark green) high abundance of the mineral; (xx, middle green) moderate abundance; (x, bright green) low abundance.

Mining disdrict	**Bezeichnung**	**Pyrite**	**Chalcopyrite**	**Galena**	**Sphalerite**	**Arsenopyrite**	**Ironhydr-oxides**	**Pyrrhotite**	**Visible gold**	**Angelesite/ Cerussite**	**Sulfosalts**	**Illmenit**	**Covelline**	**Silver**
Hirbach-Schiedalpe	A1510	x	xx	x			x							
	A1514	xxx		xx					x			x		
Pasterze	PM-PA-02	xxx	x		x			x						
	PM-PA-05B		xx		x		x							
Knappenstube/Fusch	II/873b	xxx	xx	xx	xx			x						
Mesenatten	PM-MS-02	x	x					x				x		
Goldzeche	A1462	xxx	xxx	xxx	x		xx			xx			x	
	A1463	xxx	xxx	xxx	x		xx			xx	x		x	
Hoher Goldberg-Alteck	A1373	xx	xxx	x	x	x	x		x					
	A1370	xxx	xx	x		x								
Hochwurten	A1758	xx	x	x			x							
	PM-HW-01	xxx	x			xx	x	xxx			x			
Imhof	PM-IM-03	xx		x	x									
Siglitz	PM-SZ-01	xxx		x		xxx			x	x				
Bockard	21TG27	xx		x	x	xxx			x			x		
	21TG57	xx	x	x		xx								
Erzwies	A1740	xx	x	xx	xxx					x				
	A1742	xx	x	xxx	xxx						x			
Radhausberg	PM-RB-04a	xxx	x	x		xx	x							
	PM-RB-07	xxx		x		xxx			x		x			
Rotguelden	PM-RG-01		xxx	x	x		x	xxx	x					x
	PM-RG-03	xxx	x				x	x						
Schellgaden	A1870	xxx	x	xxx					x	x			x	
	A1979	xx	x	xxx					x					

3.2.1 HIRZBACH-SCHIEDALPE

A1510

The main mineral in this polished section is chalcopyrite. This has very uneven, bay-shaped crystal boundaries towards the gangue minerals. With a pale-yellow color and a lower hardness, it is easy to distinguish it from the pyrites. The pyrites are xenomorphic and can be recognized as small inclusions within and at the edges of chalcopyrite (Figure 16A). The crystal boundaries are mostly rounded, and they reach a maximum size of only 80µm. Occasionally, pyrites can also be observed outside the chalcopyrite. A zoning within the pyrites is not recognizable with the optical microscope. The pyrites are often surrounded by a dark gray phase with low reflectivity. This phase was identified by SEM as an ironhydroxide with copper content (Figure 16B). Some pyrites have also been completely altered to iron hydroxide. Occasionally, galena and Pb-Sn sulfides can be observed between the pyrites and the chalcopyrite. These show only irregular crystal boundaries and fill the space between the other minerals. They reach a maximum size of 50µm. The gangue minerals consist mainly of quartz and sporadic dolomite crystals.

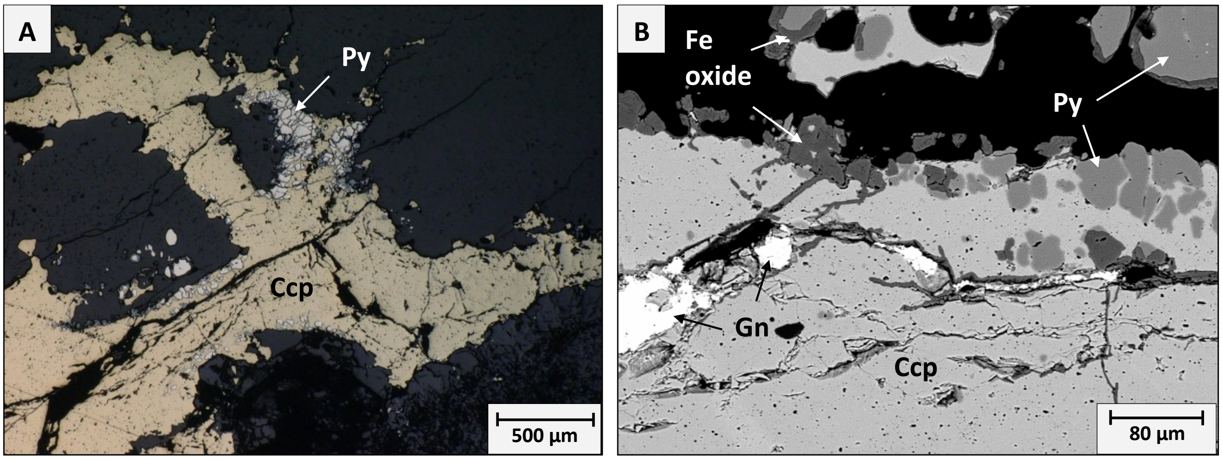

Figure 16: Sample A1510 (Hirzbach-Schiedalpe); A) fractured chalcopyrite (Ccp) with small, rounded pyrite (Py) inclusions clustered at the edge of the chalcopyrite; B) BSE image showing the chalcopyrite with galena (Gn) filing the fractures and iron-oxides surrounding or completely replacing the pyrite.

A1514

Macroscopically, pyrite and galena are already recognizable, which, in addition to the gangue minerals, make up most of the section. The pyrites are mostly xenomorphic, occasionally also idiomorphic and reach sizes of up to 1 mm. The crystal boundaries are straight and rounded, and the pyrites are also highly fractured, riddled with cracks and have many holes/inclusions. The galena is easily recognizable due to the triangular polishing pits. It is xenomorphic and has very irregular jagged crystal boundaries

(Figure 17B). Furthermore, the galena can be found within the cracks and as inclusions within the pyrite. It is also in contact with electrum particles (Figure 17B). The electrum in this polished section is in contact with the galena (Figure 17B) or as small crystals (< 20 µm) within cracks of pyrite surrounded by galena. The electrum particles have a size of up to 100 µm. Morphologically, like galena, it has very irregular crystal boundaries. Measurements with the SEM have shown that this is electrum, with approx. 60 atom% gold and 40 atom% silver. Both, patchy and striped zonations can be seen in the pyrite (Figure 17A). The gangue minerals consist mainly of quartz, but also contain dolomite and muscovite in smaller amounts.

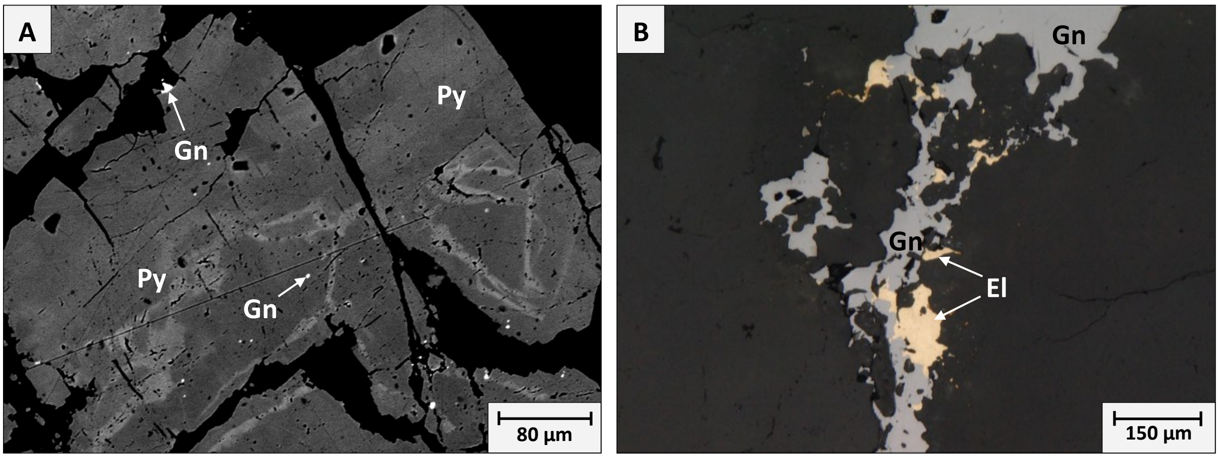

Figure 17: Sample A1514 (Hirzbach-Schiedalpe); A) BSE image of pyrites (Py) showing an irregular zonation and small galena (Gn) inclusions; B) microscopy image showing the galena (Gn) in contact with the electrum (EL), both having irregular crystal boundaries.

3.2.2 PASTERZE

PM-PA-02

This sample is characterized by a one- to two-centimeter-thick layer of pyrite on quartz, which can already be seen macroscopically. Using reflected light microscopy and SEM, the minerals pyrite, chalcopyrite, pyrrhotite and sphalerite were identified. The pyrite can be clearly identified as such due to its color (white with a yellow tinge) and high reflectance. Notable is the highly decomposed structure of the pyrites. These are crisscrossed by several cracks and have many small holes. Most of the crystals are xenomorphic and the original crystal form is only recognizable in a few of them. The crystal boundaries are mostly rounded or bay-shaped, only a few specimens show straight boundaries. The pyrite crystals reach sizes larger than 2 mm. The chalcopyrite can be recognized as very small, xenomorphic crystals within the pyrites (Figure 18A). The chalcopyrite has straight to rounded crystal boundaries and is only present as an accessory phase. Only one pyrrhotite crystal could be found, which is very small and has rounded crystal boundaries. This is found within the pyrite and is partially adjacent to the chalcopyrite (Figure 18A). Both chalcopyrite and pyrrhotite are smaller than 100µm. The sphalerite is only found as inclusions smaller than 10 µm within the pyrite, and generally are found along zonation boundaries (Figure 18B). The zonation of the pyrites is clearly recognizable in the SEM and has a rather irregular appearance (Figure 18B). The SEM analysis revealed a slightly higher arsenic content within the brighter zones.

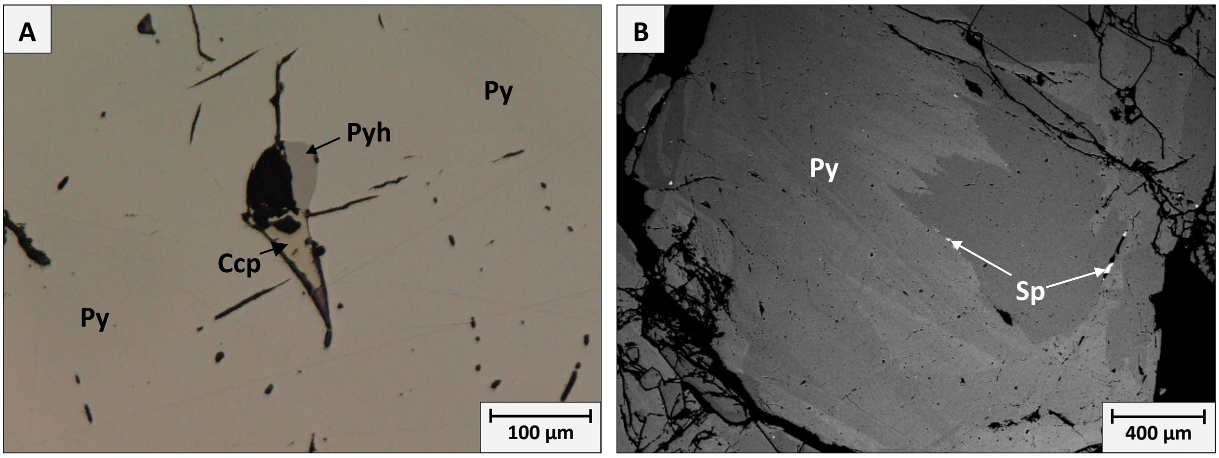

Figure 18: Sample PM-PA-02 (Pasterze); A) pyrite (Py) with inclusions of pyrrhotite (Po) and chalcopyrite (Ccp); B) BSE image showing a Pyrite (Py) crystal with a strong zonation and Sphalerite (Sp) inclusions (< 10 µm) generally are found along zonation boundaries.

PM-PA-05b

Only a small number of ore minerals can be recognized within this cut. The main mineral is chalcopyrite, followed by Iron-Copper-hydroxides. The chalcopyrite is clearly recognizable as such due to its medium to high reflectivity and the golden yellow color. It is criss-crossed by cracks and has an increased number of small holes/inclusions (Figure 19A). The chalcopyrite is xenomorphic and has a granular habit. In addition, there is a gray phase at the edge and within the cracks which can be identified as a Cu-rich iron hydroxide (Figure 19A). This can be recognized by the orange to brown-red internal reflections which are characteristic for this mineral. Occasionally, another grey phase can be observed at the edge, which has a strong anisotropy with a grey-blue color. This is often intergrown with the iron hydroxide, and was identified as cuprite using the SEM. Sporadic, the chalcopyrite has already been completely transformed into cuprite and limonite. Furthermore, a titanium oxide could also be observed, which is in contact with the cuprite. Inclusions of sphalerites and Pb-Bi-Ag-tellurites can be found within the chalcopyrite (Figure 19B). The sphalerites have a granular habit and reach a size of up to 50µm while the tellurites are only at a maximum of 5µm in size. The tellurites can also be found as inclusions within the sphalerite (Figure 19B).

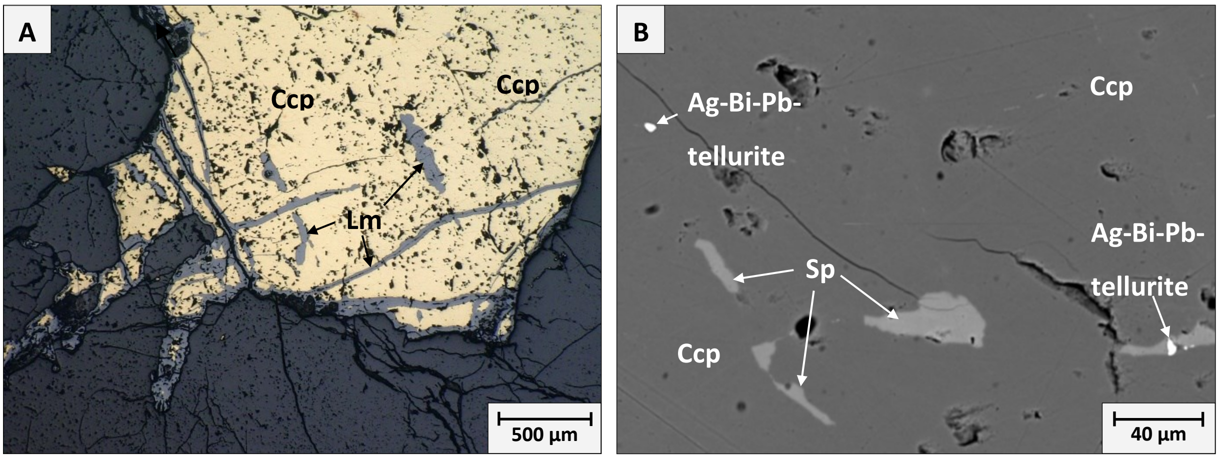

Figure 19: Sample PM-PA-05b (Pasterze); A) chalcopyrite (Ccp) altered on the edges and cracks to a Cu-rich Limonite (Lm); B) BSE image representing a close-up of the chalcopyrite (Ccp) with inclusions of sphalerite (Sp) having sizes of less than 50 µm and Ag-Bi-PB-tellurite (< 5 µm) as inclusions within chalcopyrite as well as sphalerite.

3.2.3 FUSCHER WEGSCHEIDE/MESENATTEN

II/873b

This polished section is characterized by a high proportion of large, rounded pyrite crystals, which are already visible macroscopically. Pyrite makes up the majority of this section. These are xenomorphic and range in size from less than 50 µm to 2 mm. Furthermore, the pyrites are crisscrossed by cracks, often have inclusions of other minerals and have very irregular, bay-shaped crystal boundaries galena (Figure 20A). The minerals surrounding the pyrite are a mixture of chalcopyrite, pyrrhotite, sphalerite and galena (Figure 20A). All have rounded to bay-shaped crystal boundaries and are found at the rim of the pyrite. These can also be found as inclusions within the pyrites. The inclusions usually have straight to rounded crystal boundaries in contact with the pyrite, while the surrounding minerals have very irregular crystal boundaries and penetrate strongly into the pyrite galena (Figure 20A). These minerals can also be found in the cracks of the pyrites, especially chalcopyrite. The inclusion of chalcopyrite in sphalerite (i.e. chalcopyrite disease) can be identified galena (Figure 20A). The rather patchy or striped zoning of the pyrites is clearly recognizable in some crystals (Figure 20B).

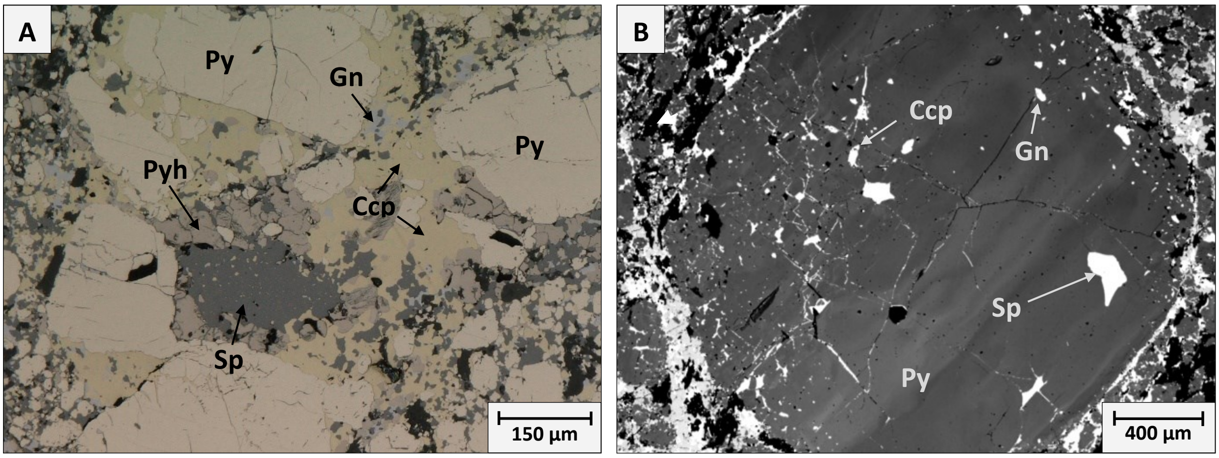

Figure 20: Sample II/873 (Fuscher Wegscheide); A) Pyrite (Py) crystals of different sizes (< 50 µm up to 2 mm) with inclusions of pyrrhotite (Po), galena (Gn), sphalerite (Sp) and chalcopyrite (Ccp), surrounded by a mixture of chalcopyrite (Ccp), pyrrhotite (Po), sphalerite (Sp) and galena (Gn); B) BSE image showing a Pyrite (Py) crystal with a striped zonation, multiple inclusions as well as filled cracks.

PM-MS-01

Macroscopically, it is characterized by its high quartz and mica content. There are only a few pyrites present, which are also macroscopically recognizable. In addition to the gangue minerals, the polished section consists mainly of pyrites, which are both idiomorphic and xenomorphic. The xenomorphic pyrites are usually larger (up to 1 mm) and are either very eroded or are already altered to limonite at the edges and within cracks (Figure 21A). The idiomorphic pyrites are intact and have hardly any inclusions or cracks. Within the idiomorphic pyrites, zoning is only faintly visible in SEM. The inclusions within pyrite are chalcopyrite and pyrrhotite. Both minerals show a granular habit and rounded crystal boundaries. These are also smaller than 50 µm. The minerals ilmenite (approx. 200 µm in size), zircon, thorite and monazite were also observed (Figure 21B). The last three reach a maximum size of 15 – 30 µm. The zircon also exhibits zoning. The surrounding gangue minerals consists of quartz, feldspar, muscovite, and calcite.

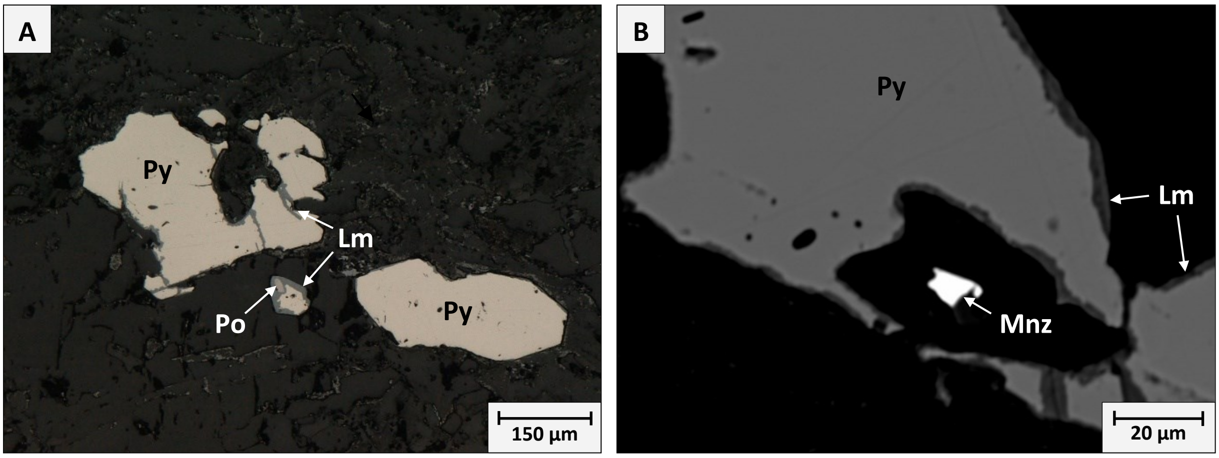

Figure 21: Sample PM-MS-01 (Mesenatten); A) Hypidiomorphic pyrite (Py) crystals and a small pyrrhotite (Po) crystal (< 50 µm) rimmed by the alteration product Limonite (Lm); B) BSE image showing a pyrite (Py) crystal altered to Limonite (Lm) on the edges and within cracks and a small (~10 µm) Monazite (Mnz) crystal.

3.2.4 GOLDZECHE

A1462

The mineral phases pyrite, galena and chalcopyrite are macroscopically recognizable within the polished section. Other identified minerals are sphalerite, iron hydroxide, covelline, cerussite and anglesite. The pyrites are easy to identify microscopically due to their high reflectivity and pale-yellow color. A distinction can be made between: (1) xenomorphic, up to 3 mm large pyrites, which are perforated by cracks. They are rimmed by iron hydroxides as a weathering product (Figure 22A). (2) Idiomorphic crystals, which reach sizes of up to 800 µm and are completely intact. These have straight crystal boundaries and are often surrounded by chalcopyrite or iron hydroxides. Both types of pyrite contain inclusions of chalcopyrite, sphalerite or galena. Both, chalcopyrite and galenite have very irregular, bay-shaped crystal boundaries and are surrounded by a mixture of weathering products such as iron hydroxides, cerussite, anglesite and covelline (Figure 22A). Galena can contain inclusions of chalcopyrite and sphalerite, while the chalcopyrite only has inclusions of galena. The sphalerites are small with a maximum size of 250 µm. Visible is the chalcopyrite disease which is typical for sphalerite. The crystal boundaries tend to be rounded to bumpy. Zonations are easily visible within the pyrites. Especially within the idiomorphic pyrites growth zonations can be seen (Figure 22B).

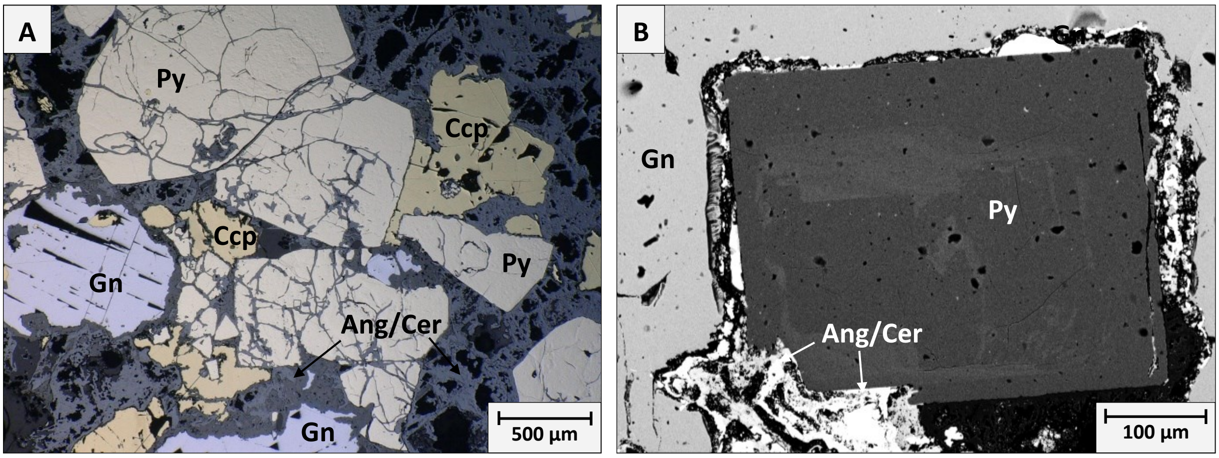

Figure 22: Sample A1462 (Goldzeche); A) Hypidiomorphic pyrite (Py) crystals perforated by cracks; galena (Gn) and chalcopyrite (Ccp) which are surrounded by a mixture of fine grained cerussite (Cer) and anglesite (Ang). B) BSE image showing an idiomorphic pyrite (Py) with distinct zonation surrounded by anglesite (Ang)/ cerussite (Cer) and galena (Gn).

A1463

This polished section is almost identical to sample A1462. The identified minerals are pyrite, chalcopyrite, galena, sphalerite, cerussite, anglesite, limonite and covelline. The mineral sizes in this section are slightly different from those in A1462. Furthermore, a light brown-gray mineral was observed within chalcopyrite which contains several inclusions of galena and boulangerite. This mineral could be identified with the SEM as Sb-Ag-Cu-sulfosalt (polybasite or pyrargyrite; Figure 23A). The pyrites in this section also exhibit zonations parallel to the crystal boundaries (Figure 23B). The zonations are particularly intense in the idiomorphic pyrite (Figure 23B).

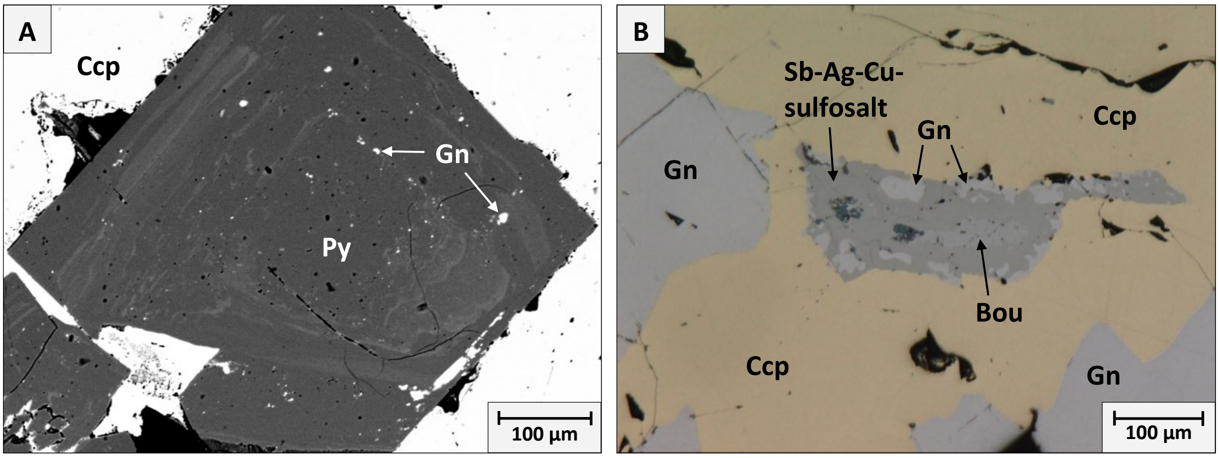

Figure 23: A1463 (Goldzeche); A) BSE image showing idiomorphic pyrite (Py) with distinct concentric zonation parallel to the crystal boundary including fine (< 20 µm) galena (Gn) inclusions, surrounded by chalcopyrite (Ccp); B) Mineral cluster consisting of Boulangerite (Boul), galena (Gn) and Sb-Ag-Cu-sulfosalt surrounded by chalcopyrite (Ccp) and galena (Gn).

3.2.5 HOHER GOLDBERG

A1373

The main minerals of this polished section are chalcopyrite and pyrite, which have very different morphologies. The pyrites are mostly hypidiomorphic to idiomorphic and often intergrown. The larger pyrites are riddled with cracks and have inclusions of galena. Some crystals are also intergrown with idiomorphic arsenopyrites (Figure 24A). Inclusions of gangue minerals, such as idiomorphic quartz crystals, can also be seen. The crystal boundaries are mostly straight. In addition, idiomorphic, platy muscovite crystals protrude into some pyrites. Faint zoning within the pyrites can be recognized with the help of the SEM, which have a rather patchy appearance. The chalcopyrite is xenomorphic and has very uneven, jagged crystal boundaries. It contains neither inclusions of sphalerite nor galena. In addition, the edges of the chalcopyrite are altered to iron hydroxides. Very small chalcopyrite aggregates can be recognized within these iron hydroxides. These alterations can also be seen sporadically on the edges of pyrite, but with straight crystal boundaries and with fine chalcopyrite included. The sphalerite usually occurs in contact with the chalcopyrite or limonite. Occasionally, however, they are also in contact with galena or stand alone. It also contains fine inclusions of chalcopyrite aggregates, the so-called chalcopyrite disease. The crystal boundaries are irregular (jagged) and the mineral only occurs as a minor component. The galena can be easily recognized by its triangular pits. This is xenomorphic and has irregular crystal boundaries. It is in contact with all other minerals. The electrum is contained in the sample as visible free electrum and has an average composition of 77.55 atom% Au and 22.45 atom% Ag. It has irregular crystal boundaries and is in contact with galena. The largest crystal reaches a size of approx. 200 µm. The minerals are surrounded by quartz, fine muscovite crystals and calcite (Figure 24B)

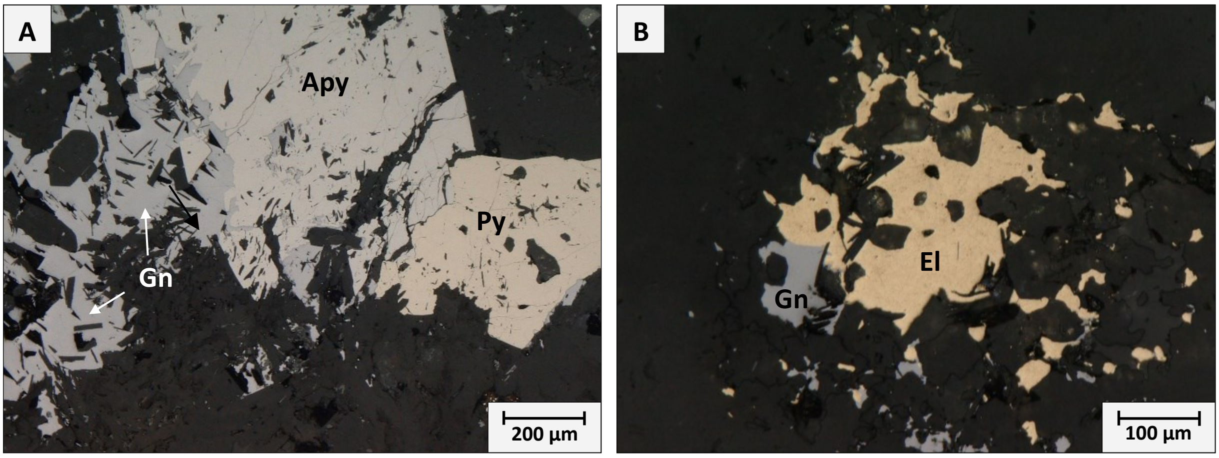

Figure 24: Sample A1373 (Hoher Goldberg); A) Hypidiomorphic pyrite (Py) and arsenopyrite (asp) intergrown with each other and with galena (Gn); B) Jagged electrum (El) in contact with galena (Gn).

A1370

The minerals pyrite and chalcopyrite can be identified macroscopically. Those minerals are confirmed by optical properties typical of chalcopyrite and pyrite. The minerals arsenopyrite, galena, quartz, calcite and dolomite have also been identified. The pyrite in this section can be divided into two types, as within the “Goldzeche”: (1) Idiomorphic pyrites intergrown, which have straight crystal boundaries and sizes of maximum 300 µm (Figure 25A). An alteration seam as in “Goldzeche” is not recognizable. (2) Hypidiomorphic to xenomorphic pyrites, intergrown, which reach sizes of up to 2 mm and are heavily fractured and interspersed with cracks. There are also inclusions of chalcopyrite, arsenopyrite, galena and gangue minerals within the pyrites. The chalcopyrite are xenomorphic and surround all other minerals as a kind of "gap filler". The crystal boundaries are mostly straight and rounded in contact with other minerals. Galena is only found as inclusions within pyrite and chalcopyrite. The galena inclusions within the pyrites are very small with less than 5 µm and can be observed distributed throughout the pyrite (Figure 25B). The inclusions reach a maximum size of 50 µm and have straight to rounded crystal boundaries. The arsenopyrite is hypidiomorphic to idiomorphic and can be recognized both as isolated crystals and as inclusions within pyrite or chalcopyrite. Intensive zonation can be recognized within pyrite (Figure 25B). The zonation of the idiomorphic crystals is stronger than that of the xenomorphic crystals. A dark core with a lighter edge can be recognized using the SEM (Figure 25B). As measured in the SEM, this is caused by a higher arsenic content in the edge. The surrounding vein material is composed of quartz, calcite and iron dolomite. Some quartz is idiomorphic and forms beautiful crystals.

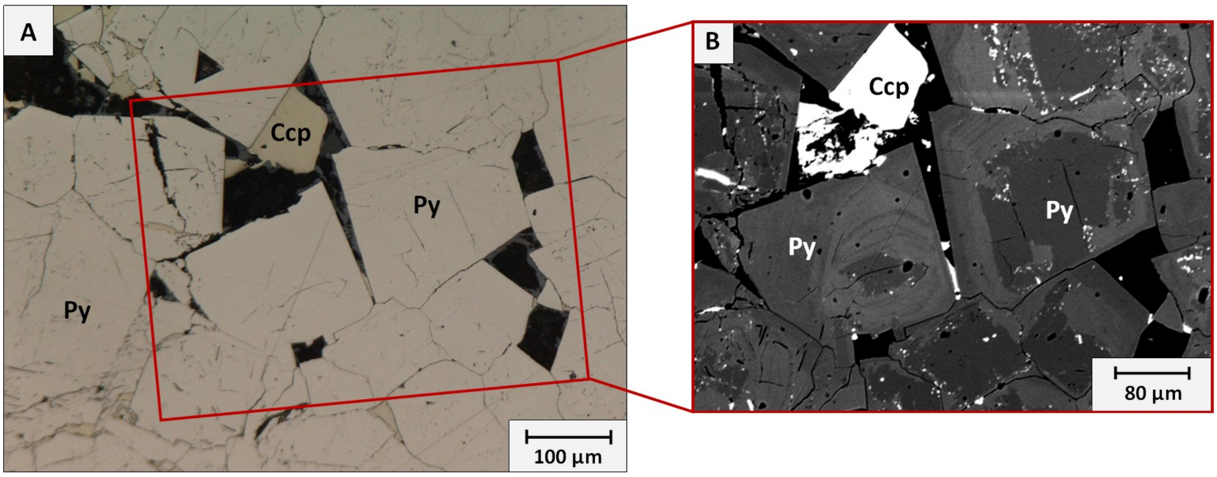

Figure 25: Sample A1370 (Hoher Goldberg); A) Idiomorphic and hypidiomorphic, pyrite (Py) crystals, partly intergrow to each other and chalcopyrite (Ccp) in between the cracks of the pyrite (Py); B) BSE image showing a close-up image of the idiomorphic pyrites (Py) showing distinct concentric zonation with different shades of grey and many fine (< 10 µm) inclusions of chalcopyrite (Ccp).

3.2.6 HOCHWURTEN

A1758

Pyrite and chalcopyrite can already be recognized macroscopically. The pyrites make up the majority of the ore minerals. Apatite, iron hydroxides and galena can be recognized as accessory minerals. The pyrites are easy to distinguish from the other minerals due to their isotropy and high reflectivity. The pyrites are mostly hypidiomorphic and only occasionally xenomorphic or idiomorphic (Figure 26A). The crystal boundaries are straight and rounded. Noticeable are the number of cracks that run through the pyrites as well as inclusions of gangue minerals, chalcopyrite, galenite, apatite and pyrrhotite. The pyrites reach sizes of up to 600 µm. The chalcopyrites are xenomorphic and have a decomposed appearance. In only a few cases can they be recognized as inclusions within pyrite (Figure 26A). In this case, the chalcopyrites have straight crystal boundaries towards the pyrite. Furthermore, minerals with a light grey as well as dark grey color are also recognizable. These can be found both as inclusions in the pyrite and as free-standing. These minerals have been identified using the SEM as galena and iron hydroxides (Figure 26B). The crystal boundaries are very irregular. The gangue minerals consist of feldspars as well as quartz.

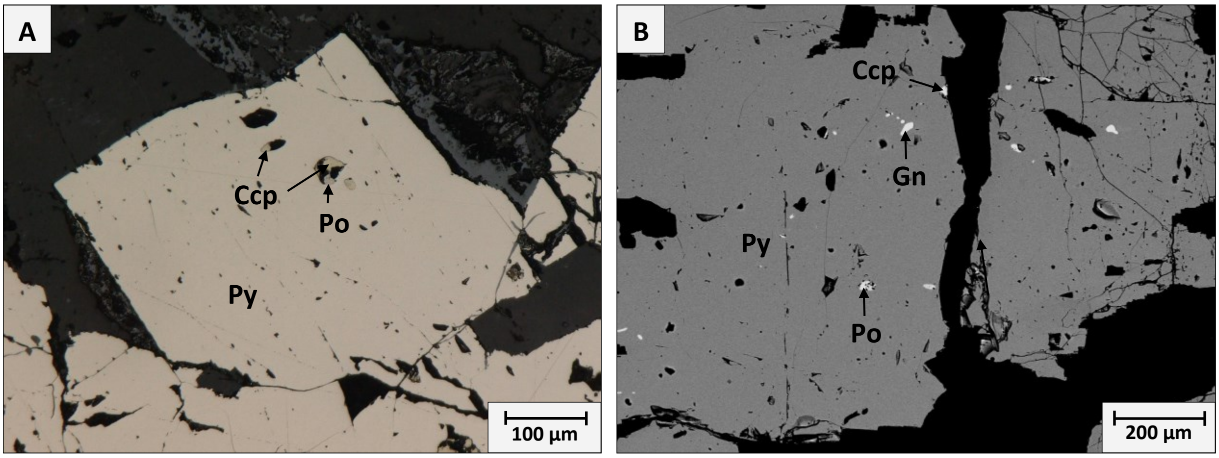

Figure 26: Sample A1757 (Hochwurten); A) Hypidiomorphic pyrite (Py) crystals partly intergrow with each other and small (< 40 µm) inclusions of chalcopyrite (Ccp) and pyrrhotite (Po); B) BSE image showing xenomorphic pyrite (Py) with inclusions of chalcopyrite (Ccp), pyrrhotite (Po) and galena (Gn).

PM-HW-01

Many phases can be already recognized macroscopically. Microscopically, the minerals pyrite, pyrrhotite, iron hydroxides, chalcopyrite, arsenopyrite, sulfosalts, dolomite/ankerite and marcasite could be identified. Pyrites can be divided into idiomorphs and xenomorphs. The idiomorphic pyrites usually have straight to less rounded crystal boundaries. They have hardly any cracks, show no signs of alteration and only reach a maximum size of 1 mm. The zonation in these pyrites is straighter than the zonations of the xenomorphic pyrites, which are very patchy (Figure 27B). The xenomorphic pyrites are very large with sizes of up to 5 mm and have rounded to bay-shaped crystal boundaries. Furthermore, they are heavily interspersed with cracks and show alteration to limonite on the edges at certain spots. These iron hydroxides show partial zoning and form bushy, needle-like aggregates, which protrude into the pyrites and pyrrhotites (Figure 27A). The pyrrhotites are very large with > 5 mm and contain many bird's eye decay structures (Figure 27A). Furthermore, the pyrrhotites are crisscrossed by many cracks and have bay -shaped to rounded crystal boundaries (Figure 27A). There is also an area where pyrrhotite is no longer present, but only a fine-grained mixture of pyrite and marcasite. The arsenopyrites are hypidiomorphic to xenomorphic and have straight to rounded crystal boundaries. They have inclusions of sulfosalts and chalcopyrite. These are Bi-Pb-Ag sulfosalts, which are only found as inclusions in the arsenopyrites. The chalcopyrites reach sizes of up to 300 µm and have rounded to bay-shaped crystal boundaries. These are distributed throughout the sample and are also present as inclusions in pyrite, pyrrhotite and arsenopyrite. The surrounding minerals are of the dolomite-ankerite mixing series which also show zonation with a varying magnesium content.

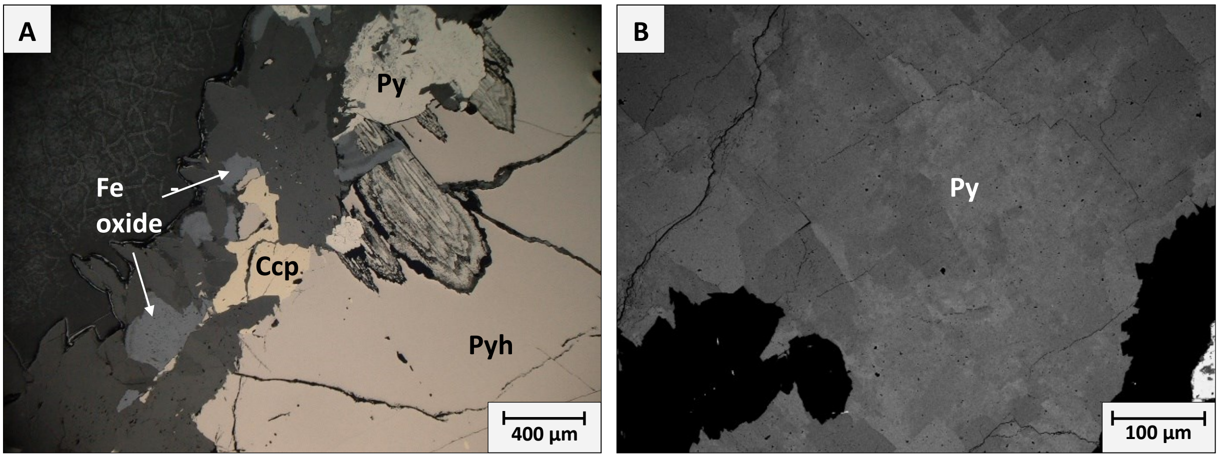

Figure 27: Sample PM-HW-01 (Hochwurten); A) Xenomorphic pyrrhotite (Po) with bird's eye decay structures in contact with a pyrite (Py) crystal. Spiky iron-oxides along the edge of the pyrrhotite (Po), pyrite (Py) and chalcopyrite (Ccp); B) BSE image showing xenomorphic pyrite (Py) with a very patchy zonation.

3.2.7 SIGLITZ

PM-IM-03

This polished section mainly includes pyrites. These occur as medium-sized to large with sizes up to 2 mm, intergrown, mostly xenomorphic to, more rarely, hypidiomorphic crystals. They often show alteration zones and are penetrated by many cracks. Some smaller exposed pyrites are also idiomorphic and have fewer cracks. Within some pyrites a light grey phase can be seen which is xenomorphic and has only a low reflectivity. This is sphalerite which can be observed both as inclusions within the pyrites but also as isolated minerals. Other inclusions that can be observed within the pyrites are galena, zircon, xenotime and monazite (Figure 28B). Galena and sphalerite can also be found within the cracks of pyrites. The xenotime has a size of approx. 50 µm, is hypidiomorphic, has straight to rounded crystal boundaries and exhibits zoning (Figure 28A). A monazite crystal with a maximum of 5 µm can also be seen next to the xenotime, which also has zoning (Figure 28A). Within the xenotime, inclusions of Th-P silicates are visible, which are only 4 µm in size, have a granular habit and rounded crystal boundaries (Figure 28A). A clear zonation can be recognized within the pyrites. This zonation has a rather patchy pattern (Figure 28B). Different arsenic contents can be measured within these zones.

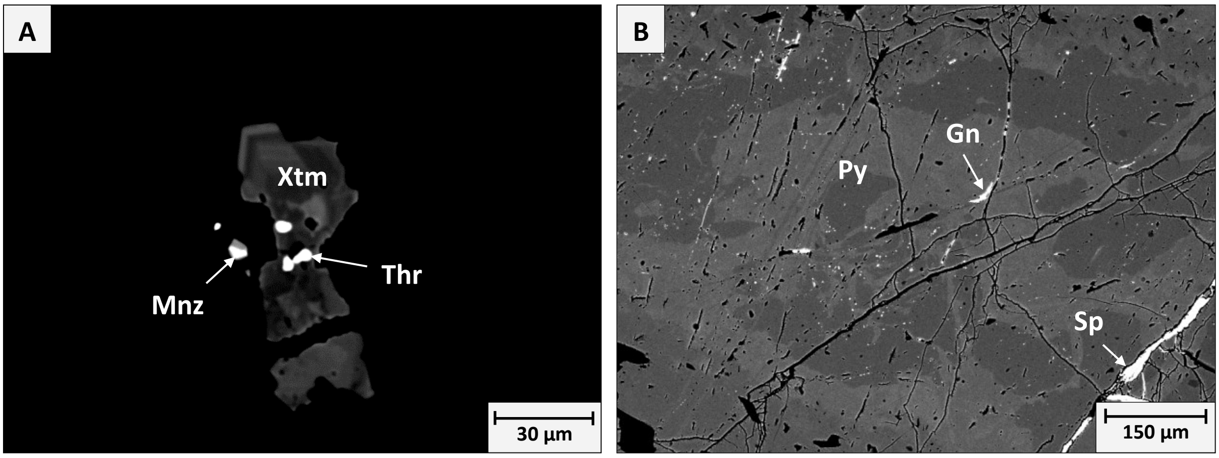

Figure 28: Sample PM-IM-03 (Imhof); A) BSE image showing a hypidiomorphic xenothime (Xtm) crystal with inclusions of small (< 10 µm) thorite (Thr) crystals next to a monazite (Mnz); B) BSE image showing a xenomorphic pyrite (Py) with a very irregular zonation and inclusions of galena (Gn) and sphalerite (Sp).

PM-SZ-01

This polished section consists mainly of pyrite and arsenopyrite, which are already macroscopically visible. These are homogeneously distributed in the polished section. Both the pyrites and the arsenopyrites are mostly hypidiomorphic, partly idiomorphic or xenomorphic and have straight to rounded crystal boundaries (Figure 29A). The pyrites reach sizes of up to 2 mm while the arsenopyrites reach sizes of up to 1.5 mm. In addition, the arsenopyrites are more frequently cracked compared to the pyrites. Both galena and its alteration products anglesite and cerussite can be found in the cracks of pyrite and arsenopyrite. The galena is also occasionally present as very fine inclusions (< 1 µm). electrum is also present as an accessory inclusion in the pyrite or within the cracks. The electrum has a maximum size of 100 µm and has rounded crystal boundaries (Figure 29B). Very fine cracks which protrude from the electrum crystal into the pyrite are also filled with electrum (Figure 29B). The measurement with the SEM revealed a composition of 67 atom% gold and 34 atom% silver on average. A zonation within the pyrites is not visible.

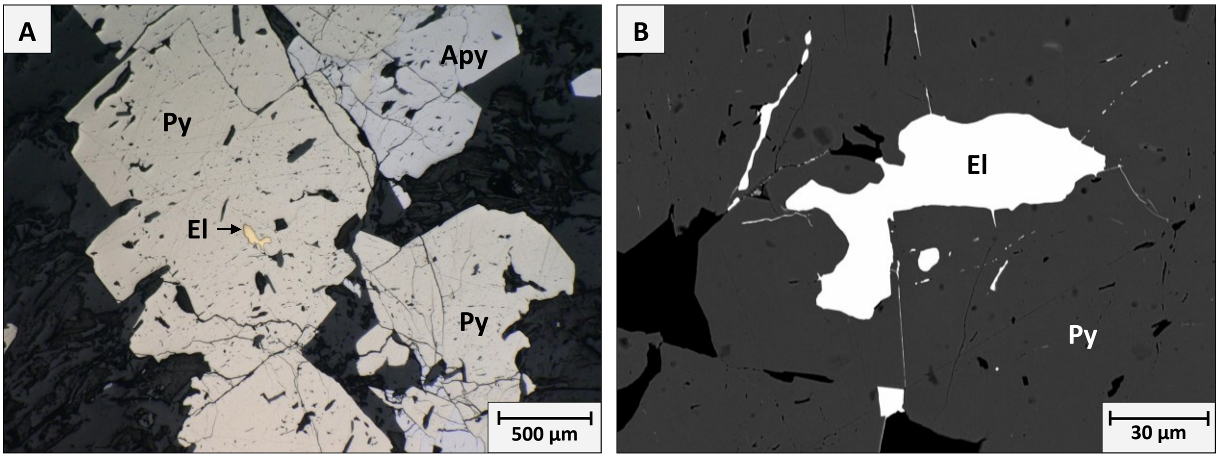

Figure 29: Sample PM-SZ-01 (Siglitz); A) Hypidiomorphic pyrite (Py) and arsenopyrite (Asp) partly intergrow. Small (< 60 µm) electrum (El) crystal as an inclusion within the pyrite (py); B) BSE image showing a close-up image of the electrum (El), revealing fine cracks around the crystal which are also mineralized with electrum (El).

3.2.8 BOCKHART

21TG27

Macroscopically, the minerals contained within the polished section are difficult to identify. The structure of the section is very complex and heterogeneous. A zone can be identified in which there are mainly very fine arsenopyrite crystals and medium-sized pyrites. The section consists mainly of gangue minerals. The majority of the ore minerals are pyrite and arsenopyrite. Compared to the arsenopyrites, the pyrites tend to be rounded and have rounded to bay-shaped crystal boundaries. In addition, they are xenomorphic and often crisscrossed by cracks or fractured (Figure 30A). Galena and sphalerite can be found within these cracks. The pyrites often have small inclusions (< 10 µm) of chalcopyrite and reach sizes of up to 500 µm. The arsenopyrites, on the other hand, are mostly idiomorphic and very small (< 100 µm), only occasionally crystals up to one mm in size can be seen (Figure 30B). Like the pyrites, the larger arsenopyrites have more cracks in which galena and sometimes sphalerite can be found. The smaller ones, on the other hand, have fewer cracks. A electrum crystal can be seen within the crack of an arsenopyrite, which is surrounded by galena. The measurement with the SEM shows a composition of 20.73 atom% gold and 79.27 atom% silver. An ilmenite crystal was also found within the zone of very fine-grained arsenopyrite. This is xenomorphic, has rounded crystal boundaries and a size of 50 µm. The gangue minerals consist of quartz and feldspar.

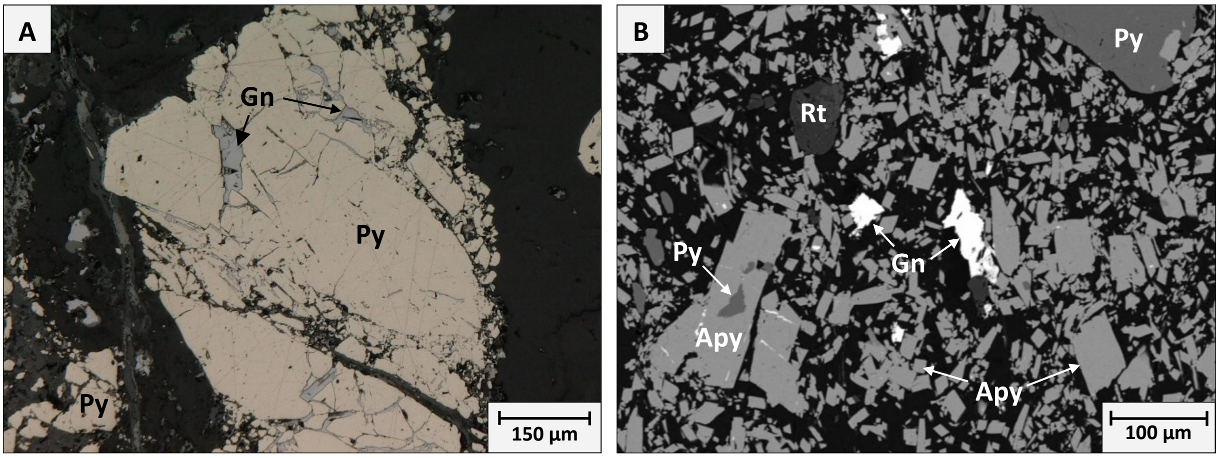

Figure 30: Sample 21TG27 (Bockhart); A) Xenomorphic pyrite (Py) fractured and perverted by cracks which are partly filled by galena (Gn); B) BSE image showing xenomorphic pyrite (Py), rutile (Rt) and galena (Gn) surrounded by a matrix of idiomorphic arsenopyrites (Asp) and gangue minerals.

21TG57

This sample consists mainly of gangue minerals. The ore minerals consist mainly of pyrite, arsenopyrite and chalcopyrite. Galena is present as a minor component. The pyrites are xenomorphic, have rounded and bay-shaped crystal boundaries and are often fractured or cracked. They also contain numerous inclusions of chalcopyrite, arsenopyrite and galena (Figure 31A). The galena and chalcopyrite are both xenomorphic, have irregular crystal boundaries and can also be found within the cracks of pyrite and arsenopyrite (Figure 31B). The arsenopyrite is idiomorphic to hypidiomorphic and has straight to rounded crystal boundaries. Both arsenopyrite and pyrite reach sizes of up to 1 mm. Zonations within the pyrites are minimally recognizable (Figure 31B). The gangue minerals consist of quartz and feldspar.

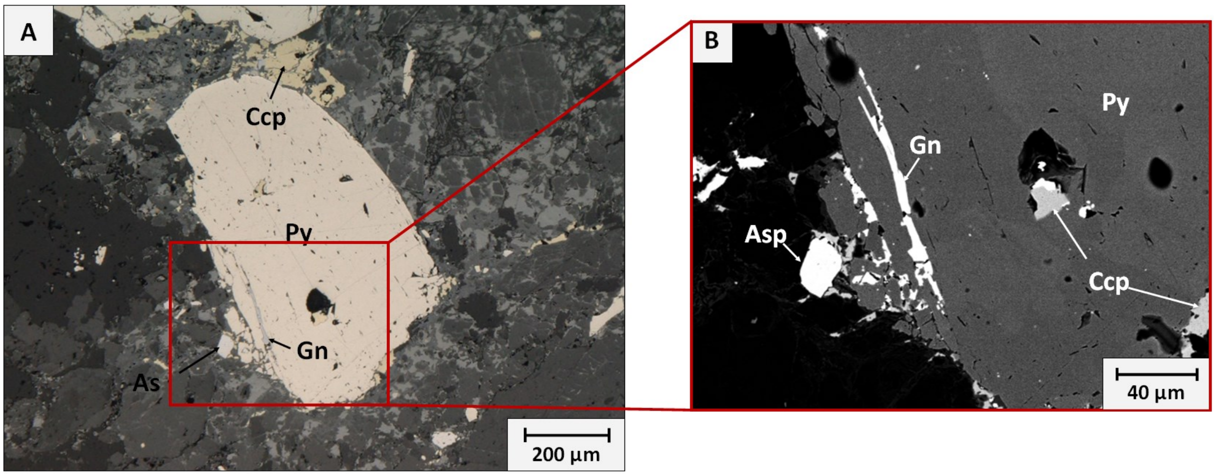

Figure 31: Sample 21TG57 (Bockhart); A) Xenomorphic pyrite (Py) with inclusions of chalcopyrite (Ccp) and galena (Gn). Idiomorphic arsenopyrite (Asp) at the edge; B) BSE image showing a close-up image of the left bottom side of the pyrite (Py) showing the with galena (Gn) filled cracks and chalcopyrite (Ccp) inclusions in detail.

3.2.9 ERZWIES

A1740

Unlike the other samples, this one consists mainly of sphalerite. This is easily recognizable due to its dark grey-brown color. It is also xenomorphic and already heavily fractured with cracks running through it. The crystals reach sizes of more than 2 mm. Within the sphalerite, small chalcopyrite aggregates are recognizable which are aligned or randomly distributed but are concentrated around the cracks in the larger specimens (Figure 32A). These show a granular habit and have rounded crystal boundaries in contact with sphalerite. In addition, chalcopyrite only occurs in contact with the sphalerite. Furthermore, idiomorphic to hypidiomorphic pyrites can be recognized which are arranged in bands. The pyrites usually contain inclusions of sphalerite and galena and have straight to rounded crystal boundaries. The pyrites can be divided into two types. The first type where the pyrites are arranged as a band close to the sphalerites. These also only have inclusions of sphalerite. The second type, where the pyrites are intergrown with the galena and contain numerous inclusions of galena (Figure 32B). Only a few sphalerite crystals can be seen in this area. These are in contact with straight crystal boundaries to the galena and contain finely dispersed chalcopyrite crystals. Idiomorphic quartz crystals are also recognizable, which have straight crystal boundaries to galena as well as pyrite and sphalerite. Lead oxides such as cerussite within the cracks of sphalerite can be identified. Within the pyrites a light zonation is visible (Figure 32B).

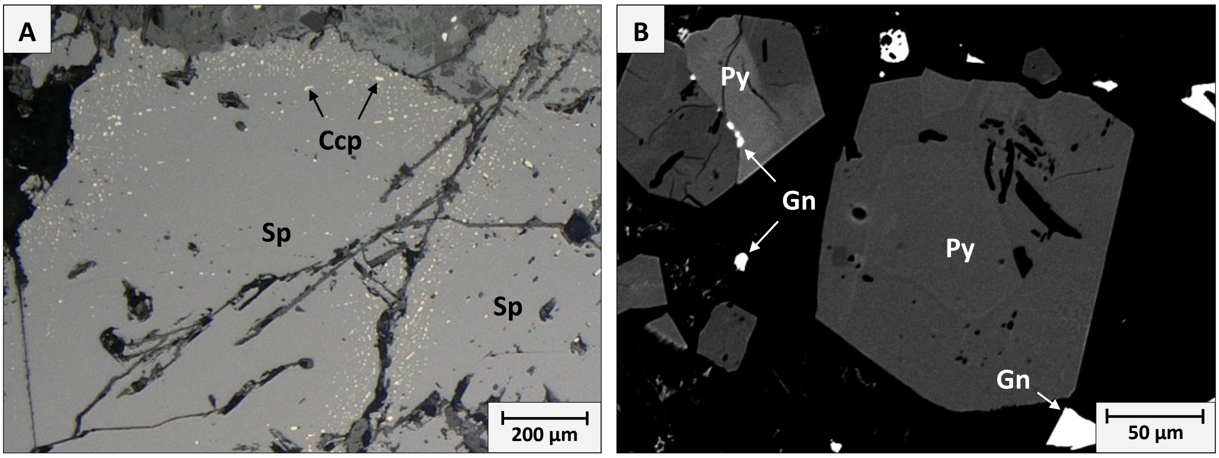

Figure 32: Sample A1740 (Erzwies); A) Xenomorphic sphalerite (Sp) perverted by cracks and small chalcopyrite (Ccp) aggregates aligned or randomly distributed but concentrated around the cracks within the sphalerite (Sp); B) BSE image showing idiomorphic pyrite (Py) crystals with an irregular zonation and galena (Gn) partly as inclusions within the pyrite (Py).

A1742

This polished section is similar to A1740. Pyrite, galena and sphalerite can already be seen macroscopically. Other minerals contained in the sample are chalcopyrite, Fe-Mn oxide and Sb-Ag-Cu sulfosalts. The polished section can be divided into a galena-rich side and a pyrite- and sphalerite-rich side (Figure 33A). The galena-rich siderite consists mainly of large galena crystals with sizes over 2 mm. These are xenomorphic, have rounded and bay-shaped crystal boundaries and are interspersed with cracks. Occasionally, small inclusions of pyrite, sphalerite and Sb-Ag-Cu sulfosalts can be seen at the edge of the galena (Figure 33B). All three minerals have rounded crystal boundaries and are smaller than 200 µm (Figure 33C). The other side of the polished section (left) mainly of a cluster of xenomorphic and hypidiomorphic pyrites, which are intergrown, and large (> 2 mm) sphalerite crystals. Both minerals have rounded and straight crystal boundaries. Isolated pyrites can also be observed occasionally. Galena and chalcopyrite are also present. The galena is in contact with pyrite and sphalerite and has straight and rounded crystal boundaries. It has a size of 2 mm. The pyrites are mostly interspersed with cracks and have inclusions of sphalerite and fine-grained galena. A slight patchy zonation can be seen within the pyrites. All the sphalerites in the section show chalcopyrite disease. The large sphalerites also contain inclusions of galena.

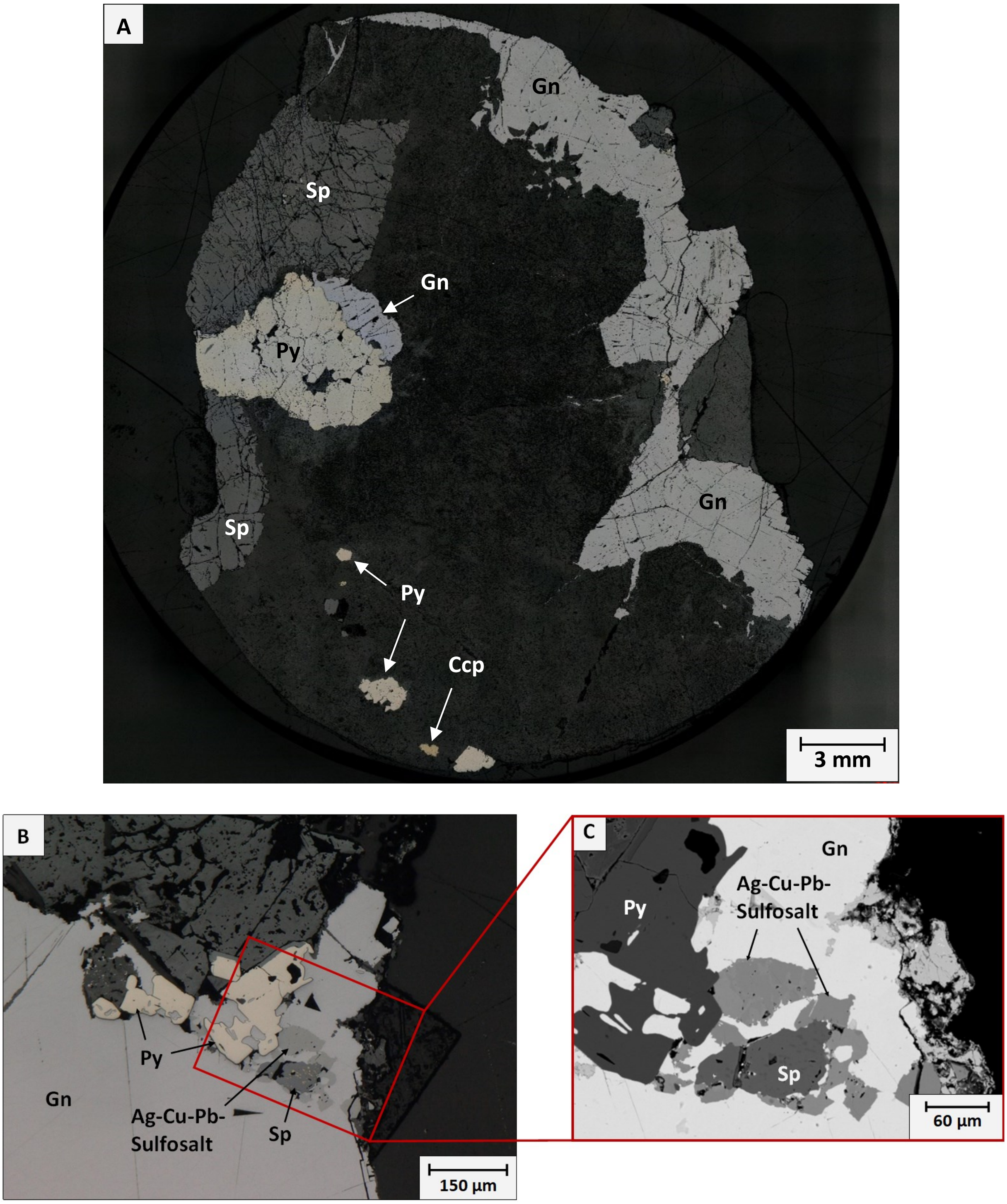

Figure 33: Sample A1742 (Erzwies); A) Overview image showing a galena-rich side (right) and a pyrite- and sphalerite-rich side (left); B) Pyrite (Py), Sphalerite (Sp) and Ag-Cu-Pb-sulfosalt within galena (Gn) on the galena-rich side; C) BSE image showing a close-up image of the Ag-Cu-Pb-sulfosalt in contact with the pyrite (py), sphalerite (Sp) and galena (Gn).

3.2.10 RADHAUSBERG

PM-RB-04a

Some of the different mineral phases can already be recognized macroscopically. Pyrite and arsenopyrite are the main components of the polished section. The pyrite crystals are mostly hypidiomorphic, but occasionally also xenomorphic or idiomorphic and reach sizes of up to 2 mm. They are also slightly anisotropic and have straight to rounded crystal boundaries (Figure 34A). Some of the crystals are intergrown. The pyrites are not in contact with the arsenopyrites, which appear whiter under the reflected light microscope (Figure 34A). While the pyrites are mostly intact, most arsenopyrites are heavily altered and riddled with cracks. The crystal boundaries are usually rounded and straight (Figure 34A). In addition, the pyrites and arsenopyrites don't appear together, but are divided into zones in which either pyrite or arsenopyrite is found. Noticeable are the dark grey almost black phases which can be seen at the edge or between the arsenopyrites within the cracks. These phases were identified with the SEM as iron hydroxides. The chalcopyrite is xenomorph, perforated and has bay-shaped crystal boundaries (Figure 34A). It occurs more frequently in the surrounding area of arsenopyrite. It also has a stockwork-like texture in the cracks between the arsenopyrites (Figure 34A). Chalcopyrite can also be observed occasionally as inclusions in pyrite, if there is also chalcopyrite around the pyrite. Galena is clearly recognizable by its triangular pits. It only occurs in a few areas with sizes of up to 1 mm and has rounded to bay-shaped crystal boundaries. It can also be observed as inclusions in pyrite and in cracks in both pyrite and arsenopyrite. Zonations are present within the pyrites. In xenomorphic pyrites these tend to be patchy and in idiomorphic crystals they follow the crystal boundaries (Figure 34B).

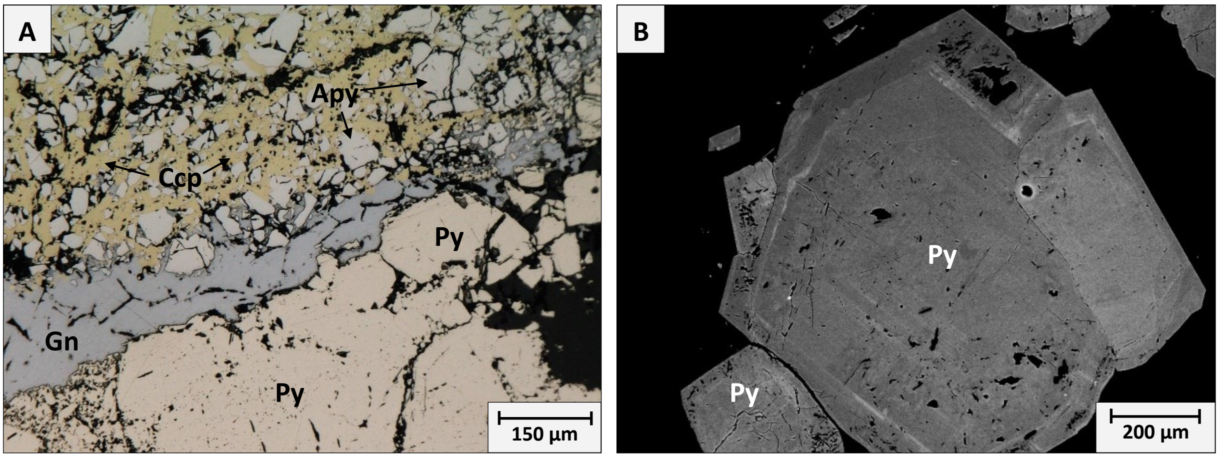

Figure 34: Sample PM-RB-04a (Radhausberg); A) Showing an area with xenomorphic pyrite (Py) and an area with xenomorphic arsenopyrite (Asp) which is surrounded by chalcopyrite (Ccp). In between both areas galena (Gn) is present; B) BSE image showing an idiomorphic pyrite (Py) crystal with distinct concentric zonation.

PM-RB-07

This section can already be divided macroscopically into two areas. Microscopically, there is a pyrite-rich and an arsenopyrite-rich area (Figure 35A). The pyrites are xenomorphic, hypidiomorphic and idiomorphic and therefore have straight to rounded crystal boundaries. In addition, the pyrites are often intergrown and reach sizes of up to 2 mm. Near the arsenopyrite-rich area, more inclusions of arsenopyrite can be observed in the pyrites (Figure 35A). Furthermore, three small electrum crystals are present as inclusions in the pyrite. The SEM measurement yielded 74.71 atom% gold and 25.29 atom% silver. These are a maximum of 15 µm in size. The arsenopyrites are mostly xenomorphic, only occasionally hypidiomorphic and intergrown. They are also heavily decomposed and have several cracks running through them (Figure 35A). The maximum size of the arsenopyrites is 1 mm. White-greyish inclusions can be seen within these, which could be identified as sulfosalts using SEM. More precisely, these are several phases of sulfosalts that are intergrown. They are mostly bismuthinite with inclusions of Cu-Pb-Bi sulfosalts (junoite), Ag-Pb-Bi-sulfosalts (erzwiesite) and occasionally galena (Figure 35C-F). This bismuthite reach maximum sizes of 400 µm and are only found within arsenopyrites. In addition, Fe and P-rich aluminum oxides can be found within the cracks of arsenopyrites, less so in pyrite. These show a strong zoning with sometimes Fe-rich, sometimes Al-rich zones. Furthermore, two monazite crystals with slight zoning can be observed. The pyrites show strong zonations which are parallel to the crystal boundaries (Figure 35B). The ore minerals are surrounded by quartz, feldspars, muscovite and calcite.

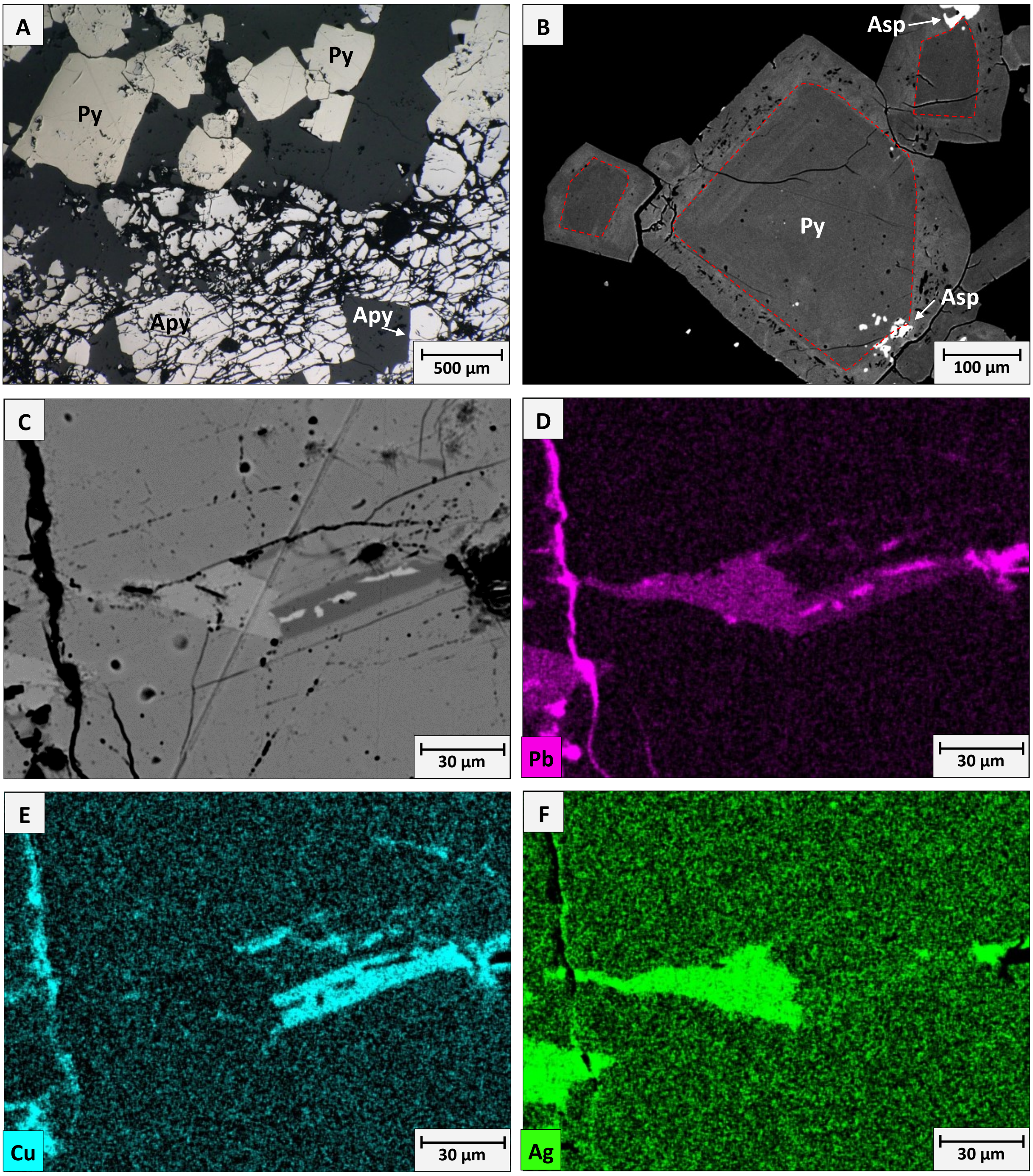

Figure 35: Sample PM-RB-07 (Radhausberg); A) Showing an area with idiomorphic pyrite (Py) crystals and an area with xenomorphic arsenopyrite (Asp) pervaded by cracks; B) BSE image showing a idiomorphic pyrite (Py) crystal with distinct concentric zonation and inclusions of arsenopyrite (Asp); C) BSE image showing galena and different sulfosalts within the arsenopyrite (Asp); D) SEM mapping of the element Pb; E) SEM mapping of the element Cu; F) SEM mapping of the element Ag.

3.2.11 ROTGÜLDEN

PM-RG-01

This polished section is clearly different from the others. It can already be seen macroscopically that it consists mainly of chalcopyrite and pyrrhotite. In addition, the electrum crystal can be seen macroscopically. Both the chalcopyrites and the pyrrhotites form clusters larger than 2 mm, are crisscrossed by cracks and have some outbreaks. Both minerals are xenomorphic and usually have rounded, sometimes even straight crystal boundaries in contact with each other and with other minerals. Microscopically, small medium-grey phases (< 50 µm) can be seen which have been identified as sphalerite. Two different sphalerites can be recognized: (1) Iron-rich (8-10 atom% Fe) sphalerite, which has a homogeneous distribution throughout the section and is present as an inclusion within pyrrhotite and chalcopyrite. It is also medium gray and sometimes forms sphalerite stars within the chalcopyrite (Figure 36A). (2) Iron-poor sphalerite, which is up to 100 µm in size, has a lower reflectivity and inclusions of fine chalcopyrite aggregates (chalcopyrite disease). The two electrum crystals contained in the sample are electrum with an average composition of 44.97 atom% silver and 55.03 atom% gold. The largest electrum crystal reaches a size of up to 500 µm (Figure 36B). The crystal boundaries are mostly rounded to bay-shaped. The crystals are found as inclusions within pyrrhotite. The cracks in the pyrrhotite surrounding the large electrum crystal are filled with silver (Figure 36B). Inclusions of silver, galena, bismuth, acanthite, matildite, stannite and cassiterite can be found within the pyrrhotite and chalcopyrite and at the edges of the crystals (Figure 36C-F). These are always smaller than 100 µm. The gangue material consists of idiomorphic, stalky quartz with occasional xenomorphic apatite and iron hydroxides.

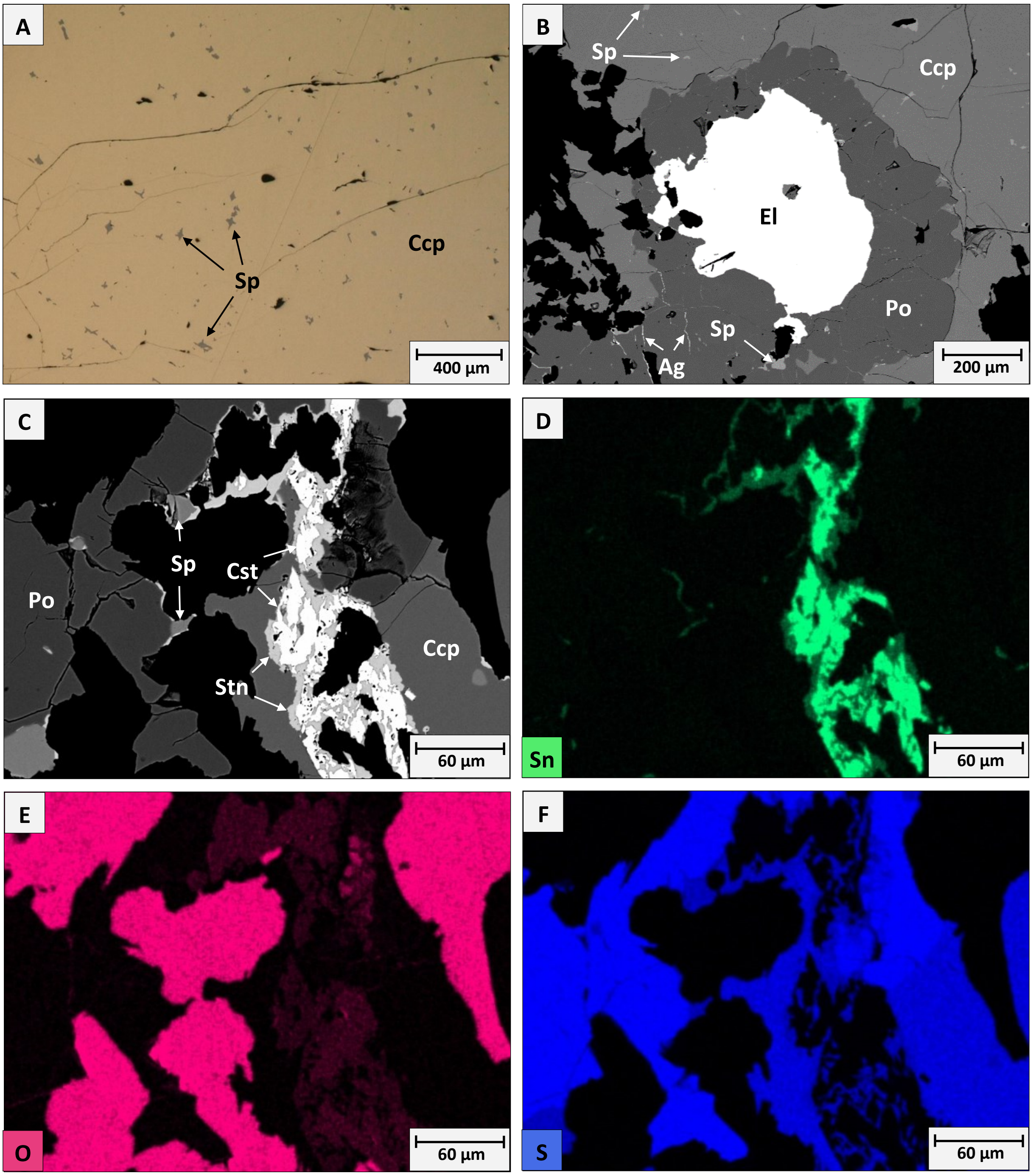

Figure 36: Sample PM-RG-01 (Rotgülden); A) Showing sphalerite (Sp) stars within the chalcopyrite (Ccp); B) BSE image of the ~500 µm sized electrum (El) crystal rimmed by a corona of pyrrhotite (Po) with silver (Ag) filled cracks within the pyrrhotite (Py). This corona is surrounded by chalcopyrite (Ccp); C) BSE image of cassiterite (Cst) surrounded by stannite (Stn) at the edges of chalcopyrite (Ccp) and pyrrhotite (Po); D) SEM mapping of the element Sn; E) SEM mapping of the element O; F) SEM mapping of the element S.

PM-RG-03

This sample is characterized by its macroscopically recognizable, xenomorphic, hypidiomorphic, and partly idiomorphic, large pyrite crystals. These have straight and rounded crystal boundaries and reach sizes of up to 2.5 mm. They are often intergrown and interspersed with fine cracks. Pyrrhotite and chalcopyrite can be found as inclusions within the pyrites (Figure 37A). These have a rather granular habit with straight to rounded crystal boundaries and a maximum size of 100 µm (Figure 37A). Chalcopyrite, in particular, is often finely distributed within the pyrite. The pyrites also have inclusions of iron hydroxides, quartz and calcite. Minerals such as hydroxyapatite and iron hydroxides can be found at the edge of the pyrites. The apatites, quartz and calcites are mostly xenomorphic but occasionally also hypidiomorphic to idiomorphic. Within the pyrites, zonations are visible, which have a different structure. Both parallel growth zonations (Figure 37B) and patchy, irregular zonations are present. The ore minerals are surrounded by a mixture of quartz and calcite/dolomite.

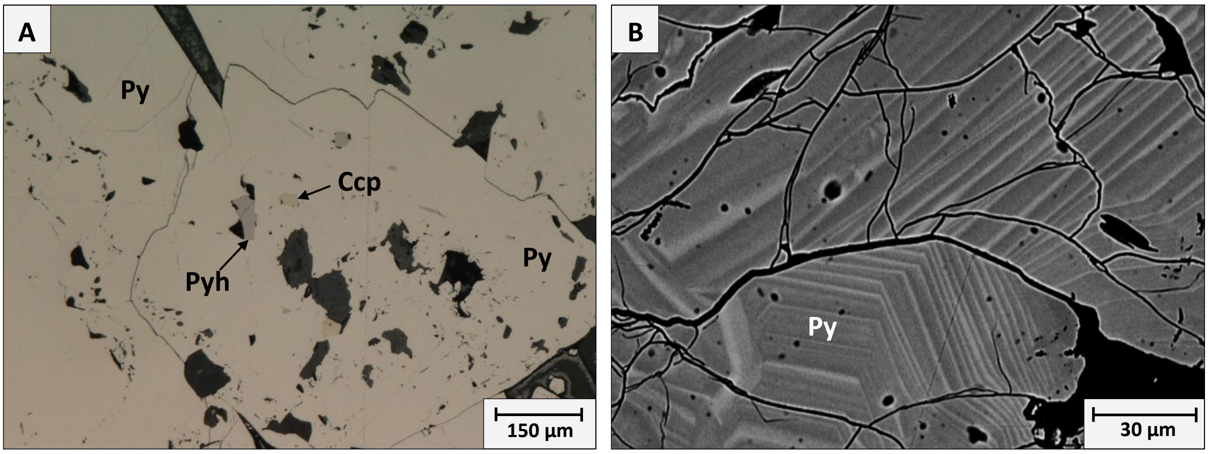

Figure 37: Sample PM-RG-03 (Rodgülden); A) Showing pyrite (Py) with inclusions of pyrrhotite (Po) and chalcopyrite (Ccp); B) BSE image showing pyrite (Py) with parallel growth zonations.

3.2.12 SCHELLGADEN

A1870

This polished section shows a rather homogeneous distribution of minerals. The minerals pyrite and galena can already be recognized macroscopically. These make up the majority of the ore minerals in this section. Other identified minerals are chalcopyrite, covelline, electrum, anglesite, quartz and muscovite. The pyrites and galena are hypidiomorphic and xenomorphic and have straight to rounded crystal boundaries (Figure 38A). The pyrites are often very strongly rounded. They contain few inclusions of galena or chalcopyrite and reach sizes of up to 1 mm. One pyrite crystal, which is surrounded in some areas by a mixture of galenite, anglesite, and covelline (Figure 38B). The galenite in this sample reaches a size of approximately 800 µm. Seams of anglesite, a alteration product of galena, are often found at the edge to galena. In some areas, the anglesite is intergrown with very fine-grained covelline (Figure 38B). The covelline can be clearly identified by its intense blue color. This can usually be observed at the edge of chalcopyrite as an alteration product. The crystal boundaries between covelline and chalcopyrite are fibrous and irregular. In contact with anglesite, the covelline has straight and rounded crystal boundaries. In this case, the covelline reaches a maximum size of 50 µm. The electrum crystals in this section are in contact with both pyrite and galena (Figure 38A). The measurement with the SEM showed an average composition of 22.53 atom% silver and 77.47 atom% gold. A minimum of 7 visible electrum crystals have been found with largest crystal having a size of approx. 400 µm.

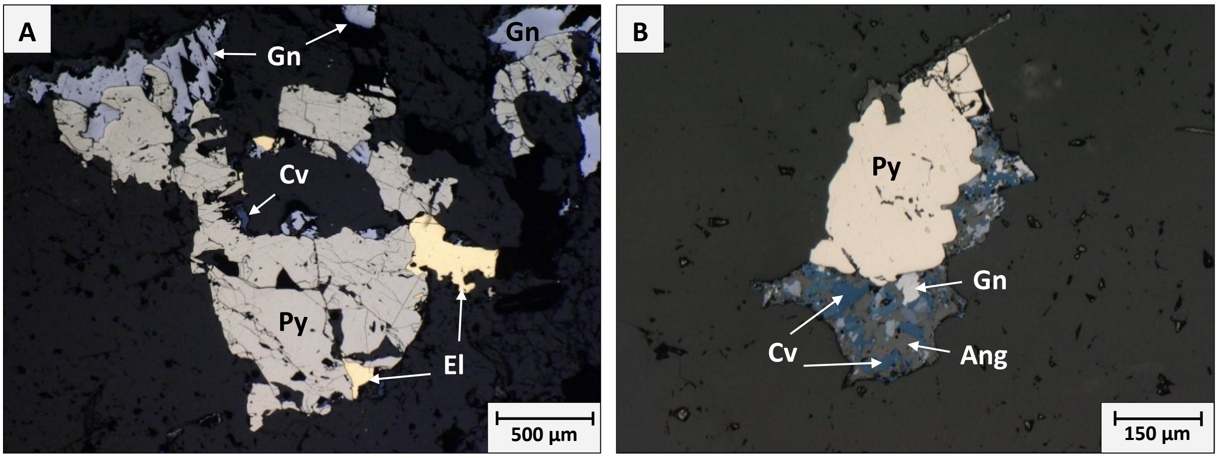

Figure 38: Sample A1980 (Schellgaden); A) Showing xenomorphic pyrite (Py) in contact with galena (Gn), covelline (Cv) and electrum (El); B) Showing pyrite (Py) partly surrounded by a mixture of covelline (Cv), galena (Gn) and its alteration product anglesite (Ang).

A1979

The minerals pyrite and galena are already macroscopically recognizable. Other minerals identified microscopically are chalcopyrite, barytes, electrum, quartz, calcite and muscovite. The pyrites in this polished section tend to differ from those in the other cuts. They are all xenomorphic, often strongly rounded with rounded and bay-shaped crystal boundaries (Figure 39A). The pyrites reach sizes of up to 1.5 mm. Next to the electrum, the pyrites appear in a rather yellow-greyish color with a slight greenish touch (Figure 39A). The pyrites are evenly distributed in the sample and have slight differences in size. They are often crisscrossed by cracks and contain inclusions. The cracks are mostly filled with galena, chalcopyrite, gangue minerals as well as electrum (Figure 39B). Apart from the electrum, the other minerals can also be found as inclusions in the pyrite. Almost no zoning is recognizable, only one pyrite crystal shows a slight spotty zoning. The electrum is contained in the sample as visible free electrum and has an average composition of 77.55 atom% Au and 22.45 atom% Ag. It reaches sizes of up to 400 µm and is mostly in contact with galena and can be found in the cracks of pyrite. The crystal boundaries between the electrum and the other minerals are straight to rounded. Noticeable is a zonation within one of the electrum crystals, which is caused by different Au:Ag ratios (Figure 39C). Chalcopyrite is only found as inclusions in pyrite or within cracks. Barite is only found as inclusions within pyrites with a maximum size of 70 µm (Figure 39B). Galena is present both as a isolated mineral and as inclusions within pyrites and as fissure filling. It shows the typical triangular pits and has straight, rounded as well as bay-shaped crystal boundaries. Galena acts as a kind of gap filler. It has a serial crystal size distribution with very large crystals (~1 mm) to very small crystals (< 10 µm). The galena inclusions in the pyrite can be as small as 1 µm. The surrounding minerals consist mainly of quartz, dolomite-ankerite mixing series and occasionally muscovite.

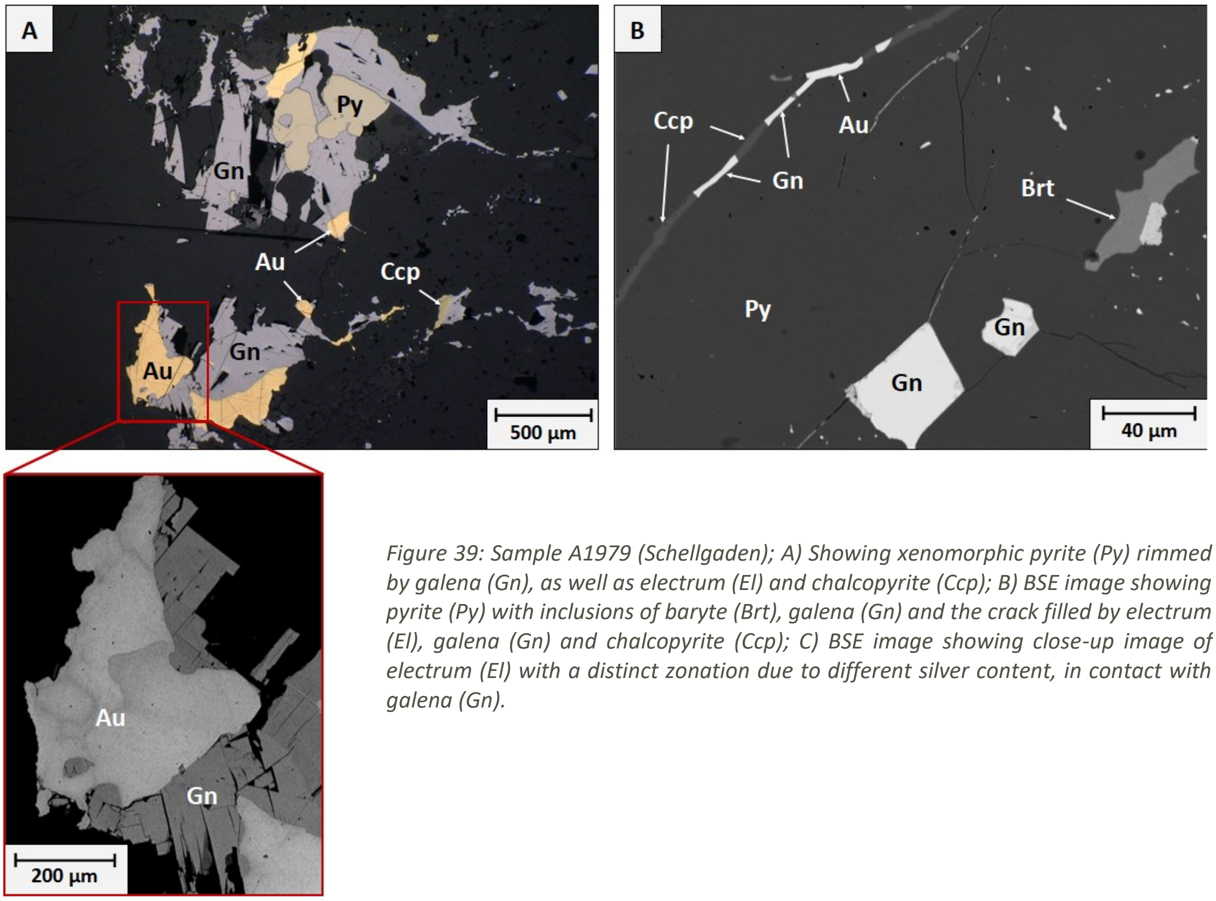

Figure 39: Sample A1979 (Schellgaden); A) Showing xenomorphic pyrite (Py) rimmed by galena (Gn), as well as electrum (El) and chalcopyrite (Ccp); B) BSE image showing pyrite (Py) with inclusions of baryte (Brt), galena (Gn) and the crack filled by electrum (El), galena (Gn) and chalcopyrite (Ccp); C) BSE image showing close-up image of electrum (El) with a distinct zonation due to different silver content, in contact with galena (Gn).

3.3 LASER ABLATION (LA-ICP-MS)

In this work, in-situ point analyses were carried out both in the pyrite and in the visible gold crystals. An attempt was made to measure 20 points in the pyrite in each cut. However, due to a “pollution effect” of the LA-ICP-MS by arsenopyrite and galena, pyrites with numerous inclusions of these minerals were avoided and some specimens showed only small amounts of pyrite, so that less than 20 points were measured in some specimens (21TG57, A1742, A1462, A1370 and PM-MS-02). Two to seven points were measured per pyrite, depending on the size of the pyrite. In addition, attention was paid to setting the points in a linear line from the pyrite edge to the core with regard to the zonation (if recognizable). In the sections PM-RG-01 (Rotgülden), PM-PA-05b (Pasterze) and A1510 (Hierzbach-Schiedalpe) no or too small pyrites were present, which is why no measurements from these sections are available. The measurement values are given in ppm (parts per million).

In five cuts, the gold crystals were large enough for a measurement. A total of 14 measurements were carried out in gold crystals. Most of the measurements (five measurements) were carried out in PM-RG-01 (Rotgülden). As no standards were used for the gold measurements, the results are given in counts per second (cps).

The pyrite measurement data was processed using the Iolite software. The elements of each measurement point that are the result of micro inclusions were eliminated. The data is analyzed with correlation plots and scatter plots for a regional comparison.

3.3.1 LASER ABLATION OF PYRITES

In the following correlation matrices, all values of the measurement are plotted against each other in order to recognize which values correlate with each other. All values were used here without subdividing them into the individual districts. As there are only a few values for some elements in some districts, many of the correlation matrices are not very expressive.

Figure 40A plots all values excluding inclusions and Figure 40B plots all values including inclusions. There are significant differences between these two correlation matrices. Figure 40A shows clear correlations between Cr/V and Sn/In with values above 0.8. Further significant correlations can be seen between Ga/Ge, Mo/Ge, Te/Ga, Te/Ge, Au/As, Cd/Ag, Tl/Sb, Pb/Bi and Ni/Co. In addition, anti-correlations can be seen to a lesser extent, such as between nickel and arsenic. The matrix in Figure 40B, on the other hand, shows many more correlations with much higher values

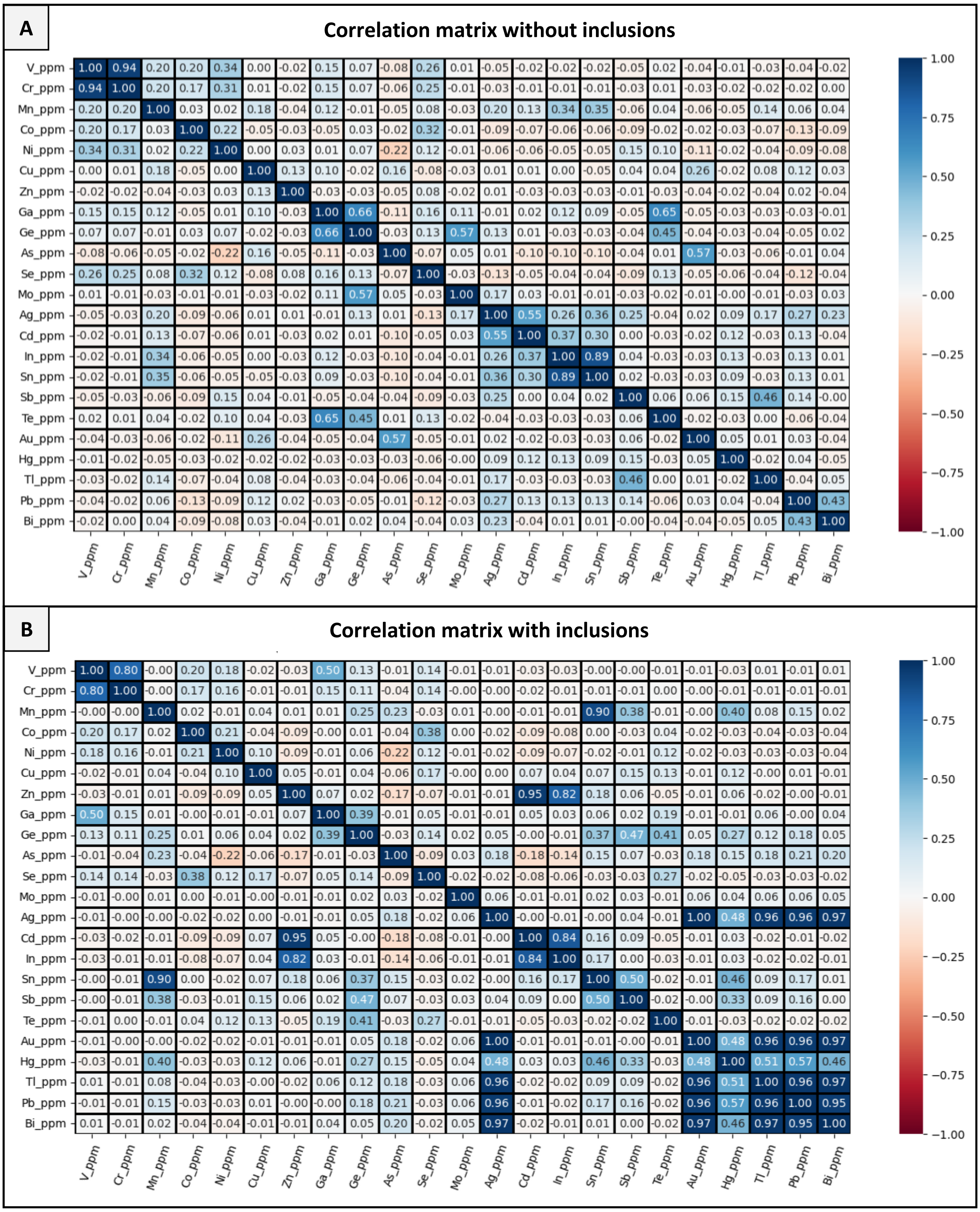

A Correlation matrix without inclusions

	V_ppm	Cr_ppm	Mn_ppm	Co_ppm	Ni_ppm	Cu_ppm	Zn_ppm	Ga_ppm	Ge_ppm	As_ppm	Se_ppm	Mo_ppm	Ag_ppm	Cd_ppm	In_ppm	Sn_ppm	Sb_ppm	Te_ppm	Au_ppm	Hg_ppm	Tl_ppm	Pb_ppm	Bi_ppm
V_ppm	1.00	0.94	0.20	0.20	0.34	0.00	-0.02	0.15	0.07	-0.08	0.26	0.01	-0.05	-0.02	-0.02	-0.02	-0.05	0.02	-0.04	-0.01	-0.03	-0.04	-0.02
Cr_ppm	0.94	1.00	0.20	0.17	0.31	0.01	-0.02	0.15	0.07	-0.06	0.25	-0.01	-0.03	-0.01	-0.01	-0.01	-0.03	0.01	-0.03	-0.02	-0.02	-0.02	0.00
Mn_ppm	0.20	0.20	1.00	0.03	0.02	0.18	-0.04	0.12	-0.01	-0.05	0.08	-0.03	0.20	0.13	0.34	0.35	-0.06	0.04	-0.06	-0.05	0.14	0.06	0.04
Co_ppm	0.20	0.17	0.03	1.00	0.22	-0.05	-0.03	-0.05	0.03	-0.02	0.32	-0.01	-0.09	-0.07	-0.06	-0.06	-0.09	-0.02	-0.02	-0.03	-0.07	-0.13	-0.09
Ni_ppm	0.34	0.31	0.02	0.22	1.00	0.00	0.03	0.01	0.07	-0.22	0.12	-0.01	-0.06	-0.06	-0.05	-0.05	0.15	0.10	-0.11	-0.02	-0.04	-0.09	-0.08
Cu_ppm	0.00	0.01	0.18	-0.05	0.00	1.00	0.13	0.10	-0.02	0.16	-0.08	-0.03	0.01	0.01	0.00	-0.05	0.04	0.04	0.26	-0.02	0.08	0.12	0.03
Zn_ppm	-0.02	-0.02	-0.04	-0.03	0.03	0.13	1.00	-0.03	-0.03	-0.05	0.08	-0.02	0.01	-0.03	-0.03	-0.03	-0.01	-0.03	-0.04	-0.02	-0.04	0.02	-0.04
Ga_ppm	0.15	0.15	0.12	-0.05	0.01	0.10	-0.03	1.00	0.66	-0.11	0.16	0.11	-0.01	0.02	0.12	0.09	-0.05	0.65	-0.05	-0.03	-0.03	-0.03	-0.01
Ge_ppm	0.07	0.07	-0.01	0.03	0.07	-0.02	-0.03	0.66	1.00	-0.03	0.13	0.57	0.13	0.01	-0.03	-0.03	-0.04	0.45	-0.04	-0.03	-0.04	-0.05	0.02
As_ppm	-0.08	-0.06	-0.05	-0.02	-0.22	0.16	-0.05	-0.11	-0.03	1.00	-0.07	0.05	0.01	-0.10	-0.10	-0.10	-0.04	0.01	0.57	-0.03	-0.06	-0.01	0.04
Se_ppm	0.26	0.25	0.08	0.32	0.12	-0.08	0.08	0.16	0.13	-0.07	1.00	-0.03	-0.13	-0.05	-0.04	-0.04	-0.09	0.13	-0.05	-0.06	-0.04	-0.12	-0.04
Mo_ppm	0.01	-0.01	-0.03	-0.01	-0.01	-0.03	-0.02	0.11	0.57	0.05	-0.03	1.00	0.17	0.03	-0.01	-0.01	-0.03	-0.02	-0.01	-0.00	-0.01	-0.03	0.03
Ag_ppm	-0.05	-0.03	0.20	-0.09	-0.06	0.01	0.01	-0.01	0.13	0.01	-0.13	0.17	1.00	0.55	0.26	0.36	0.25	-0.04	0.02	0.09	0.17	0.27	0.23
Cd_ppm	-0.02	-0.01	0.13	-0.07	-0.06	0.01	-0.03	0.02	0.01	-0.10	-0.05	0.03	0.55	1.00	0.37	0.30	0.00	-0.03	-0.02	0.12	-0.03	0.13	-0.04
In_ppm	-0.02	-0.01	0.34	-0.06	-0.05	0.00	-0.03	0.12	-0.03	-0.10	-0.04	-0.01	0.26	0.37	1.00	0.89	0.04	-0.03	-0.03	0.13	-0.03	0.13	0.01
Sn_ppm	-0.02	-0.01	0.35	-0.06	-0.05	-0.05	-0.03	0.09	-0.03	-0.10	-0.04	-0.01	0.36	0.30	0.89	1.00	0.02	-0.03	-0.03	0.09	-0.03	0.13	0.01
Sb_ppm	-0.05	-0.03	-0.06	-0.09	0.15	0.04	-0.01	-0.05	-0.04	-0.04	-0.09	-0.03	0.25	0.00	0.04	0.02	1.00	0.06	0.06	0.15	0.46	0.14	-0.00
Te_ppm	0.02	0.01	0.04	-0.02	0.10	0.04	-0.03	0.65	0.45	0.01	0.13	-0.02	-0.04	-0.03	-0.03	-0.03	0.06	1.00	-0.02	-0.03	0.00	-0.06	-0.04
Au_ppm	-0.04	-0.03	-0.06	-0.02	-0.11	0.26	-0.04	-0.05	-0.04	0.57	-0.05	-0.01	0.02	-0.02	-0.03	-0.03	0.06	-0.02	1.00	0.05	0.01	0.03	-0.04
Hg_ppm	-0.01	-0.02	-0.05	-0.03	-0.02	-0.02	-0.02	-0.03	-0.03	-0.03	-0.06	-0.00	0.09	0.12	0.13	0.09	0.15	-0.03	0.05	1.00	-0.02	0.04	-0.05
Tl_ppm	-0.03	-0.02	0.14	-0.07	-0.04	0.08	-0.04	-0.03	-0.04	-0.06	-0.04	-0.01	0.17	-0.03	-0.03	-0.03	0.46	0.00	0.01	-0.02	1.00	-0.04	0.05
Pb_ppm	-0.04	-0.02	0.06	-0.13	-0.09	0.12	0.02	-0.03	-0.05	-0.01	-0.12	-0.03	0.27	0.13	0.13	0.13	0.14	-0.06	0.03	0.04	-0.04	1.00	0.43
Bi_ppm	-0.02	0.00	0.04	-0.09	-0.08	0.03	-0.04	-0.01	0.02	0.04	-0.04	0.03	0.23	-0.04	0.01	0.01	-0.00	-0.04	-0.04	-0.05	0.05	0.43	1.00

B Correlation matrix with inclusions

	V_ppm	Cr_ppm	Mn_ppm	Co_ppm	Ni_ppm	Cu_ppm	Zn_ppm	Ga_ppm	Ge_ppm	As_ppm	Se_ppm	Mo_ppm	Ag_ppm	Cd_ppm	In_ppm	Sn_ppm	Sb_ppm	Te_ppm	Au_ppm	Hg_ppm	Tl_ppm	Pb_ppm	Bi_ppm
V_ppm	1.00	0.80	-0.00	0.20	0.18	-0.02	-0.03	0.50	0.13	-0.01	0.14	-0.01	-0.01	-0.03	-0.03	-0.00	-0.00	-0.01	-0.01	-0.03	0.01	-0.01	0.01
Cr_ppm	0.80	1.00	-0.00	0.17	0.16	-0.01	-0.01	0.15	0.11	-0.04	0.14	-0.00	-0.00	-0.02	-0.01	-0.01	-0.01	0.00	-0.00	-0.01	-0.01	-0.01	-0.01
Mn_ppm	-0.00	-0.00	1.00	0.02	-0.01	0.04	0.01	0.01	0.25	0.23	-0.03	0.01	-0.00	-0.01	-0.01	0.90	0.38	-0.01	-0.00	0.40	0.08	0.15	0.02
Co_ppm	0.20	0.17	0.02	1.00	0.21	-0.04	-0.09	-0.00	0.01	-0.04	0.38	0.00	-0.02	-0.09	-0.08	0.00	-0.03	0.04	-0.02	-0.03	-0.04	-0.03	-0.04
Ni_ppm	0.18	0.16	-0.01	0.21	1.00	0.10	-0.09	-0.01	0.06	-0.22	0.12	-0.01	-0.02	-0.09	-0.07	-0.02	-0.01	0.12	-0.02	-0.03	-0.03	-0.03	-0.04
Cu_ppm	-0.02	-0.01	0.04	-0.04	0.10	1.00	0.05	-0.01	0.04	-0.06	0.17	-0.00	0.00	0.07	0.04	0.07	0.15	0.13	-0.01	0.12	-0.00	0.01	-0.01
Zn_ppm	-0.03	-0.01	0.01	-0.09	-0.09	0.05	1.00	0.07	0.02	-0.17	-0.07	-0.01	-0.01	0.95	0.82	0.18	0.06	-0.05	-0.01	0.06	-0.02	-0.00	-0.01
Ga_ppm	0.50	0.15	0.01	-0.00	-0.01	-0.01	0.07	1.00	0.39	-0.01	0.05	-0.01	-0.01	0.05	0.03	0.06	0.02	0.19	-0.01	-0.01	0.06	-0.00	0.04
Ge_ppm	0.13	0.11	0.25	0.01	0.06	0.04	0.02	0.39	1.00	-0.03	0.14	0.02	0.05	-0.00	-0.01	0.37	0.47	0.41	0.05	0.27	0.12	0.18	0.05
As_ppm	-0.01	-0.04	0.23	-0.04	-0.22	-0.06	-0.17	-0.01	-0.03	1.00	-0.09	0.03	0.18	-0.18	-0.14	0.15	0.07	-0.03	0.18	0.15	0.18	0.21	0.20
Se_ppm	0.14	0.14	-0.03	0.38	0.12	0.17	-0.07	0.05	0.14	-0.09	1.00	-0.02	-0.02	-0.08	-0.06	-0.03	-0.03	0.27	-0.02	-0.05	-0.03	-0.03	-0.02
Mo_ppm	-0.01	-0.00	0.01	0.00	-0.01	-0.00	-0.01	-0.01	0.02	0.03	-0.02	1.00	0.06	-0.01	-0.01	0.02	0.03	-0.01	0.06	0.04	0.06	0.06	0.05
Ag_ppm	-0.01	-0.00	-0.00	-0.02	-0.02	0.00	-0.01	-0.01	0.05	0.18	-0.02	0.06	1.00	-0.00	-0.01	-0.00	0.04	-0.01	1.00	0.48	0.96	0.96	0.97
Cd_ppm	-0.03	-0.02	-0.01	-0.09	-0.09	0.07	0.95	0.05	-0.00	-0.18	-0.08	-0.01	-0.00	1.00	0.84	0.16	0.09	-0.05	-0.01	0.03	-0.02	-0.01	-0.02
In_ppm	-0.03	-0.01	-0.01	-0.08	-0.07	0.04	0.82	0.03	-0.01	-0.14	-0.06	-0.01	-0.01	0.84	1.00	0.17	0.00	-0.03	-0.01	0.03	-0.02	-0.02	-0.01
Sn_ppm	-0.00	-0.01	0.90	0.00	-0.02	0.07	0.18	0.06	0.37	0.15	-0.03	0.02	-0.00	0.16	0.17	1.00	0.50	-0.02	-0.01	0.46	0.09	0.17	0.01
Sb_ppm	-0.00	-0.01	0.38	-0.03	-0.01	0.15	0.06	0.02	0.47	0.07	-0.03	0.03	0.04	0.09	0.00	0.50	1.00	-0.02	-0.00	0.33	0.09	0.16	0.00
Te_ppm	-0.01	0.00	-0.01	0.04	0.12	0.13	-0.05	0.19	0.41	-0.03	0.27	-0.01	-0.01	-0.05	-0.03	-0.02	-0.02	1.00	-0.01	-0.03	-0.02	-0.02	-0.02
Au_ppm	-0.01	-0.00	-0.00	-0.02	-0.02	-0.01	-0.01	-0.01	0.05	0.18	-0.02	0.06	1.00	-0.01	-0.01	-0.01	-0.00	-0.01	1.00	0.48	0.96	0.96	0.97
Hg_ppm	-0.03	-0.01	0.40	-0.03	-0.03	0.12	0.06	-0.01	0.27	0.15	-0.05	0.04	0.48	0.03	0.03	0.46	0.33	-0.03	0.48	1.00	0.51	0.57	0.46
Tl_ppm	0.01	-0.01	0.08	-0.04	-0.03	-0.00	-0.02	0.06	0.12	0.18	-0.03	0.06	0.96	-0.02	-0.02	0.09	0.09	-0.02	0.96	0.51	1.00	0.96	0.97
Pb_ppm	-0.01	-0.01	0.15	-0.03	-0.03	0.01	-0.00	-0.00	0.18	0.21	-0.03	0.06	0.96	-0.01	-0.02	0.17	0.16	-0.02	0.96	0.57	0.96	1.00	0.95
Bi_ppm	0.01	-0.01	0.02	-0.04	-0.04	-0.01	-0.01	0.04	0.05	0.20	-0.02	0.05	0.97	-0.02	-0.01	0.01	0.00	-0.02	0.97	0.46	0.97	0.95	1.00

Figure 40: A) Correlation matrix of all by LA-ICP-MS measured elements within Pyrite excluding the values of inclusions; B) Correlation matrix of all by LA-ICP-MS measured elements within Pyrite including the values of inclusions.

According to this figure, Au and Ag have a correlation of 1.0. Further correlations with values above 0.9 prevail between Au/Tl, Au/Pb, Au/Bi, Ag/Tl, Ag/Pb, Ag/Bi, Pb/Bi, Tl/Pb, Tl/Bi, Cd/Zn, Sn/Mn. As in Figure 40B, an anti-correlation between Ni and As can be seen here. Additional other anit-correlations can be seen between As/Zn, As/Cd and As/In.

3.3.1.1 Element Correlations without inclusions

Silver and Pb do show a weak correlation to each other. This can be seen specifically within the data of Erzwies (EW), Hoher Goldberg (HG), Bockhart (BH) where the higher the lead content the higher the silver content is (Figure 41A). Silver never exceeds 30 ppm and in almost halve of the measuring points Ag is below detection limit or not plotted due to an inclusion, whereas Pb reaches values of up to 160 ppm. A similar trend can be seen in the correlation of Ag and Au. Here, an increase in Ag content with increasing Au content can be seen in the districts of Bockhart (BH), Hirzbach (HZ) and Hochwurten (HW) (Figure 41B). In contrast, the Hoher Goldberg (HG), Erzwies (EW), Goldzeche (GZ) and Radhausberg (RB) districts in particular show a wide scattering of points due to a lack of correlation (Figure 41B) Silver plotted with Cd, on the other hand, shows a positive correlation where Cd also increases with increasing Ag content. However, only the Goldzeche (GZ) and Erzwies (EW) districts have enough values to make a valid statement (Figure 41C). A tendency to a positive correlation can be seen in the Ag/Bi plot, but only for the Siglitz district. All other districts do not show any correlation (Figure 41D).

Rising Au values with rising As values can be seen in Figure 41E. The values from Hoher Goldberg (HG) are particularly high and show on average a higher Au content with the same As content compared to the values from Radhausberg (RD), Pasterze (PA) and Siglitz (SZ) (Figure 41E). The values from Hochwurten (HW) are widely distributed and show no correlation. The same applies to Erzwies (EW). The values of Schlellgarden are generally very low with values < 1 ppm for gold and < 35 ppm for arsenic.

In Figure 41F the As/Ni plot is displayed. The different districts show different patterns like Schellgaden, Fuscher Wegscheide and Mesenatten, which form cluster. Schellgaden is the only district that shows for all measuring points low As and high Ni contents. The districts Hoher Goldberg, Radhausberg show different nickel values with unchanged As values. All other districts show rather a scattering of values without specific correlation.

Figure 41G shows an irregular distribution of Pb/Co values with no specific trend for all districts.

Except for one point, a tendency with a positive correlation can be seen for the Te/Ga values, while the opposite is true for the Te/Ge values, where a tendency towards anti-correlation can be recognized (Figure 41I; J). Within the Ge/Ga plot, a positive correlation can also be seen. However, these correlations only apply to the Pasterze (PA) district, as this is the only district where there is more than one value for these plots, even if the values of these elements are limited to < 1 ppm (Figure 41H).

Mesenatten is the only district where chromium is found in pyrite. There is a low correlation between Cr / V (Figure 41K). The chromium reaches values of up to 10 ppm.

A tendency towards positive correlation can be seen between Sb and Tl as well as Sn and In. In the case of Sb/Tl, this is mainly represented by the values of the Hochwurten (HW) and Hirzbach-Schiedalpe (HZ) districts (Figure 41L). The correlation of Sn/In can be seen particularly in the values of the Erzwies (EW) district and partly in the values of Radhausberg (RB) (Figure 41M), which reach up to 160 ppm.

Figure 41N shows a slightly positive correlation of Pb/Bi, but only for the districts Bockhart (BH), Hoher Goldberg (HG) and Siglitz (SZ), all other districts show no correlation.

A tendency towards positive correlation can also be seen for In/Cd and Sn/Mn (Figure 41O; P). However, for In/Cd only values for the districts Goldzeche (GZ), Erzwies (EW) and Bockhart (BH) and for Sn/Mn only values for Radhausberg (RB), Erzwies (EW) and Bockhart (BH) are available. For all other districts, the values are below the detection limit or were evaluated as the result of inclusions and therefore not included.

The plots of Ag/Tl, Au/Bi, Au/Pb, Au/Tl, In/Mn and Ni/Cr all show no tendency towards a correlation (Figure 41Q-V). Especially for the plots In/Mn and Ni/Cr there is not enough data available to make an actual valid statement.

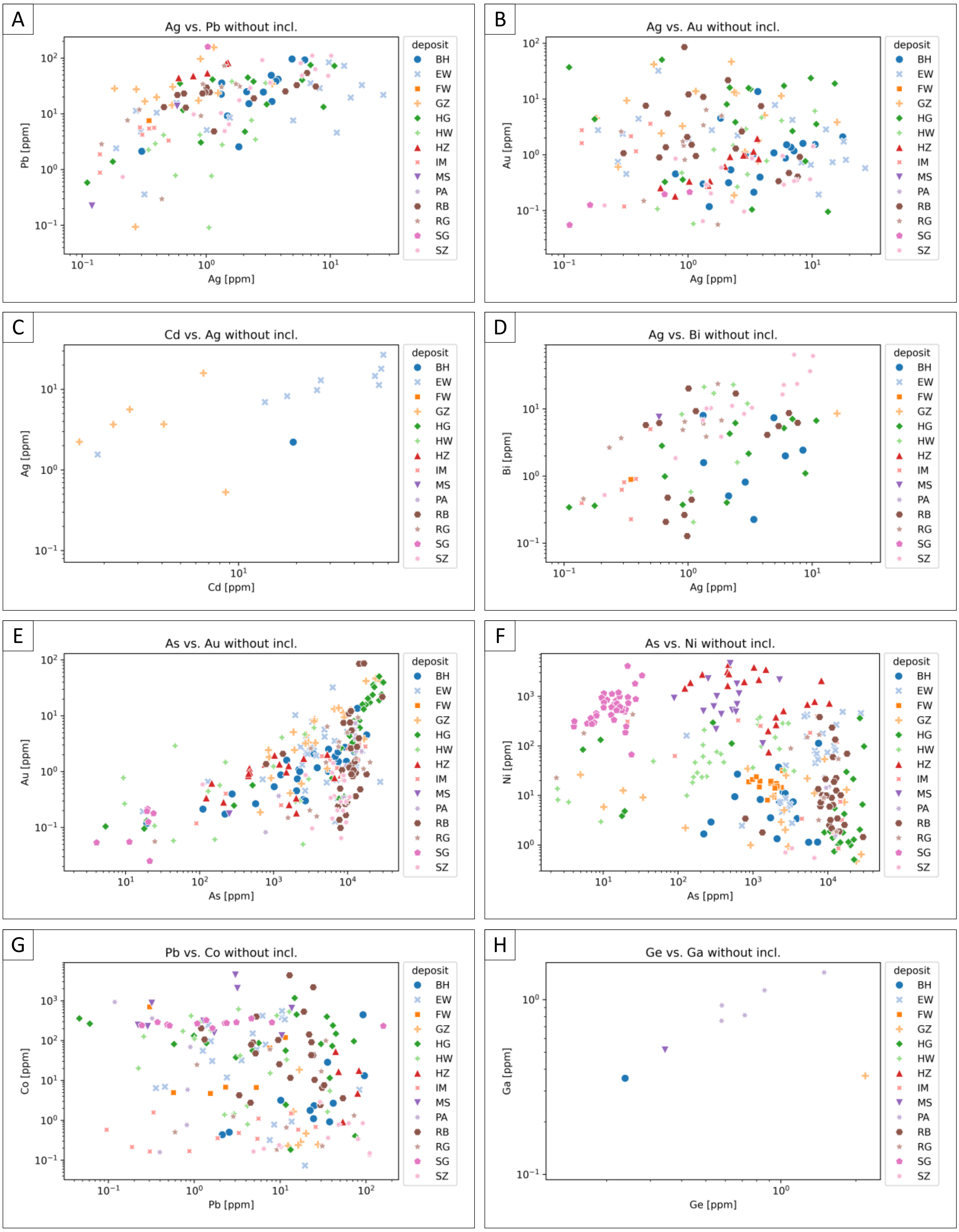
A
Ag vs. Pb without incl.
Pb [ppm]
Ag [ppm]
10^{-1}
10^{0}
10^{1}
10^{2}
deposit
BH
EW
FW
GZ
HG
HW
HZ
IM
MS
PA
RB
RG
SG
SZ
B
Ag vs. Au without incl.
Au [ppm]
Ag [ppm]
C
Cd vs. Ag without incl.
Ag [ppm]
Cd [ppm]
D
Ag vs. Bi without incl.
Bi [ppm]
Ag [ppm]
E
As vs. Au without incl.
Au [ppm]
As [ppm]
10^{3}
10^{4}
F
As vs. Ni without incl.
Ni [ppm]
As [ppm]
G
Pb vs. Co without incl.
Co [ppm]
Pb [ppm]
H
Ge vs. Ga without incl.
Ga [ppm]
Ge [ppm]

I

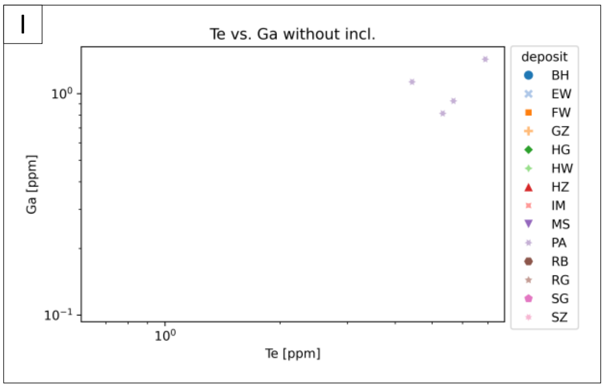
Te vs. Ga without incl.
Ga [ppm]
Te [ppm]
10^0
10^{-1}
10^0
deposit
BH
EW
FW
GZ
HG
HW
HZ
IM
MS
PA
RB
RG
SG
SZ

J

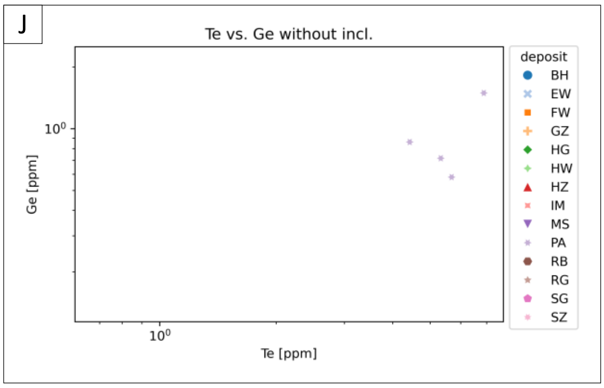
Te vs. Ge without incl.
Ge [ppm]
Te [ppm]
10^0
10^0
deposit
BH
EW
FW
GZ
HG
HW
HZ
IM
MS
PA
RB
RG
SG
SZ

K

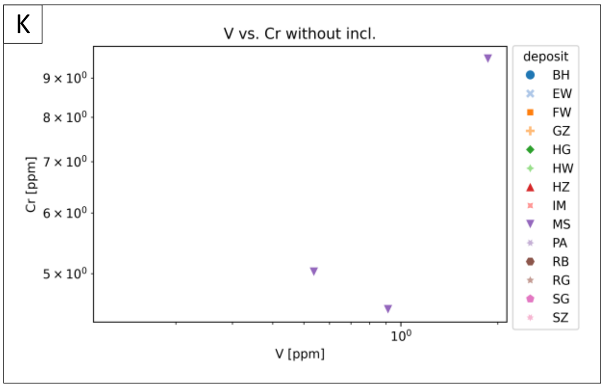
V vs. Cr without incl.
Cr [ppm]
V [ppm]
9×10^0
8×10^0
7×10^0
6×10^0
5×10^0
10^0
deposit
BH
EW
FW
GZ
HG
HW
HZ
IM
MS
PA
RB
RG
SG
SZ

L

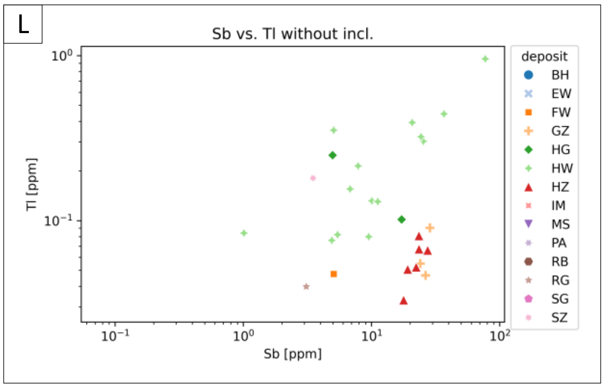
Sb vs. Tl without incl.
Tl [ppm]
Sb [ppm]
10^0
10^{-1}
10^{-1}
10^0
10^1
10^2
deposit
BH
EW
FW
GZ
HG
HW
HZ
IM
MS
PA
RB
RG
SG
SZ

M

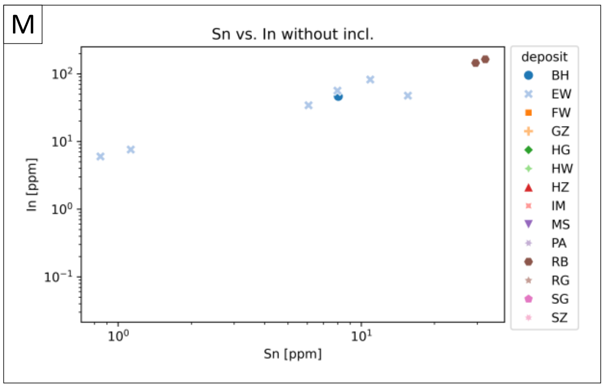
Sn vs. In without incl.
In [ppm]
Sn [ppm]
10^2
10^1
10^0
10^{-1}
10^0
10^1
deposit
BH
EW
FW
GZ
HG
HW
HZ
IM
MS
PA
RB
RG
SG
SZ

N

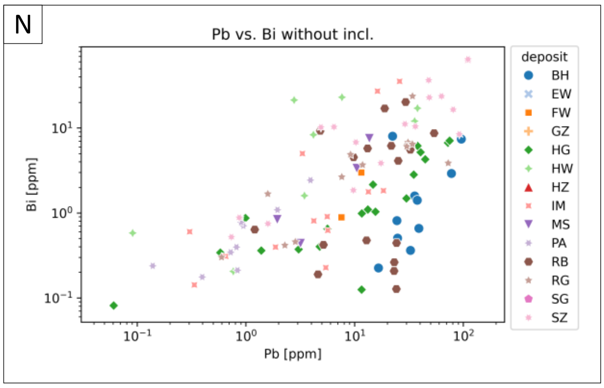
Pb vs. Bi without incl.
Bi [ppm]
Pb [ppm]
10^1
10^0
10^{-1}
10^{-1}
10^0
10^1
10^2
deposit
BH
EW
FW
GZ
HG
HW
HZ
IM
MS
PA
RB
RG
SG
SZ

O

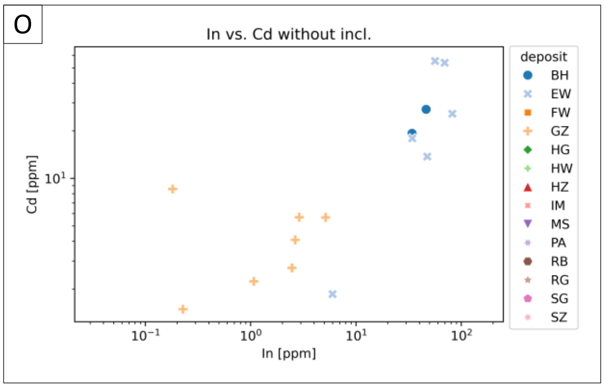
In vs. Cd without incl.
Cd [ppm]
In [ppm]
10^1
10^{-1}
10^0
10^1
10^2
deposit
BH
EW
FW
GZ
HG
HW
HZ
IM
MS
PA
RB
RG
SG
SZ

P

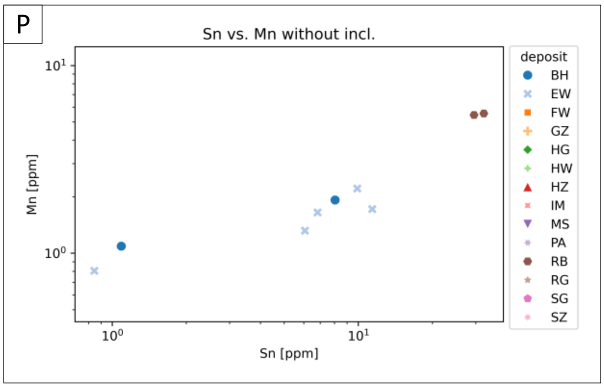
Sn vs. Mn without incl.
Mn [ppm]
Sn [ppm]
10^1
10^0
10^0
10^1
deposit
BH
EW
FW
GZ
HG
HW
HZ
IM
MS
PA
RB
RG
SG
SZ

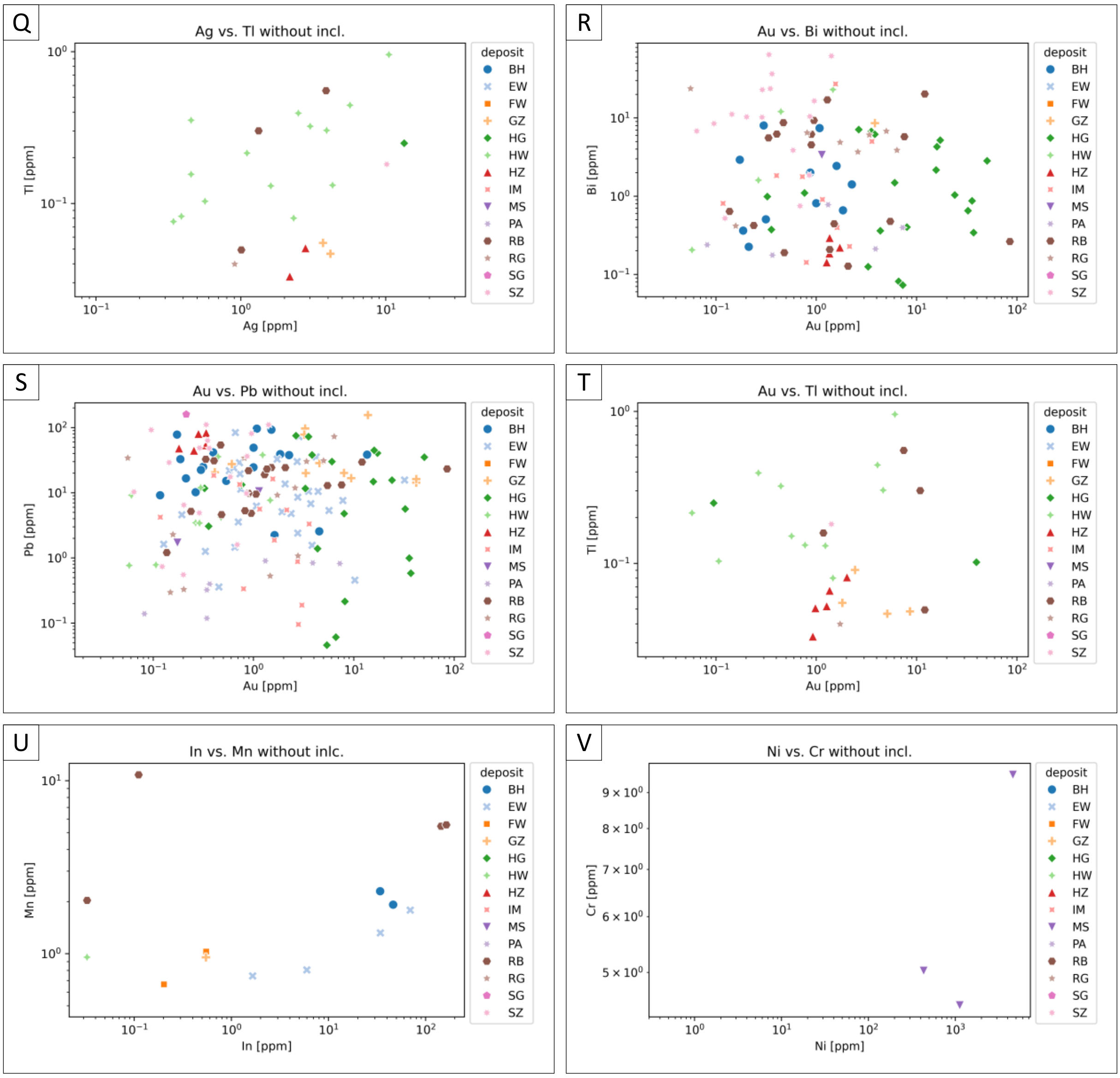

Figure 41: Whole rock geochemistry element correlation. Each graph shows two elements of each district compared to each other. In those graphs are plotted using the data without inclusions A) Ag vs. Pb without incl.; A) Ag vs. Au without incl.; C) Cd vs. Ag without incl.; D) Ag vs. Bi without incl.; E) As vs. Au without incl.; F) As vs. Ni without incl.; G) Pb vs. Co without incl.; H) Ge vs. Ga without incl.; I) Te vs. Ga without incl.; J) Te vs. Ge without incl.; K) V vs. Cr without incl.; L) Sb vs. Tl without incl.; M) Sn vs. In without incl.; N) Pb vs. Bi without incl.; O) In vs. Cd without incl.; P) Sn vs. Mn without incl; Q) Ag vs. Tl without incl.; R) Au vs. Bi without incl.; S) Au vs. Pb without incl.; T) Au vs. Tl without incl.; U) In vs. Mn without incl.; V) Ni vs. Cr without incl..

3.3.1.2 Element Correlations with inclusions

Silver and Pb do show a positive correlation to each other. This can be seen within almost all districts, where the higher the lead content the higher the Ag content is (Figure 42A). Silver reaches values of up to 900 ppm and in around one third of the measuring points silver is below detection limit, whereas Pb reaches values of up to 7 wt% (69371.21 ppm). A positive correlation of Ag and Au can only be seen in the Hirzbach-Schiedalpe (HZ) district (Figure 42B). All the other districts show a wide scattering of points due to a lack of correlation (Figure 42B). The point on the very far right of the Goldzeche district is due to an Au inclusion with a value of around 3 wt%. Silver plotted with Cd, on the other hand, shows a positive correlation only for the Bockhart (BH) district (Figure 42C). The points of the other districts do not show any correlation. The values of the Radhausberg (RB) represent a cluster, meaning the amounts of Cd and Ag do not change much. A tendency to a positive correlation can be seen in the Ag/Bi plot for the Siglitz (SZ), Hoher Goldberg (HG) and Imhof (IM) district (Figure 42D). All other districts do not show any correlation. The values of Hirzbach-Schiedalpe (HZ) form a cluster. The Pb/Bi plot is very similar to Ag/Bi plot. Figure 42E shows a positive correlation of Pb/Bi, for almost all districts with Hirzbach-Schiedalpe (HZ) being the exception, where the points form a cluster with very low Bi values and medium high Pb values.

Rising Au values with rising As values can be seen in Figure 42F. Only five values of Au and three values of As are marked as inclusions, therefor the As/Au plot is almost identical to the one excluding the inclusions.

Figure 42G the As/Ni plot is displayed. The different districts show different patterns like Schellgaden, Fuscher Wegscheide and Mesenatten, which form cluster. Schellgaden is the only district that shows for all measuring points low As and high Ni contents. The districts Hoher Goldberg, Radhausberg show different nickel values with unchanged As values. All other districts show rather a scattering of values without specific correlation. Since only a few values of As and Ni are counted as inclusions, the pattern is almost identical to the plot without inclusions.

The highest value measured for an Au inclusion is 3 wt%. Figure 42H shows an irregular distribution of Pb/Co values with no specific trend for all districts.

Except for one point, a tendency to a positive correlation can be seen for the Te/Ga values, while the opposite is true for the Te/Ge values, where a tendency towards anti-correlation can be recognized (Figure 42I; J). These two plots are the same as without inclusions. If Ge/Ga is plotted, a positive correlation can also be seen here (Figure 42K). However, these correlations only apply to the Pasterze

(PA) district, as this is the only district where there is more than one or two values to make a valid statement, even if the values of these elements are limited to < 1 ppm.

A tendency towards positive correlation can be seen between Sb and Tl as well as Sn and In (Figure 42L; M). In the case of Sb/Tl, this is mainly represented by the values of the Hochwurten (HW) and Hirzbach-Schiedalpe (HZ) districts (Figure 42L). The correlation of Sn/In can be seen particularly in the values of the Erzwies (EW) and Bockhart (BH) districts (Figure 42M). The values of Radhausberg rather form a cluster. All other districts don't show any correlation.

A tendency towards positive correlation and similar appearance can also be seen for In/Cd, Cd/Zn and In/Zn (Figure 42N-P). This is particularly the case for the Erzwies (EW) and Bockhart (BH) districts. The Goldzeche district only shows a distinct correlation for Cd/Zn (Figure 42O). The Radhausberg district is striking, as its values are cluster-formed in all three plots and has the highest values of all (Figure 42N-P). For all other districts, the values are below the detection limit.

None of the Cr/V values are stated as inclusions therefor the plot is the same as the one without inclusions. A low correlation between those two elements is recognizable (Figure 42Q). The chromium reaches values of up to 10 ppm.

The plots of Ag/Tl, Au/Bi, Au/Pb, Au/Tl and In/Mn show all no tendency towards a correlation (Figure 42R-V).

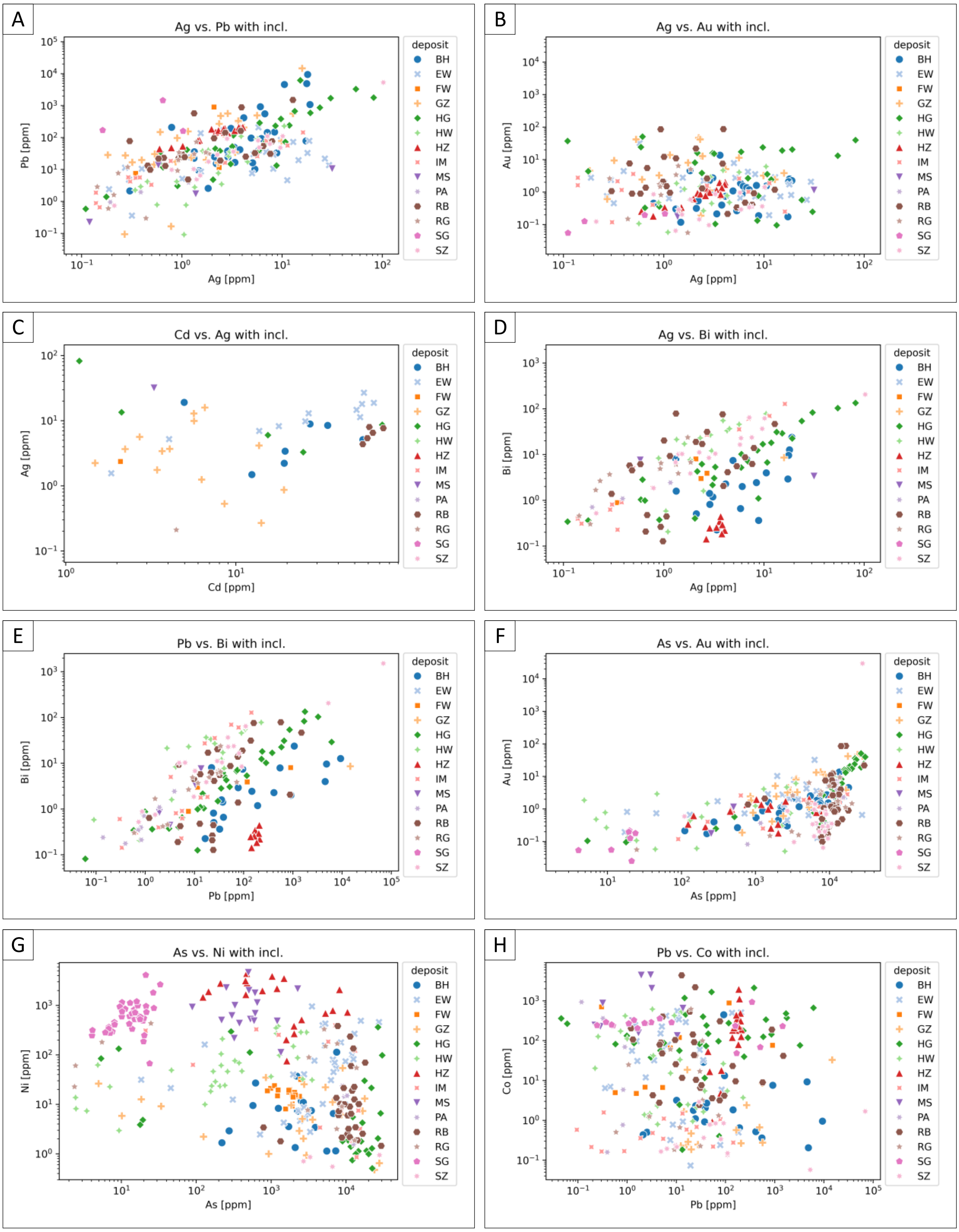
A
Ag vs. Pb with incl.
Pb [ppm]
Ag [ppm]
10⁻¹ 10⁰ 10¹ 10² 10³ 10⁴ 10⁵
B
Ag vs. Au with incl.
Au [ppm]
Ag [ppm]
10⁻¹ 10⁰ 10¹ 10² 10³ 10⁴
C
Cd vs. Ag with incl.
Ag [ppm]
Cd [ppm]
10⁻¹ 10⁰ 10¹ 10²
D
Ag vs. Bi with incl.
Bi [ppm]
Ag [ppm]
10⁻¹ 10⁰ 10¹ 10² 10³
E
Pb vs. Bi with incl.
Bi [ppm]
Pb [ppm]
10⁻¹ 10⁰ 10¹ 10² 10³ 10⁴ 10⁵
F
As vs. Au with incl.
Au [ppm]
As [ppm]
10⁻¹ 10⁰ 10¹ 10² 10³ 10⁴
G
As vs. Ni with incl.
Ni [ppm]
As [ppm]
10⁰ 10¹ 10² 10³ 10⁴
H
Pb vs. Co with incl.
Co [ppm]
Pb [ppm]
10⁻¹ 10⁰ 10¹ 10² 10³ 10⁴ 10⁵
deposit
BH
EW
FW
GZ
HG
HW
HZ
IM
MS
PA
RB
RG
SG
SZ

I

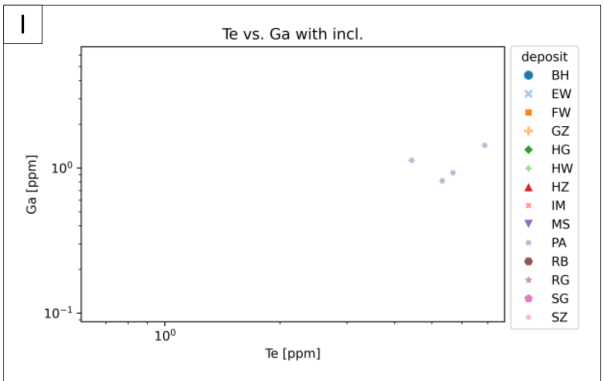
Te vs. Ga with incl.
Ga [ppm]
10^0
10^{-1}
10^0
Te [ppm]
deposit
BH
EW
FW
GZ
HG
HW
HZ
IM
MS
PA
RB
RG
SG
SZ

J

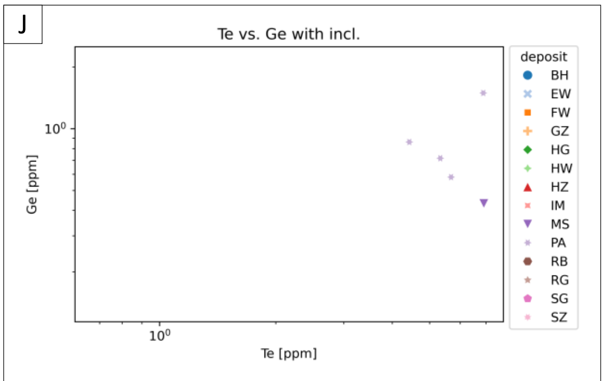
Te vs. Ge with incl.
Ge [ppm]
10^0
10^0
Te [ppm]
deposit
BH
EW
FW
GZ
HG
HW
HZ
IM
MS
PA
RB
RG
SG
SZ

K

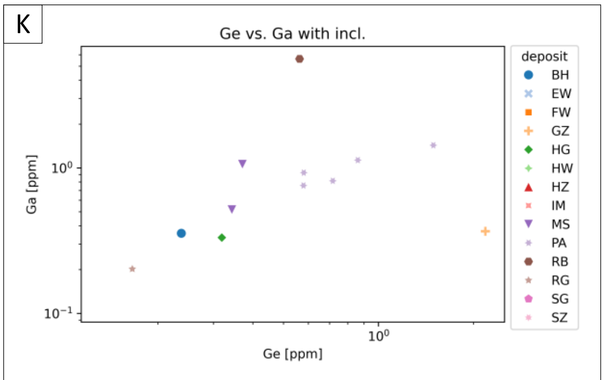
Ge vs. Ga with incl.
Ga [ppm]
10^0
10^{-1}
10^0
Ge [ppm]
deposit
BH
EW
FW
GZ
HG
HW
HZ
IM
MS
PA
RB
RG
SG
SZ

L

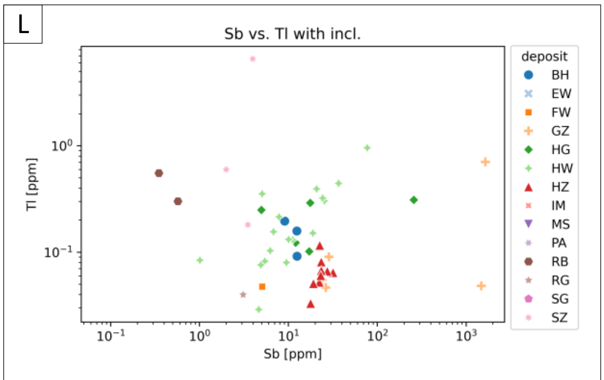
Sb vs. Tl with incl.
Tl [ppm]
10^0
10^{-1}
10^{-1}
10^0
10^1
10^2
10^3
Sb [ppm]
deposit
BH
EW
FW
GZ
HG
HW
HZ
IM
MS
PA
RB
RG
SG
SZ

M

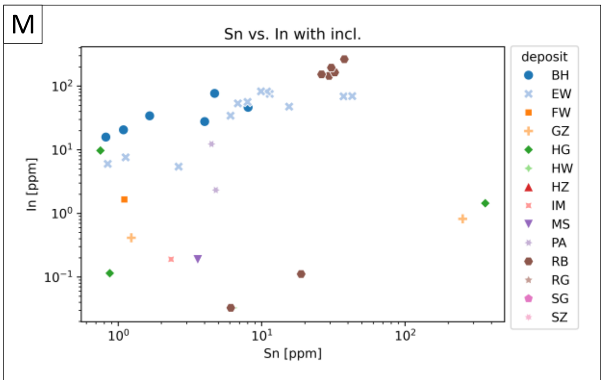
Sn vs. In with incl.
In [ppm]
10^2
10^1
10^0
10^{-1}
10^0
10^1
10^2
Sn [ppm]
deposit
BH
EW
FW
GZ
HG
HW
HZ
IM
MS
PA
RB
RG
SG
SZ

N

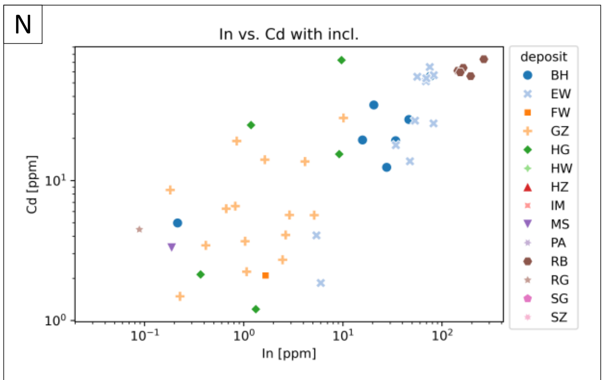
In vs. Cd with incl.
Cd [ppm]
10^1
10^0
10^{-1}
10^0
10^1
10^2
In [ppm]
deposit
BH
EW
FW
GZ
HG
HW
HZ
IM
MS
PA
RB
RG
SG
SZ

O

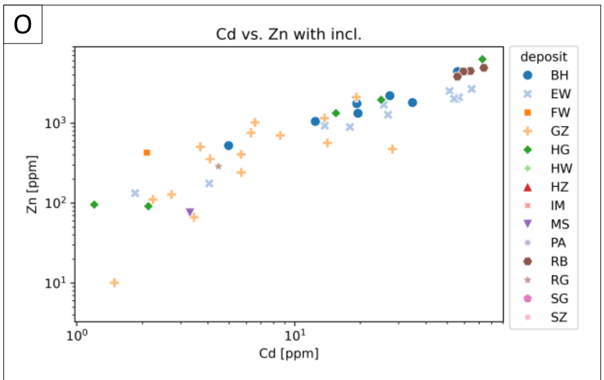
Cd vs. Zn with incl.
Zn [ppm]
10^3
10^2
10^1
10^0
10^1
Cd [ppm]
deposit
BH
EW
FW
GZ
HG
HW
HZ
IM
MS
PA
RB
RG
SG
SZ

P

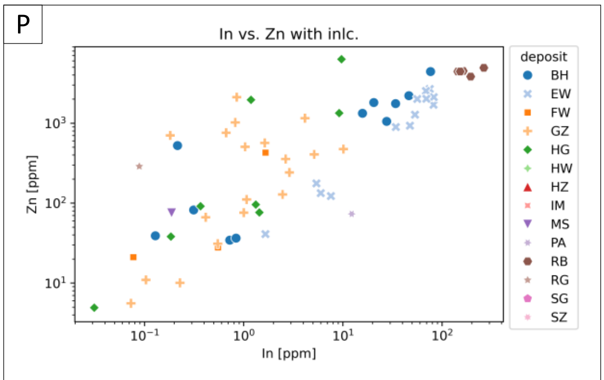
In vs. Zn with inlc.
Zn [ppm]
10^3
10^2
10^1
10^{-1}
10^0
10^1
10^2
In [ppm]
deposit
BH
EW
FW
GZ
HG
HW
HZ
IM
MS
PA
RB
RG
SG
SZ

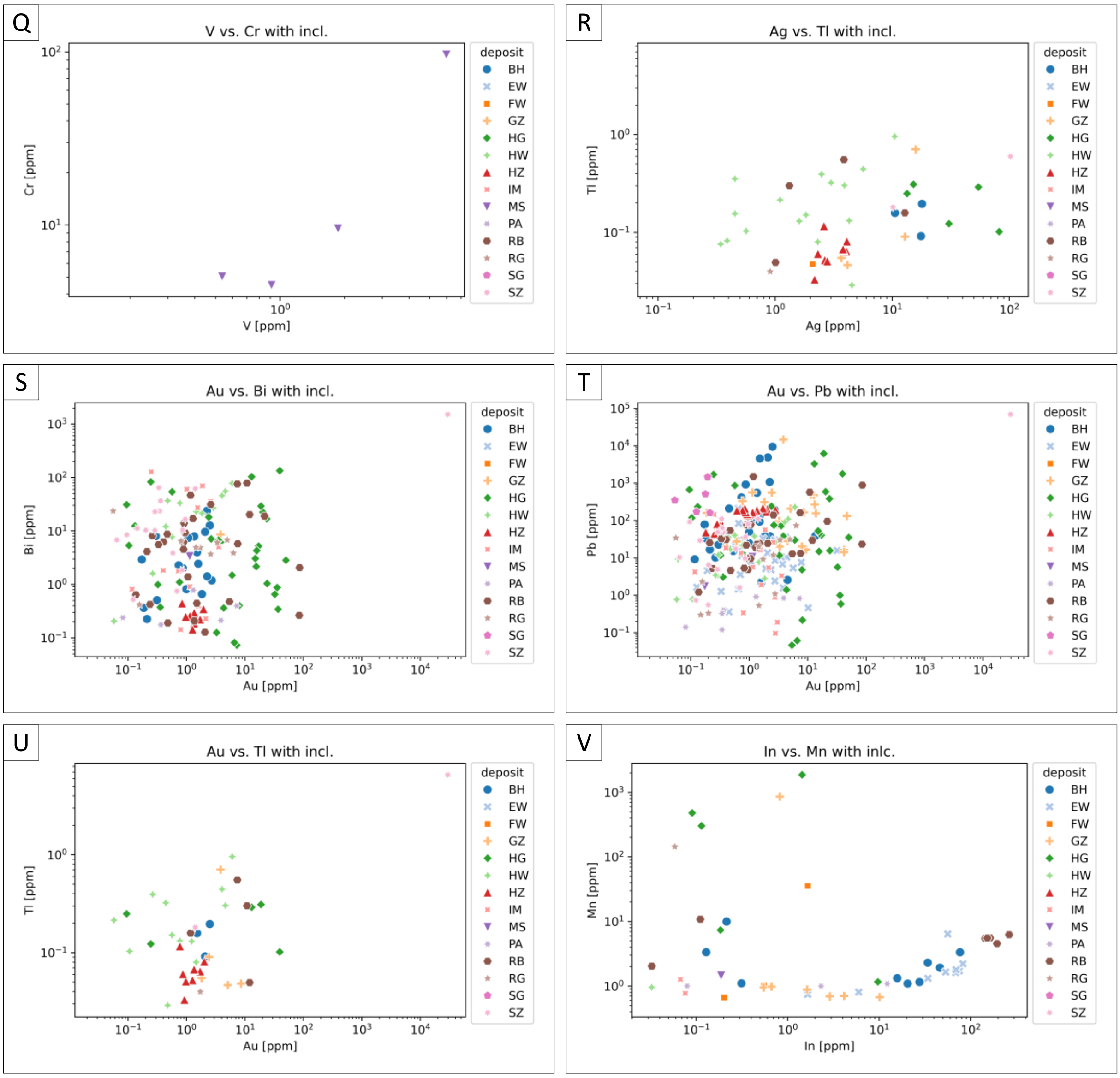

Figure 42: Whole rock geochemistry element correlation. Each graph shows two elements of each district compared to each other. In those graphs are plotted using the data with inclusions A) Ag vs. Pb with incl.; A) Ag vs. Au with incl.; C) Cd vs. Ag with incl.; D) Ag vs. Bi with incl.; E) Pb vs. Bi with incl.; F) As vs. Au with incl.; G) As vs. Ni with incl.; H) Pb vs. Co with incl.; I) Te vs. Ga with incl.; J) Te vs. Ge with incl.; K) Ge vs. Ga with incl.; L) Sb vs. Tl with incl.; M) Sn vs. In with incl.; N) In vs. Cd with incl.; O) Cd vs. Zn with incl.; P) In vs. Zn with incl; Q) V vs. Cr with incl.; R) Ag vs. Tl with incl.; S) Au vs. Bi with incl.; T) Au vs. Pb with incl.; U) Au vs. Tl with incl.; V) In vs. Mn with incl..

3.3.1.3 *Element changes within zonation*

In order to obtain a better visual comparison of the elements measured with the LA-ICP-MS depending on the points set in different areas of the zoning, the graphics below were created and described. The measured points (shown as red circles) are marked and numbered in the BSE image. These points already correspond to the true size of the measuring points. In the enclosed graphs, the contents of Co, Ni, As and Au are plotted in relation to the numbers. These plotted values represent the exact values measured within the marked point on the BSE image.

Sample A1370 (Hoher Goldberg)

Most of the pyrites within this sample show strong, partly oscillating zonations, especially the smaller idiomorphic crystals. Figure 43A shows several idiomorphic pyrite crystals with distinct zonation. The zonation of these crystals can be divided into 3 main zones. The dark core has rounded, as well as straight edges. Along the edge of this zone, very small (< 5 µm), very bright inclusions can be seen which mainly are inclusions of galena and chalcopyrite. This core is surrounded by a lighter greyscale zone which oscillates with a middle bright phase in the case of the crystal on the right. The rim of the pyrite is characterized by a medium dark zone. This zone is lighter than the core but darker than the brighter middle zone. Four LA-ICP-MS points were placed and measured within these two pyrite crystals. The first within the dark core, the second and third within the light intermediate area and the fourth at the edge of the left pyrite.

It can be clearly seen in the graphs that the gold and arsenic contents within the dark core are very low, or below detection limit (Figure 43C; D). In addition, both graphs show a similar pattern regarding the contents. Within the light areas the gold and arsenic contents are increased, but are slightly decreased within the edge area, but not as low as in the core. The nickel and cobalt contents show similar trends to each other, but a different pattern compared to the gold and arsenic. The nickel and cobalt concentrations are slightly elevated within the core and the light zones (Figure 43B). However, the grades are very low to below detection limit at the rim within the medium dark zone.

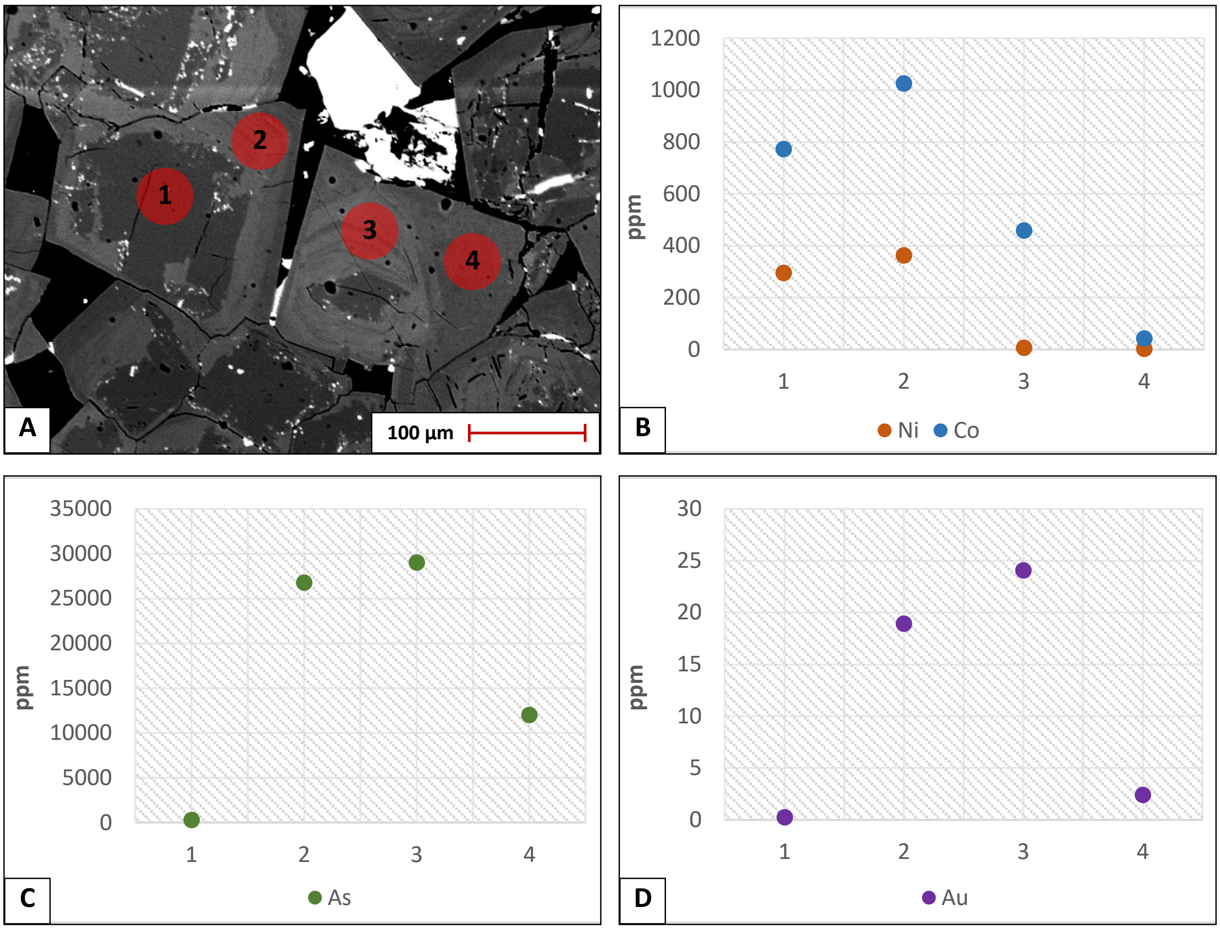

Figure 43: Comparison of the measured values of Au, As, Ni, and Co with the zonation of the measured Pyrite. Each number represents the value of the measured point within the shown Pyrite. A: BSE image of two Pyrites of the Sample A1370 (Hoher Goldberg) showing severe zonation. B: graph showing the Ni (orange) and Copper (blue) values of the measured points as shown in A. C: graph showing the As (green) values of the measured points as shown in A. D: graph showing the Au (purple) values of the measured points as shown in A.

Sample PM-RB-07 (Radhausberg)

Most of the pyrites within this sample show clearly visible zonations, especially the smaller idiomorphic crystals. The larger xenomorphic pyrite crystals show an irregular zonation while the idiomorphs show a crystal boundary parallel zonation. Figure 44A shows three idiomorphic pyrite crystals with straight crystal boundaries and a distinct zonation. The core of those pyrites appears dark, whereas the rim is brighter. The boundary between the light and darker zones is subparallel to the crystal boundary. In addition, within the dark core of the large central pyrite near the zonation boundary, very fine light zones can be recognized which also run parallel to the crystal boundary. Only a few inclusions of light-appearing arsenopyrite can be recognized, which do not follow any particular pattern. Within the light areas, however, more dark appearing inclusions or holes can be recognized. Four LA-ICP-MS points were placed and measured within two pyrite crystals. The first and fourth a located within the dark core, whereas the second and third are located within the bright rim of the pyrites.

The graphs in this sample also show that the gold and arsenic contents are higher in the light areas than in the dark areas (Figure 44C; D). This is particularly clear in the graph with the gold contents, as the contents here are close to zero or below detection limit in the dark areas. The cobalt and nickel contents are very similar and correlate with each other (Figure 44B). However, a specific dependence of the contents on the zonations cannot be recognized. While the contents of the first measuring point (dark area) are elevated, the contents of the fourth measuring point (also dark area of another pyrite) are very low. The Ni and Co contents of the two measuring points within the light areas are relatively equal (Figure 44B). These are lower than at measuring point 1 but higher than at measuring point 4.

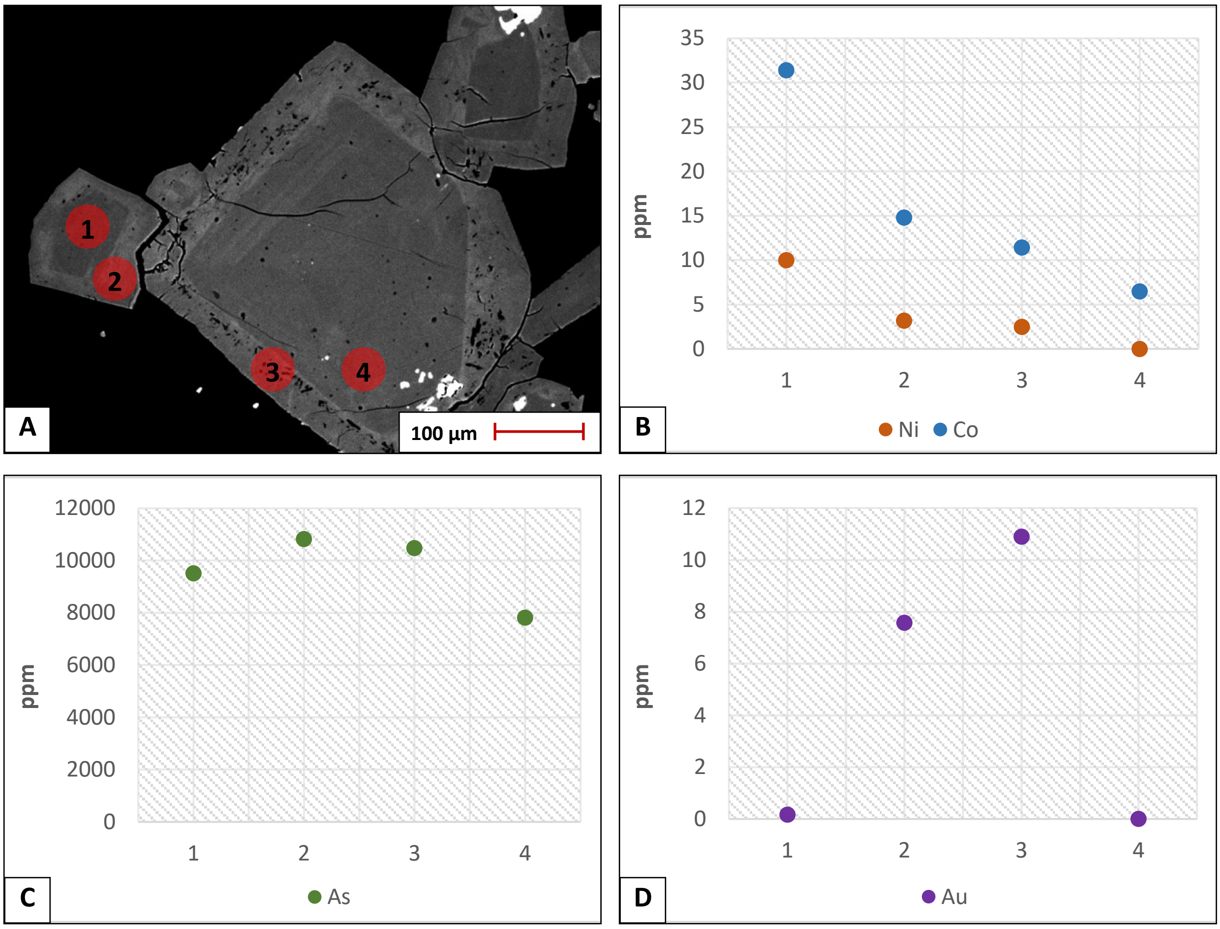

Figure 44: Comparison of the measured values of Au, As, Ni, and Co with the zonation of the measured Pyrite. Each number represents the value of the measured point within the shown Pyrite. A: BSE image of two Pyrites of the Sample PM-RB-07 (Radhausberg) showing intensive zonation. B: graph showing the Ni (orange) and Copper (blue) values of the measured points as shown in A. C: graph showing the As (green) values of the measured points as shown in A. D: graph showing the Au (purple) values of the measured points as shown in A.

Sample PM-PA-02 (Pasterze)

Most of the pyrites within this sample show strong, mostly irregular zonations, which are usually composed of a dark core and a bright rim and rounded irregular zone boundaries. Figure 45A shows xenomorphic pyrite crystal with distinct zonation. The zonation of this crystal can be divided into a dark core which has rounded as well as bay-shaped edges which is surrounded by a bright rim. Around the dark core within the bright area, streak-like irregular zonations can be seen which are slightly brighter than the rim. Only a few chalcopyrite and pyrrhotite inclusions can be seen. Five LA-ICP-MS points were placed and measured within this pyrite crystal with three being placed within the bright zonation and two placed in the dark core.

In this case the graphs representing the gold and arsenic contents show a similar pattern regarding the contents. Within the dark core the contents are very low, or below detection limit. Within the light areas the gold and arsenic contents are increased (Figure 45C; D). The first LA-ICP-MS point shows a lower gold content compared to points number two and three, whereas the arsenic content is in point one to three. The nickel and cobalt contents are very different from each other (Figure 45B). In this pyrite there is no nickel above the detection limits. The cobalt does show a similar pattern to the arsenic with higher contents in the bright rim and lower to zero/below detection limit in the dark core (Figure 45B). This contrasts with the pyrite in Figure 44 and Figure 43, where the As and Co showed no correlation.

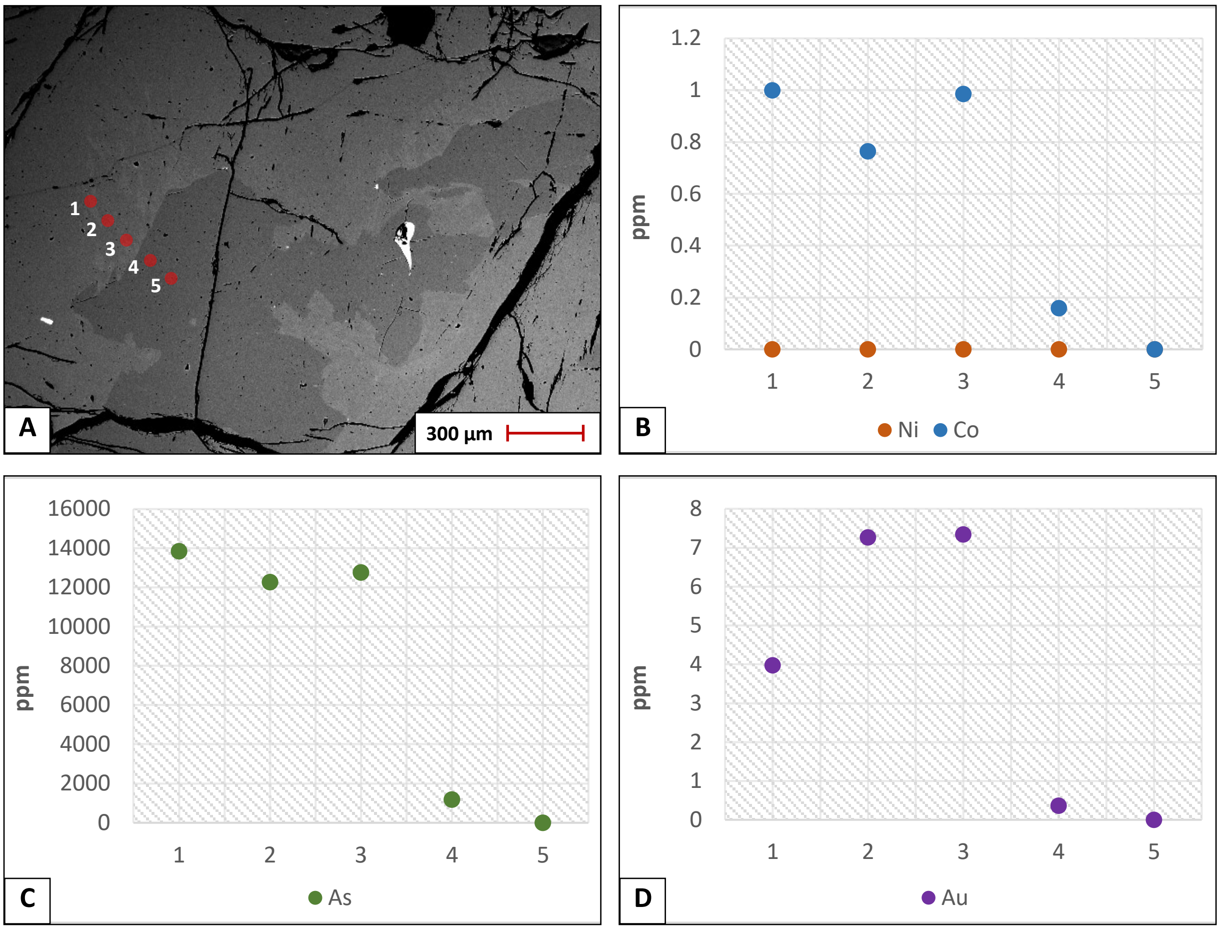

Figure 45: Comparison of the measured values of Au, As, Ni, and Co with the zonation of the measured Pyrite. Each number represents the value of the measured point within the shown Pyrite. ***A:*** *BSE image of two Pyrites of the Sample PM-PA-02 (Pasterze) showing severe zonation.* ***B:*** *graph showing the Ni (orange) and Copper (blue) values of the measured points as shown in A.* ***C:*** *graph showing the As (green) values of the measured points as shown in A.* ***D:*** *graph showing the Au (purple) values of the measured points as shown in A.*

3.3.1.4 Trace element distribution

For a better visual representation, the average values measured in pyrite crystals are displayed on a geological map with color gradation depending on the values. The elements chosen are the same plotted in 3.3.2 Laser Ablation of electrum for a better comparison and further discussion. The element Pd hasn't been measured in pyrite so instead the element As is plotted.

As can be seen in Figure 46A, the highest Cu values were measured in the pyrite districts Hierzbach-Schiedalpe (HZ), Bockhart (BH), Radhausberg (RB) and Rotgülden (RG), while in the districts Fuscher Wegscheide (FW), Mesenatten (MS) Hochwurten (HW), Bockhart (BH) and Schellgaden (SG) only very low to no values (below detection limit) were measured. Schellgaden (SG) has the lowest As value compared to all other districts with an average of only 15 ppm (Figure 46B). Such deficits for Schellgaden (SG) can also be seen for the elements Au, Ag, Sb, Pb and Bi (Figure 46C-E,G-H). Elevated values were only measured for Hg (Figure 46F). The Fuscher Wegscheide (FW) and Mesenatten (MS) districts also show low to occasional moderate values for most elements (Pb, Bi, Sb, Au, Ag, Cu, As). The exception is Mesenatten (MS), which shows elevated values for Hg. Rotgülden (RG), on the other hand, only shows low values for the elements Sb and Hg (Figure 46E-F). The situation is similar in the Hirzbach-Schiedalpe (HZ) district, which only has low values for the elements Hg and Bi (Figure 46F,H). Figure 46D shows that the highest Au values are found in the Goldzeche (GZ), Hoher Goldberg (HG), Radhausberg (RB) and Erziwes (EZ) districts, while the Fuscher Wegscheide (FW), Mesenatten (MS), Hochwurten (HW), Bockhart (BH) and Schellgaden (SG) districts have only very low values or no values (below detection limit). For Ag Figure 46C shows a similar distribution. In general, a trend can be seen in which most of the districts with high values for the elements shown are located in the central region of the study area (Gastein-Rausris). Figure 46 is an exception for the element Hg, which does not reflect this distribution trend.

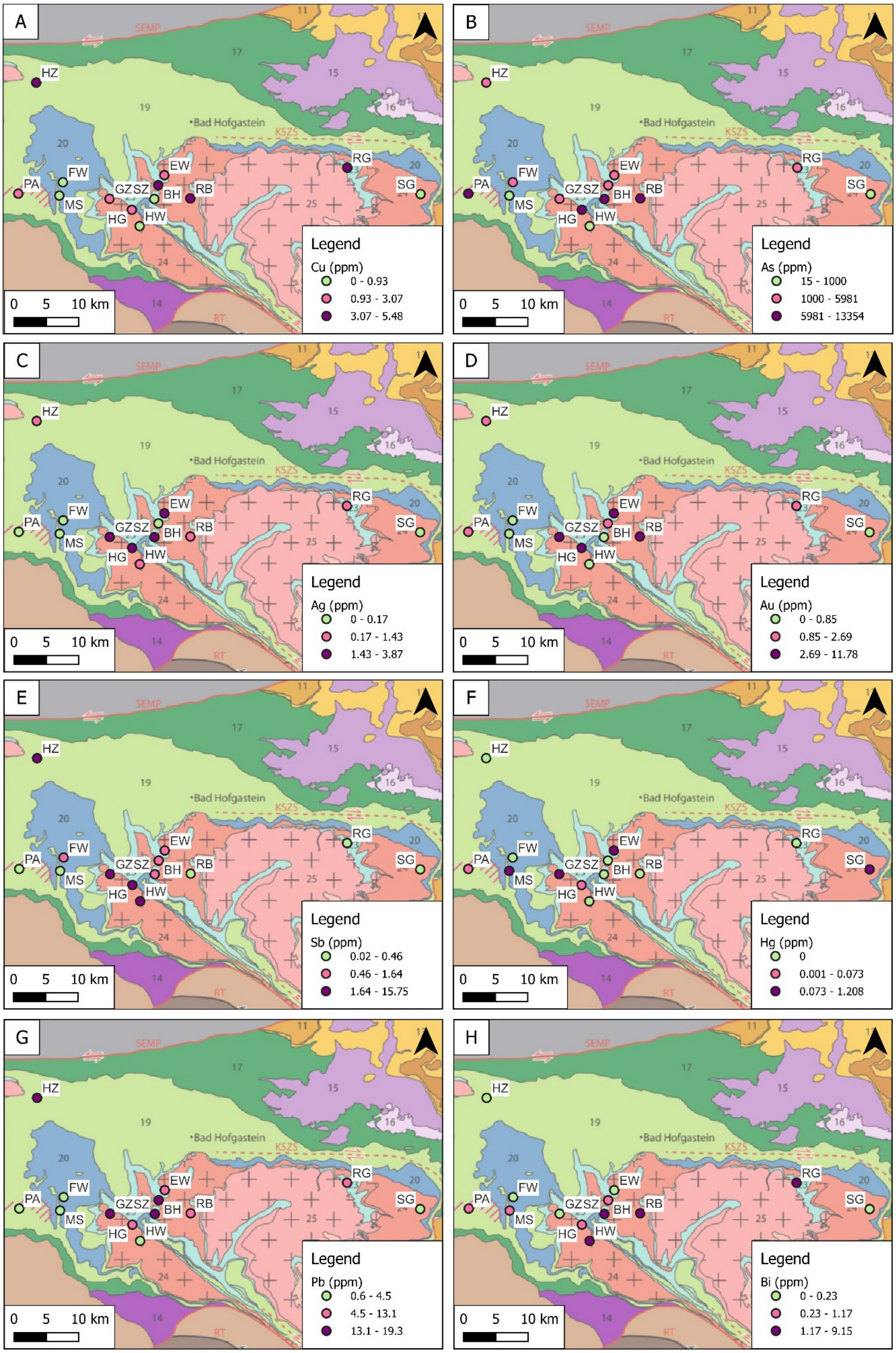
A
B
C
D
E
F
G
H
SEMP
KSZS
RT
Bad Hofgastein
11
14
15
16
17
19
20
24
25
HZ
PA
FW
MS
GZ
SZ
EW
BH
RB
HG
HW
RG
SG
0 5 10 km
Legend
Cu (ppm)
0 - 0.93
0.93 - 3.07
3.07 - 5.48
Legend
As (ppm)
15 - 1000
1000 - 5981
5981 - 13354
Legend
Ag (ppm)
0 - 0.17
0.17 - 1.43
1.43 - 3.87
Legend
Au (ppm)
0 - 0.85
0.85 - 2.69
2.69 - 11.78
Legend
Sb (ppm)
0.02 - 0.46
0.46 - 1.64
1.64 - 15.75
Legend
Hg (ppm)
0
0.001 - 0.073
0.073 - 1.208
Legend
Pb (ppm)
0.6 - 4.5
4.5 - 13.1
13.1 - 19.3
Legend
Bi (ppm)
0 - 0.23
0.23 - 1.17
1.17 - 9.15

Figure 46: Showing the average values of some elements measured in the pyrite crystals, displayed on a geological map with color gradation depending on the values in parts per million (ppm). Each map representing a different element. A) Average values for Cu; B) Average values for As; C) Average values for Ag; D) Average values for Au; E) Average values for Sb); F) Average values for Hg; G) Average values for Pb; H) Average values for Bi. The districts are named after their abbreviations: HZ = Hierzbach-Schiedalpe, PA = Pasterze, FW = Fuscher Wegscheide, MS = Mesenatten, GZ = Goldzeche, HG = Hoher Goldberg, HW = Hochwurten, SZ = Siglitz, BH = Bockhart, EW = Erzwies, RB = Radhausberg, RG = Rotgülden, SG = Schellgaden.

3.3.2 LASER ABLATION OF ELECTRUM

For a better visual representation, the average values of the relevant elements measured in the electrum crystals are displayed on a geological map with color gradation depending on the values.

As can be seen in (Figure 47A), the electrum crystals of the Schellgaden district contain the largest amount of Cu with more than 200 cps while the others only reach less than 41.4 cps. The Schellgaden district also stands out in terms of palladium content, as it is the only district to contain Pd in the gold crystals (Figure 47B). Figure 47C; D show the Au and Ag content of the crystals. The high content of Au but low content of Ag in the Schellgaden district is conspicuous, whereas the crystals of the Rotgülden district have a moderately high content of Ag but a low content of Au. The Au and Ag contents in the Hoher Goldberg district are comparatively low. The Schellgaden district has a comparatively high Ag content as well as a moderately high Au content. In terms of Sb content, the Rotgülden district stands out in particular with values of up to 485 cps (Figure 47E). Siglitz and Schellgaden contain no Sb, while the Hohe Goldberg district has a rather low content of up to 50 cps compared to Rotgülden.

The Hoher Goldberg district also exhibits the highest values for the elements Hg, Pb and Bi. Values of 324 cps are achieved for Hg, 34 cps for Pb and 55 cps for Bi (Figure 47F-H). The Rotgülden district, on the other hand, shows the lowest values for these three elements. Schellgaden has moderately high Hg values (up to 203 cps) and only low Pb and Bi values. The Siglitz district has low Hg values, but in turn has moderately high values for the elements Pb (up to 20 cps) and Bi (up to 44 cps)(Figure 47F-H).

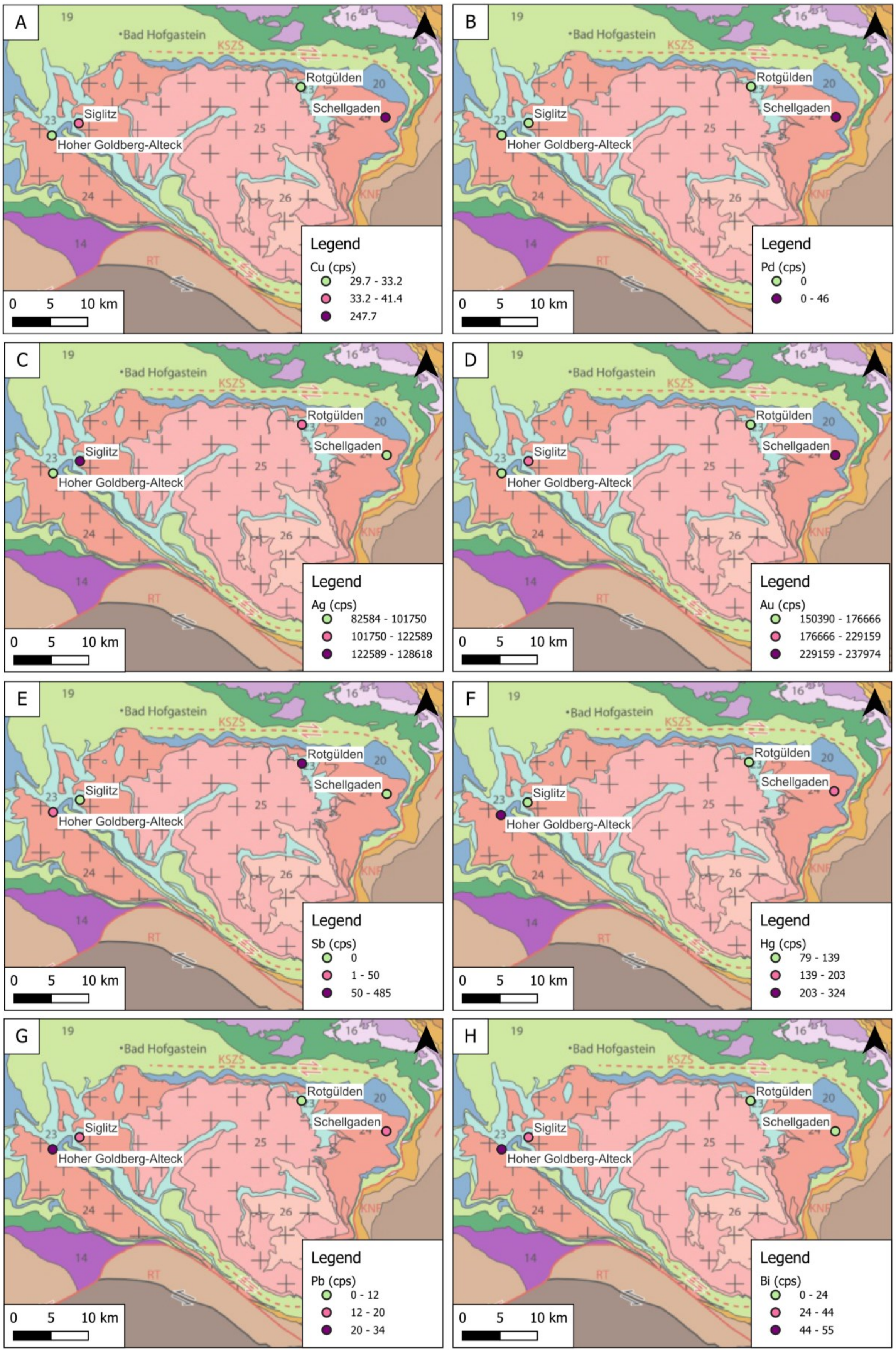
A
B
C
D
E
F
G
H
19
16
•Bad Hofgastein
KSZS
Rotgülden
20
Schellgaden
Siglitz
23
Hoher Goldberg-Alteck
25
24
26
KNF
14
RT
0 5 10 km
Legend
Cu (cps)
29.7 - 33.2
33.2 - 41.4
247.7
Pd (cps)
0
0 - 46
Ag (cps)
82584 - 101750
101750 - 122589
122589 - 128618
Au (cps)
150390 - 176666
176666 - 229159
229159 - 237974
Sb (cps)
0
1 - 50
50 - 485
Hg (cps)
79 - 139
139 - 203
203 - 324
Pb (cps)
0 - 12
12 - 20
20 - 34
Bi (cps)
0 - 24
24 - 44
44 - 55

Figure 47: Showing the average values of the relevant elements measured in the electrum crystals, displayed on a geological map with color gradation depending on the values in counts per second (cps). Each map representing a different element. A) Average values for Cu; B) Average values for Pd; C) Average values for Ag; D) Average values for Au; E) Average values for Sb); F) Average values for Hg; G) Average values for Pb; H) Average values for Bi.

3.4 ELECTRON PROBE MICROANALYSIS (EPMA)

In total, three EPMA maps of representative samples were conducted to see in greater detail the differences in trace elements within pyrites. In the case of multiple maps of the same sample the maps are individually labeled. The maps show either parts of pyrite or the whole crystal. The EPMA maps provide only qualitative and not quantitative results, therefor brighter colors (orange/white in this case) indicate higher element contents while darker shades (green/black in this case) indicate a lower element content. For all maps the elements As (WDS; L - α), Ag (WDS; L - α), Au (WDS; L - α), Co (WDS; K - α), Ni (WDS; K - α), Pb (EDS; L - α), Sb (EDS; L - β), Cu (EDS; K - α), Fe (EDS; K - α), S (EDS; K - α) and are shown.

All mapping locations were selected based on zonations recognizable in the BSE image. The size of the image section was adapted to each crystal. The pixel size, dwell time and probe current were also adjusted according to the elements to be mapped and the type of zonation. The dwell time was between 150 ms and 500 ms and the probe current between 100 nA and 230 nA. As can be seen in Figure 48 below, a higher dwell time and higher probe current leads to better signal to noise, which allows for the detection of smaller amounts of an element within the pyrite.

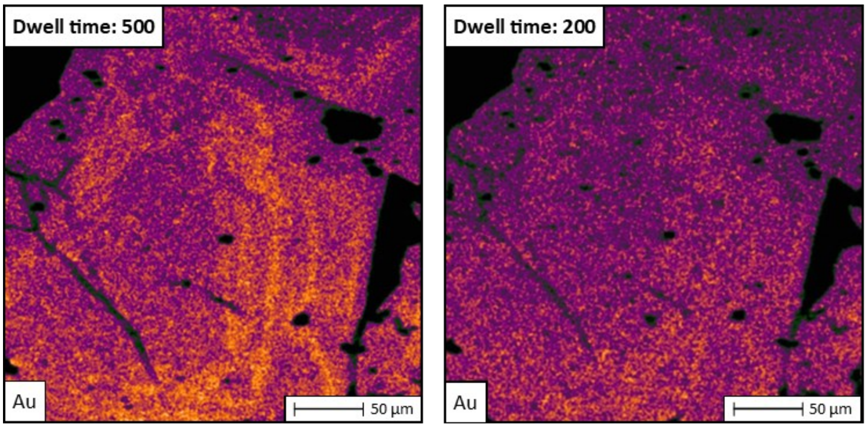

Figure 48: Sample PM-RG-03 (Rotgülden), EMPA gold map with 500 ms dwell time with 145 nA probe current (left) and 200 ms dwell time with 223 nA probe current (right).

3.4.1 EPMA ELEMENT MAP A1370 (HOHER GOLDBERG)

As can be seen in the BSE image (Figure 49a), these are idiomorphic crystals which have a straight and sharp boundary to each other. A clear zonation of the pyrite crystals can be seen within the BSE image. A dark core surrounded by a light rim can be observed. This bright edge has a thickness of 20 – 50 µm. The brightness also varies within this rim. The brightness decreases slightly towards the core. At the lower end (bottom left) of the elongated pyrite crystal, small and dark square areas up to 15 µm in size can also be observed within the bright rim. At the left rim of the elongated pyrite crystal, the bright rim appears slightly diagonally striped. At the very bottom, a triangular zonation can be recognized within a small pyrite where the core is bright, and the zonation becomes darker towards the outside. The surrounding pyrite crystals shows similar characteristics. Especially within the right pyrite crystal, several very bright and small inclusions can be recognized, which are preferably located along the bright zonations.

The zonation of As (Figure 49b) in the pyrite crystals is particularly pronounced. These high As contents, characterized by orange/white color, are congruent with the bright edges of the pyrites in the BSE image. The rather striped zoning on the left edge can be seen even more clearly in the As map. In the core of the pyrites, the As content is relatively low. The square areas that appear darker in the BSE also show very low As contents. Gold, Pb, Sb and Cu (Figure 49d; g-i) show similar zonation patterns. Lead shows the highest content of the four elements, followed by Au, Cu and Sb. The maps of Au, Pb, Sb and Cu mirror the features seen in both the BSE image and the As map. Within the Au map, the bright inclusions visible in the BSE also show a very high Au content. Inclusions with higher contents are also increasingly recognizable in the Sb and Cu maps. Only in the Pb map shows hardly any inclusions. Silver (Figure 49c) shows hardly any zonation. On the right side a slight zonation is visible which follows the inclusions. The inclusions visible in the Ag map are congruent with the inclusions of the Au map. Sulfur (Figure 49j) exhibits a zonation pattern contrary to that of As, Au, Pb, Sb and Cu. The S map shows clearly the higher the content of As, Au, Pb, Sb and Cu the lower the S content. A zonation of iron (Figure 49k) within the pyrite is not visible. The Ni and Co maps (Figure 49e; f), on the other hand, show completely different zonation patterns. Cobalt shows increased values partly congruent with As but in a different rather irregular pattern. The Co content is particularly high at the top left at the edge of the pyrite crystal and at the bottom left near the edge of the pyrite crystal. The triangular zonations of the two pyrites at the bottom left also have a high Ni content. The triangular light-colored core has a high Ni content while the edge has a low Ni content. In addition, streaky, slightly brightened zoning is also visible towards the core of the elongated pyrite. The Ni zoning does not correlate to the other mapped elements. It is subparallel to the crystal boundaries but is more concentrated in the cores of the pyrite crystals. Along the Ni rich zonation, spotty areas are also recognizable which appear particularly bright and thus represent a high Ni content. The zonation in general is particularly prominent just before the strong Co zoning appears.

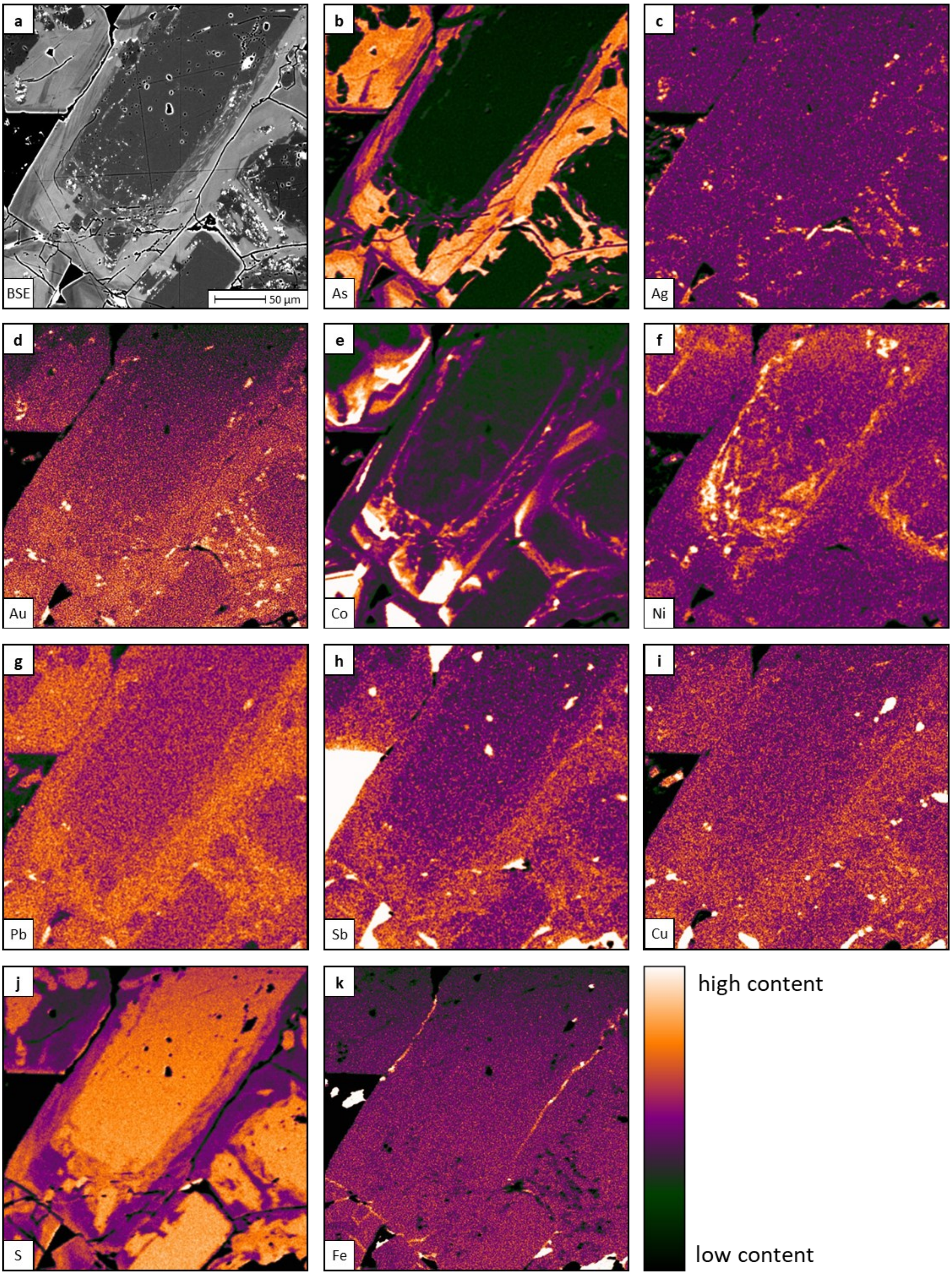

Figure 49: Pyrite element maps in sample A1370; a) BSE image; b) As EDS spectrometer; c) Ag WDS spectrometer; d) Au WDS spectrometer; e) Co EDS spectrometer; f) Ni EDS spectrometer; g) Pb EDS spectrometer; h) Sb WDS spectrometer; i) Cu EDS spectrometer; j) S EDS spectrometer; k) Fe WDS spectrometer.

3.4.2 EPMA ELEMENT MAP A1463 (GOLDZECHE)

The map of specimen A1463 (Goldzeche) shows a section (lower corner) of a 950 µm large idiomorphic pyrite crystal. In the BSE image (Figure 50a) a clear concentric zonation parallel to the crystal rim can be recognized. Several alternating light and dark zoning stripes are visible. These also have different thicknesses of less than 5 µm to 25 µm. Furthermore, interruptions of the zonation can be seen in the upper center as well as in the far-left center of the image. These interruptions show no zonation and appear dark. Towards the core of the pyrite crystal, no more zonations can be recognized and it appears dark. Some bright and small inclusions (smaller than 5 µm) distributed within the pyrite are identifiable.

Arsenic (Figure 50b) shows a particularly pronounced zonation within the pyrite crystal. These high As contents, characterized by orange/white color, are congruent with the bright zonation stripes of the pyrites in the BSE image. Therefore, just like in the BSE image, the As zonation appears as a clear concentric zonation parallel to the crystal rim with some interruptions in the upper center as well as in the far-left center of the image. Gold, Pb and Sb (Figure 50d; g-h) show similar zonation patterns. Gold shows the highest content of the three elements, followed by Sb and Pb. The maps of Au, Pb and Sb mirror the features seen in both the BSE image and the As map. Within the Au map, the bright inclusions visible in the BSE also show a very high Au content. These inclusions are preferably visible within or on the edge of the zonations with higher Au content. No inclusions with higher contents are recognizable in the Sb and Pb maps. Sulfur (Figure 50j) exhibits a zonation pattern contrary to that of As, Au, Pb and Sb. The S map shows clearly the higher the content of As, Au, Pb and Sb the lower the sulfur content. The Cu map (Figure 50i) exhibits only a fade zonation with lots of copper rich inclusion distributed over the whole pyrite crystal. The Co map (Figure 50e) barely shows any zonation but appears brighter at the bottom edge than on the top edge of the map. The nickel map (Figure 50f), on the other hand, shows a completely different zonation pattern. The zonation is contrary to all other elements. It is parallel to the crystal boundaries and more concentrated to the edge of the pyrite crystal. On the right edge two thin lines with medium intensity are recognizable whereas on the left edge one thin line with medium intensity and one thick line with high intensity are visible. Some parts of the thick bright zonation are congruent with the As zonations.

A zonation of Fe or Ag (Figure 50c; k) within the Pyrite is not visible.

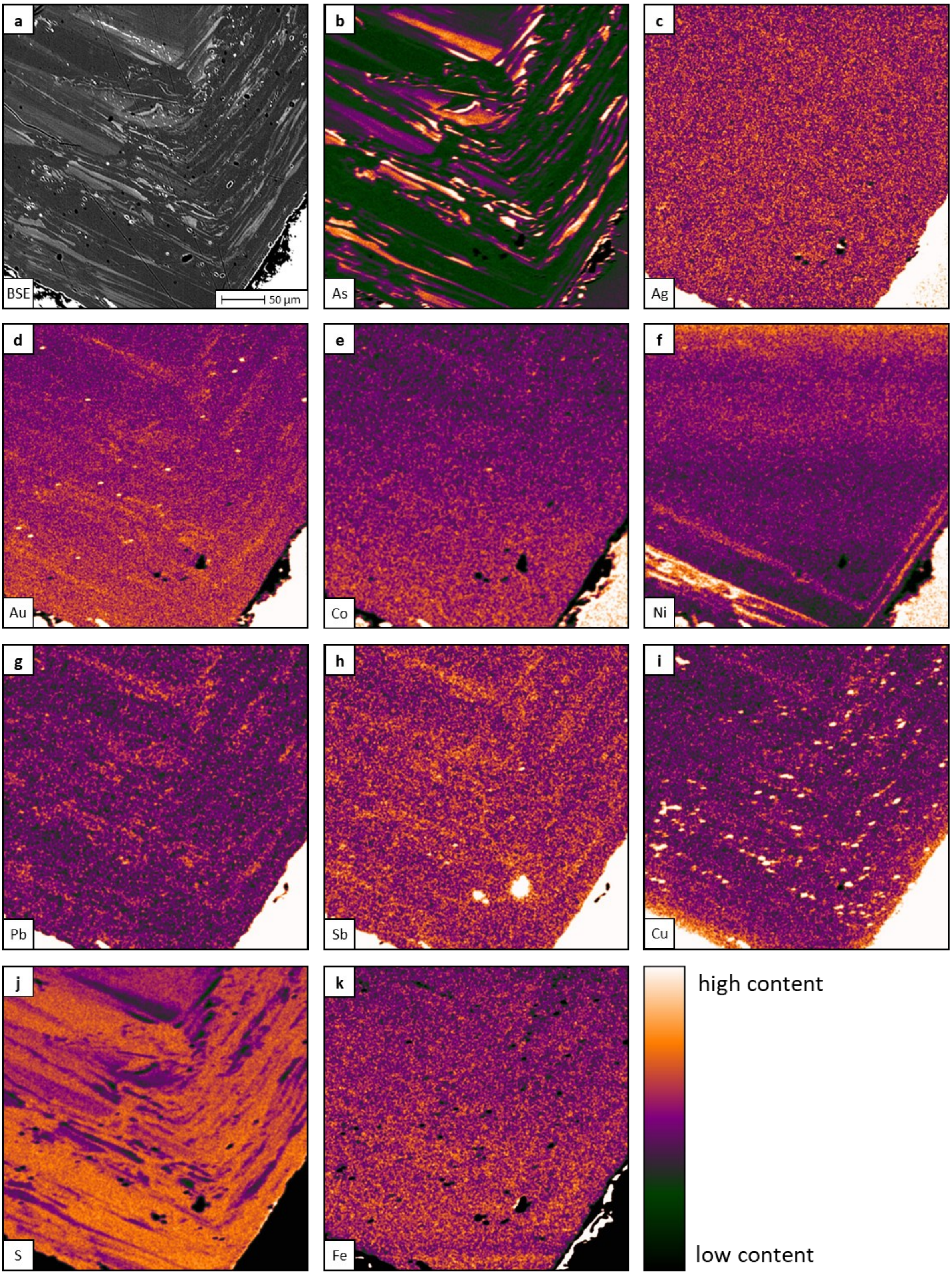

Figure 50:Pyrite element maps in sample A1463; a) BSE image; b) As EDS spectrometer; c) Ag WDS spectrometer; d) Au WDS spectrometer; e) Co EDS spectrometer; f) Ni EDS spectrometer; g) Pb EDS spectrometer; h) Sb WDS spectrometer; i) Cu EDS spectrometer; j) S EDS spectrometer; k) Fe WDS spectrometer.

3.4.3 EPMA ELEMENT MAP PM-RG-03 (ROTGÜLDEN)

As can be seen in the BSE image (Figure 51a), these are hypidiomorphic crystals which have a straight, partly rounded and sharp boundary to each other. A clear zonation of the pyrite crystals can be seen within the BSE image. A dark core surrounded by a light zone can be observed. This bright area has a varying thickness of 5 – 80 µm. The brightness also varies within this zone. The bright zone is surrounded by a dark rim which is as dark as the core. The bright zone is more irregular towards the core and straighter towards the dark rim. Furthermore, an interruption of the zonation can be seen in the far right lower third of the image. These interruption shows no zonation and appears dark. Conspicuous inclusions of other ore minerals are barely visible and are usually concentrated within the bright zonation. Some inclusions of gangue minerals are visible within the dark areas of the pyrite.

The zonation of As (Figure 51b) in the pyrite crystals is particularly pronounced. These high As contents, characterized by orange/white color, are congruent with the bright parts of the pyrites in the BSE image. The rather striped zoning on the left edge can be seen even more clearly in the As map. In the core and rim of the pyrites, the As content is relatively very low. Some purple lines close to the core indicate a slight As content. Gold, Pb, Sb and Cu (Figure 51d; g-i) show similar zonation patterns. Lead shows the highest content of the four elements, followed by Au, Cu and Sb. The maps of Au, Pb, Sb and Cu mirror the features seen in both the BSE image and the As map. In contrast to the other maps, no Au inclusions within the Au map are visible. Whereas inclusions with higher contents are increasingly recognizable in the Sb and Cu maps. In the Pb map are hardly any inclusions with an increased Pb content visible, which might be due to an interference of S on Pb. The inclusions within the Cu map are preferably recognized within or at the edge of the zonation. Silver (Figure 51c) does not show any zonation or inclusions. Sulfur. (Figure 51j) exhibits a zonation pattern contrary to that of As, Au, Pb, Sb and Cu. The S map shows clearly the higher the content of As, Au, Pb, Sb and Cu the lower the sulfur content. A zonation of Iron (Figure 51k) within the Pyrite is barely visible, inclusions are in turn recognizable. The Ni and Co maps (Figure 51e; f), on the other hand, show completely different zonation patterns. Cobalt shows slightly increased values partly congruent with As but in a different rather irregular pattern. The Co content is higher within a line on the left side of the pyrite crystal which runs from top to bottom. The Ni zoning is contrary to all other elements. An increased Ni content is recognizable within the same line as the higher Co content. Also, in the right middle of the map the Ni content is increased within a 25 µm big area. The increased Ni signal at the top of the map and the decreased signal at the bottom are due to an artefact.

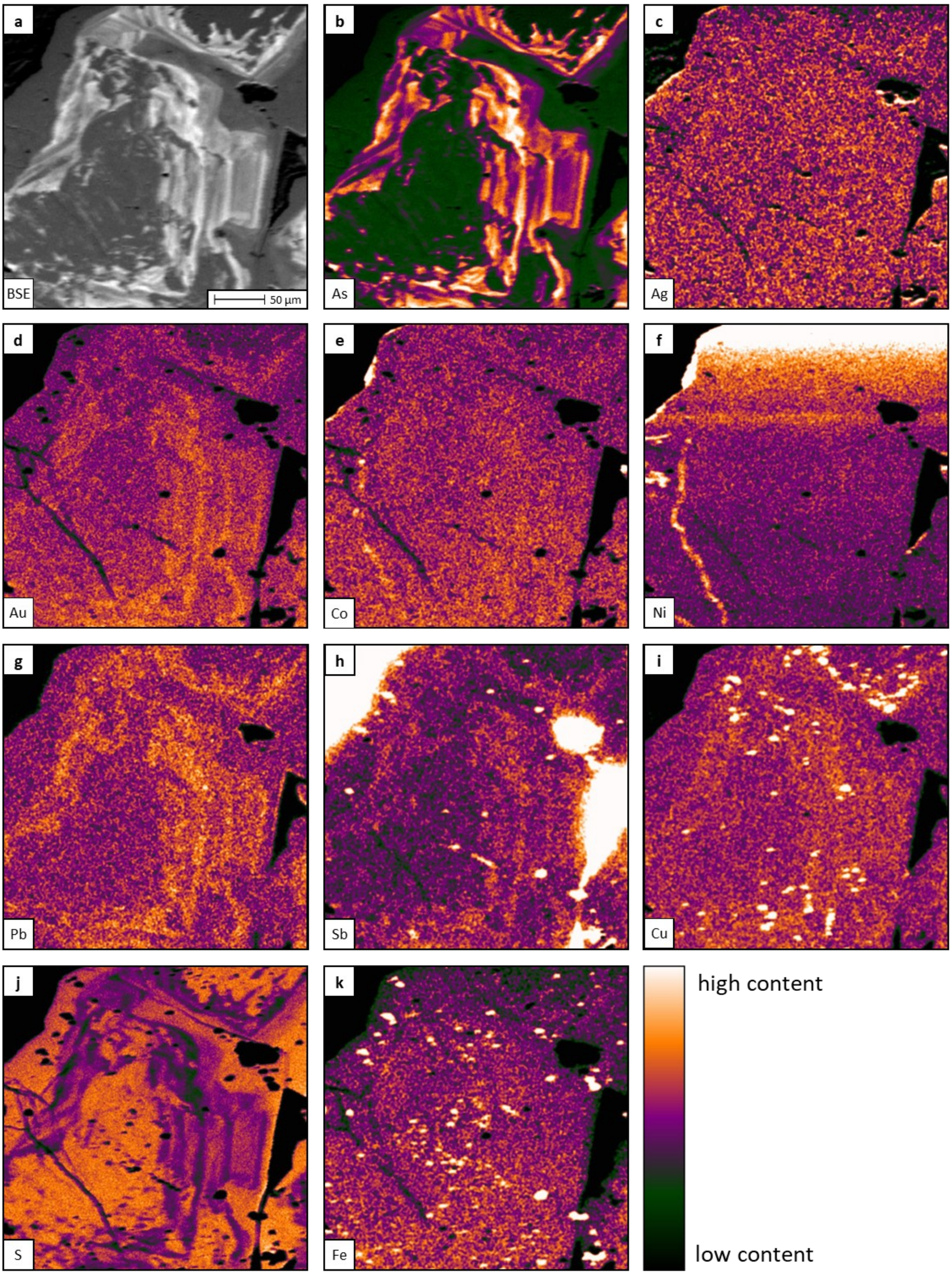

Figure 51: Pyrite element maps in sample PM-RG-03-1; a) BSE image; b) As EDS spectrometer; c) Ag WDS spectrometer; d) Au WDS spectrometer; e) Co EDS spectrometer; f) Ni EDS spectrometer; g) Pb EDS spectrometer; h) Sb WDS spectrometer; i) Cu EDS spectrometer; j) S EDS spectrometer; k) Fe WDS spectrometer.

4. DISCUSSION

4.1 FIELD OBSERVATIONS

The Fuscher Wegscheide district differs greatly from the others in terms of the surrounding rock and the mineralization found. The surrounding rock cellular dolomite present here, and the lead ores found strongly indicate that this is a different type of deposit from the Tauern gold veins. This is also described by Paar et al., 1978. It is also confirmed by the results of microscopy and LA-ICP-MS, as this was the only sample to show a cementation like microstructure with strongly rounded pyrite of various sizes situated in a matrix of pyrrhotite, chalcopyrite, galena and sphalerite (Figure 20).

The samples found in the Pasterze district strongly indicate the presence of mineralization. The amphibolite boulder that was found, which represents the host rock, showed small pyrite and chalcopyrite, indicating a pyrite rich mineralization of the host rock. Sample PM-PA-02 is from the quartzite with pyrite mineralization already described in the field results. It should be noted that the origin of the rock/sample is not known, but the origin can be restricted to an area with ~8km radius restricted by the surrounding mountains. Therefore, based on this and the measured values for Au (up to 7 ppm), As (up to 1.5 wt%) and Co (up to 1 wt%) within the pyrites, it is very likely that ore mineralization is still present within the Pasterze area. This is also supported by the two massive quartz veins exposed and examined at the Margaritzen reservoir, which contain pyrite and chalcopyrite and have already taken on a brown color in some areas due to the weathering of the ore minerals. These have already been described by Cornelius and Clar, 1939. However, it should be noted that, unlike the other Tauern gold veins, these do not strike NNE-SSW but ESE-WNW and dip ~ 45° to the NNE. which raises the question of whether this is the same vein mineralization as in the rest of the Tauern. Due to the strong weathering of the ore minerals within the quartz veins, the sample taken contained only fresh chalcopyrite with inclusions of sphalerite and Ag-Bi-Pb-tellurites. These are part of a complicated mineralization range and common companions for structurally controlled and late-Alpine gold mineralization (Cook et al., 2007; Putz et al., 2003), which suggests that these mineralized quartz veins belong to the Tauern gold vein type.

In the Mesenatten district the fuchsite is found with occasional pyrite and chalcopyrite within the mineralized veins, it can be assumed that it was formed from Cr-containing hydrothermal fluids.

Chromium was also be detected as a trace element in the pyrite, and it seems likely that the fuchsite is associated with the Tauern mineralization.

The investigations of the districts (Laserzen/Breitschitzen and Dösner Alm) in the area around Mallnitz, which are marked in IRIS (Weber et al., 2019) as former Au-As deposits, have shown that no tangible evidence of such existing mineralization can be found. No literature could be found regarding mineralization in these districts either. The prospecting holes found in the quartz veins at Laserzen/Breitschitzen could suggest former mining, but it is more likely that a mineralized vein was searched for here but abandoned after a short time because it gave no indication of gold mineralization.

As only one or two samples from each district were examined and each district shows significant changes in mineralization, possible sources of error cannot be ruled out. This also limits the representativeness of the statements. When taking samples, an attempt was made not only to take samples from dumps, but also to extract samples from underground directly from the mineralized vein. Many of the samples originate from the pair collection, for which the exact sampling point is only available to a limited extent, thus reducing the representativeness.

4.2 MINERALIZATION

4.2.1 MINERAL TEXTURE AND EVOLUTION OF MINERALIZATION

Pyrite is present in every polished section, except for PM-RG-01 and PM-PA-05b. Two types of pyrite can be observed in some polished sections. The xenomorphic pyrite, which often has very irregular to jagged grain boundaries and is cracked or fractured (Figure 30), usually shows a very irregular zonation, which has different appearance form district to district (Figure 17A, Figure 27B, Figure 28B). These appearances indicate that it is a 1st generation pyrite which has been repeatedly displaced in places during growth and has undergone changes in fluid chemistry. The irregular and jagged grain boundary contacts to galena in some areas indicate a displacement of the pyrite by the galena. The cracks indicate a tectonic overprinting of these pyrites. As these cracks also exist across the zonation, the tectonic overprinting took place after the formation of the zonation. The iron hydroxides which can be found in some polished sections at the crystal edge or along cracks are very likely a result of weathering, as some samples come from dumps and the minerals were therefore exposed to different weather conditions for 100+ years. The idiomorphic pyrites (Figure 22B, Figure 35A), on the other hand, have straight grain boundaries even in contact with other minerals and usually show a grain boundary parallel zonation, sometimes very fine oscillating zonations (Figure 23A, Figure 25B, Figure 37B). In addition, these rarely show evidence of cracks or larger inclusions of other minerals. Micrometer-sized inclusions (< 5 µm) can be recognized, which often occur along zonation boundaries. These observations indicate that these are 2nd generation pyrites, i.e. pyrites that crystallized at a later point in time and were no longer affected by strong tectonic overprinting. The fine inclusions along the zonation may be a sign of oversaturation of other elements as well as exsolution. The pyrites in Schellgaden differ from the others in that only xenomorphic pyrites are present, which are strongly rounded and contain hardly any cracks and only a few inclusions. In addition, barite inclusions were only observed in this district, which strongly indicates that the mineralizing fluids from this district differ significantly from the others and that different mineralization conditions prevailed.

Arsenopyrite is found in just under half of all samples, mainly in the districts located in the central gneisses. These arsenopyrites are often intergrown with pyrite and show just as many cracks. They are often more heavily fractured and more fissured than the pyrites (Gen 1). These cracks are also partially filled by chalcopyrite and/or galena. Isolated displacement splinting by galena can also be observed (Figure 23A). Occasionally cracks can also be seen running through both pyrite (Gen 1) and arsenopyrite. These observations show that the arsenopyrites crystallized at the same time as the pyrite (Gen 1) and were subsequently overprinted by tectonic activity.

The most frequently occurring non-ferrous metal sulfide in the samples is **galena**. This mineral always appears xenomorphic with irregular grain boundaries and is often in contact with all other minerals contained in the polished section. Since it is very frequently found in the cracks of the pyrites (Gen.1), it can be assumed that galena was mineralized later than these pyrites. In addition, a mixture of fine-grained anglesite and cerussite can also be seen in some polished sections, which is the result of weathering/alteration of galena under acidic or alkaline conditions (Benvenuti et al., 2000; Deer et al., 2013; Keim and Markl, 2015) where anglesite is often formed first and later transformed to cerussite. (Lara et al., 2011). In addition, the LA-ICP-MS measurements showed that the galena inclusions measured within the pyrites contain certain amounts of Bi and Ag as the three elements Pb, Bi and Ag show a positive correlation to each other, but only in the plots that include the inclusions. This indicates that the later stage fluid was not just rich in Pb but also in Ag and Bi and that during the precipitation of galena Ag and Bi were incorporated in its crystal structure.

Chalcopyrite is the second most frequently occurring non-ferrous metal sulfide in the samples after galena. As with galenite, it always appears as xenomorphic crystals with irregular grain boundaries and is often in contact with all other minerals contained in the polished section. It is also frequently found as inclusions in pyrites and also as gap fillers with galena in the cracks of the pyrites. These observations indicate that chalcopyrite was precipitated relatively simultaneously with galena and is therefore younger than the 1st generation pyrites. A separate case is the polished section PM-RG-01, which comes from the Kupferkieskaverne in the Rotgülden district. Almost half of the polished section consists of chalcopyrite, which contains so-called sphalerite stars (Figure 36). According to Castroviejo, 2023 and Ramdohr, 1975, these are the result of segregation of sphalerite contained in high-temperature (~ 400°C) chalcopyrite. However, studies by Marignac, 1989 describe the case of the formation of sphalerite stars by a supersaturation process at the growing fronts of chalcopyrite. According to several studies, the mineralization temperatures of the gold veins are up to 400 °C in some cases (Horner et al., 1997; Putz et al., 2003; Robl and Paar, 1994). This does not entirely rule out the possibility that the sphalerite stars are the result of segregation. A formation due to a supersaturation process at the growing fronts of chalcopyrite seems more plausible.

Sphalerite is also present in small quantities in many polished sections. This is usually found in the presence of chalcopyrite and galena and can occasionally also be recognized as inclusions in pyrite or in its cracks. Higher quantities of sphalerite can be found within the Erzwies samples (which represent the upper gold depleted mineralization zone) and the sample of Fuscher Wegscheide. This indicates that it is more found within the districts surrounded by carbonate rocks, where the mineralization takes on more of the characteristics of a Pb-Zn deposit. Fine chalcopyrite inclusions can be recognized everywhere within the sphalerite (so-called chalcopyrite disease). These are evenly distributed within the smaller sphalerite crystals, but within the large crystals they are more likely to be found at the edge of the crystal boundaries and cracks, similar to as observed in the Erzwies district, (Figure 32). These sphalerite inclusions in chalcopyrite are commonly referred to as the chalcopyrite disease and is a heavily debated phenomenon. Some argue that it is the result of exsolution of Cu from higher temperature sphalerite (Ramdohr, 1975), while others argue that is due to due to alteration, secondary replacement or co-precipitation (Bortnikov et al., 1991; Brandmaier, 1989; Castroviejo, 2023a). In the case of this work, the observations indicate that it is a combination of secondary replacement, due to the partial concentration at the edge of the crystal boundaries and cracks, and coprecipitation. Segregation is ruled out because at temperatures below 600°C the solubility of CuS in sphalerite is too low to explain the amount of disseminated chalcopyrite (Bowles et al., 2011; Castroviejo, 2023a). Therefore, it is assumed that sphalerite crystallized shortly before and during chalcopyrite mineralization. LA-ICP-MS measurements revealed that the sphalerite inclusions measured within the pyrites contain trace amounts of Cd and In. This is further supported by the positive correlation between Cd, In and Zn that is observed only in the data from which inclusions have not been culled, especially for the districts Bockhart, Erzwies, Goldzeche, Radhausberg and Hoher Goldberg. These districts lie within the central gneisses, suggesting that the presence of In and Cd rich sphalerites is host rock dependent. It is known that sphalerite is one of the most important Cd carriers and that it can also be incorporated into sphalerite in significant amounts. In addition, granites and gneisses can contain both In and Cd in certain quantities (Guo et al., 2023; Schwartz, 2000; Sinclair et al., 2006). It is therefore assumed that the fluids eluted In and Cd when passing through felsic rock and were then incorporated into sphalerite during mineralization.

Pyrrhotite is only present in 6 polished sections, mostly only as inclusions in pyrite. In the case of the Fuscher-Wegscheide district, pyrrhotite in combination with sphalerite, galena and chalcopyrite forms a matrix around the large, rounded, pyrite crystals. PM-RG-01 (Rotgülden) and PM-HW-01 (Hochwurten) are the only sample where large amounts of pyrrhotite were noted. A bird-eyes structure can also be recognized in the Hochwurten polished section. These are a result of supergene alteration of pyrrhotite to a fine-grained mixture with marcasite and pyrite. This also leads to the formation of Fe-hydroxides near these structures (Castroviejo, 2023b). This suggests that pyrrhotite has been exposed to temperatures above 230°C and is therefore no longer stable (Neumann, 2020).

The visible **gold** found in some polished sections occurs as the electrum crystals. The silver contents are highly variable but were always above 20 atom%. In 6 of 8 polished sections, the electrum crystals of various sizes are found on the edge of pyrite and/or galena, as well as in the cracks of pyrite. In polished section PM-SZ-01, electrum is located within a pyrite, close to the edge. From this, several fine cracks in the pyrite are also filled with electrum (Figure 28B), indicating that the electrum crystallized after the pyrite and filled the cavities. The electrum in polished section PM-RG-01 (deposit name) differs from the others in its Ag content. It contains 45 atom% Ag, while the average Ag content of all others is 21 - 40 atom%. In addition, near the electrum crystals there are fine cracks filled with pure silver within the pyrrhotite and chalcopyrite. Based on this data, it can be assumed that several generations of silver are involved here. This has already been discussed by Brandmaier, 1989, who divides the gold/electrum into three generations which have different average gold contents, with the silver-richest electrum as the youngest generation. Brandmaier, 1989 describes three different electrum mineralizations. The limited data and observations within this thesis show only two electrum generations: generation 1 is the Au richer electrum and crystallized shortly before/during the formation of galena and chalcopyrite, and generation 2 contains electrum with higher Ag contents as found in the sample PM-RG-01 (Rotgülden, Kupferkieskaverne).

The given mineralogical observations indicate that the fluids became richer in Ag over time. According to a study by Pohl and Belocky, 1999, the fluids are relatively poor in NaCl, so it can be assumed that Au was transported as a sulfide complex. According to Steadman et al., 2021 Au, Ag and As are preferentially incorporated into pyrite at temperatures 150-300°C. In this temperature range, $Au(HS)_2^-$ and $AuHS^0$ is the dominant phase of gold transportation (Williams-Jones et al., 2009). Ag^+ is considered to be a bit of a harder acid than Au^+ therefor Ag^+ will preferentially bind with Cl^- forming the $Ag(Cl)_2^-$ complex for transportation even in fluids with low salinity (Morrison et al., 1991). Therefore, one explanation for the increase in silver content in the fluid may be a change in salinity leading to higher Ag solubility (Gammons and Williams-Jones, 1995). Another explanation might be that the Au mineralization was due to a fluid change affecting the solubility of S but not the Cl solubility. However, the Ag measured with the LA-ICP-MS may be incorporated as elemental Ag in the pyrite crystal or be contained in the pyrite in the form of nanoinclusions. Further investigations are necessary to clarify this.

4.2.2 MAJOR TRACE ELEMENT ZONING IN PYRITE

For this work, zonations in pyrite were sought out to obtain information on fluid development. However, while many of the observed pyrites were zoned, zonations could not be observed in every polished section. The reason for this could be that there are truly no zonations or due to different settings of the SEM and the resulting different measurement and image qualities.

Both the EPMA mapping and the LA-ICP-MS measurements show that there are generally limited trace elements within the pyrite cores. This applies to both the xenomorphic and idiomorphic pyrite crystals. Nickel is an exception to this observation and is found in appreciable concentrations in the core of the pyrites. The zoning patterns of Ni and Co are very different in most cases, suggesting that they do not correlate with each other due to a different behavior in being incorporated in Pyrite (Figure 49e,f; Figure 50e,f). Cobalt and Ni often have similar zoning patterns to As, this is especially the case for Co. In polished section A1370 (Hoher Goldberg) it can also be seen that the Ni zonation occurs before the Co zonation. This can be explained by the position in the periodic table where Co is closer to Fe and thus has a more similar radius to Fe which ensures that it is preferably incorporated before the Ni. In the plot As/Ni (Figure 41F) it can be seen that As and Ni do not correlate with each other. Instead, the points within the figure of these deposits form clusters, meaning that for some deposits the As/Ni ratio stay the same regardless of where the pyrite was measured. These differences in zoning patterns can be explained by a change in fluid chemistry during crystallization or a change in crystallization conditions (e.g. temperature or pressure) as Co and Ni are predominantly incorporated into pyrite at temperatures above 300°C, whereas for As this is more the case for temperatures of 200-300°C (Steadman et al., 2021).

Furthermore, the EPMA mappings and the LA-ICP-MS show that Au and As have the same zoning pattern and that in this case the Au content is increased when the As content is elevated. This observation is consistent with the literature, wherein the As content facilitates the incorporation of Au in pyrites (Deditius et al., 2014; Gopon et al., 2019; Reich et al., 2005; Xie et al., 2024). According to these authors S is substituted by As^{-1} causing pair-bonded S atoms to break resulting in a Lewis base (partial charge imbalance) as well as point defects in the crystal lattice. At a point where ~200 As atoms replace S, a full 1- charge imbalance is created which can be balanced by Au^{1+} (Gopon et al., 2019). This means that the amount of Au that is incorporated in the lattice is constrained by the amount of As available. It should be mentioned that under oxidizing conditions As^{2+} can substitute for Fe^{2+} (Deditius et al., 2008), however in none of the maps was there an anti-correlation noted between As and Fe. According to Deditius et al., 2014; Gopon et al., 2019 and Reich et al., 2005 the limited uptake of Au is described by a line with a limiting Au/As-ratio of 1:200 (0.005) where samples above that ratio have Au in form of Au^0 nanonuggets, whereas samples plotting below that ratio show that Au in solid solution (Au^{1+}) is the dominant form. In the case of this work, Au is not only as visible Au but also as solid solution Au^{1+}present. This is supported by the EPMA mappings in which it is clearly recognizable that the Au zonation pattern corresponds to that of As, while S shows an inverse pattern, and Fe shows little to no zonation. This suggests that in the crystal lattice of the pyrite the S is substituted by As. The plots of the LA-ICP-MS measurements also show a clear positive correlation between As and Au. In Figure 52, the Au/As ratios are plotted with a hashed line representing the limit (1:200) above which Au nanoparticles are indicated to form. Since most of the Au/As ratios of each district are a below that hashed line the dominant form within the Pyrites might be Au in solid solution. However, this does not apply to Schellgaden, where most of the points lie above the hashed line and are therefore probably mostly present as nanoinclusions. Some points from the Hochwurten district and one from the Hoher Goldberg district also lay above the line. This indicates that the Au measured at this point is present as nanoinclusions, which in the case of Hoher Goldberg can also be conditionally confirmed by the EPMA maps as microinclusions (< 5 µm to < 20 µm) of Au can frequently be detected along the zonation boundaries within this map. This means that in that case the 1:200 Au/As ratio was exceeded, leading to the formation of nanonuggets (Gopon et al., 2019; Reich et al., 2005).

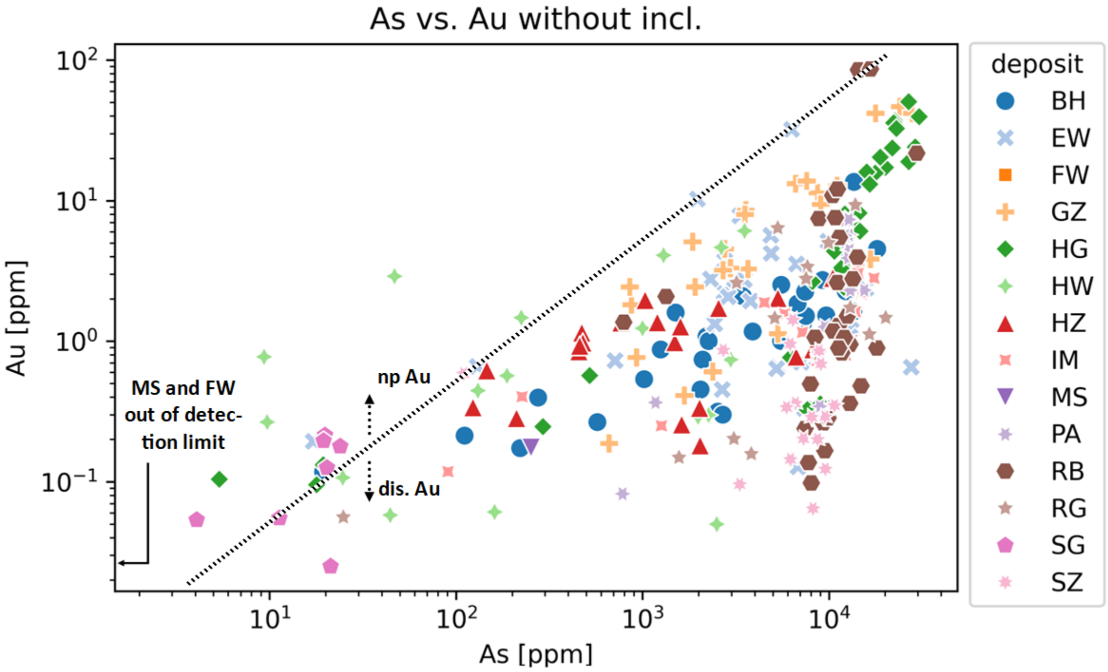

Figure 52: Whole rock geochemistry element correlation of Au and As for each district. The hashed line is representing the limit which below Au is incorporated in Pyrite as solid solution. Whereas above Au nanoparticles are intended to form. The hashed line is taken from Reich et al., 2005.

4.2.3 REGIONAL CHANGES IN AU / AS CONTENT IN PYRITE ACROSS THE TAUERN

In general, four regional distinctions can be made between (1) districts in which the Au content is high, to varying degrees, while the As content remains fairly constant (Hoher Goldberg, Radhausberg, Siglitz, Pasterze, Rotgülden); (2) districts that have a medium As and Au contents and whose ratios are rather highly variable (Hierzbach-Schiedalpe, Hochwurten, Erzwies); (3) Districts which show a positive correlation with increasing Au values with increasing As values (Bockhart, Goldzeche); (4) Districts which have no/hardly any Au values (Mesenatten, Fuscher Wegscheide) or which have only low As and Au values (Schellgarden).

The fact that no zonations were observed in the Mesenatten and Fuscher Wegscheide districts and no/hardly any Au values were measured supports the assumption that these are not typical Tauern gold mineralization’s. Both are also the only ones to lie within the carbonate-rich rocks of the Modereck nappe, and the carbonate host rock might be the cause for the atypical mineralization style. In the case of Carlin gold deposits, the pyrites with solid solution gold are located within Fe-rich carbonate rocks.

The Fe content of these rocks reacts with the S-rich fluid to form pyrite and incorporate the Au^+, creating the for Carlin gold typical zonations. In the case of the Tauern mineralization, as already mentioned, no zonations or gold contents in the pyrites are evident within the carbonates, whereas the pyrites within the orthogneisses show zonations and Au-As contents typical of Carlin gold type within the pyrites. The reason for this is different mineralization conditions/mechanisms such as the possible lack of Fe in the carbonates, which led to this atypical mineralization. As already described in Chapter 1.3.2, the solubility of Au in the fluid depends, among other things, on the pH. The interaction between fluid and carbonate rock presumably led to a slight increase in pH and thus to an increase in the solubility of Au in the fluid (Diamond, 1986; Foster and Seward, 1991; Pokrovski et al., 2019). This would also explain the change in the mineral assemblage in the Erzwies district where the change from gold-rich ore (below) to gold-poor ore (above, near and within the marbles) which was already described by Vavtar, 1982.

The Schellgaden district has one of the lowest Au and As values measured of all, forming its own cluster within the scatter plots. This means that regardless of the measuring point in the pyrite, the As and Au contents are always relatively equal. Schellgaden has with an average 0.008 the highest Au:As-ratio compared to the other districts, which speaks for a high Au content in relation to As. This ratio is also above the ratio 1:200 (0.005) as described by Reich et al. 2005 and Gopon et al., 2019, leading to the fact that Au as nanoinclusions is high likely the dominant phase which could be an explanation for why no zonation could be visible within the Pyrites of the Schellgaden district. This distinguishes Schellgarden intensely from the other districts. The absence of As can also be observed petrographically as no arsenopyrite is present in the two polished sections of Schellgarden (A1979, A1980), and the absence of arsenopyrite has already been described in various publications (Amann et al., 1997; Friedrich, 1968; Krenn et al., 2011). In addition, it is located at the edge of the Hohe Tauern and is the the only one that were ductile deformed with the Variscan basement rocks. Additionally, the pyrites contain very few to almost no inclusions, which is also only the case in this district. These observations suggest that this is a different type of mineralization than that of the Tauern gold veins. Some literature suggests that this type of mineralization is older than the Tauern gold veins (Amann et al., 1997; Krenn et al., 2011), but no statement can be made based on the observations made here.

4.2.4 CORRELATION OF TRACE ELEMENTS BETWEEN GOLD AND PYRITE

The measurements of the Rotgülden district show a comparatively high content of Sb within the electrum crystal compared to the other districts, but no to hardly any Sb (< 3 ppm) within the measured pyrites indicating that the electrum mineralization happened at a later point of time with a different fluid chemistry. It must also be noted that no pyrites are present in the polished section of the measured electrum (PM-RG-01), which means that the values can only be compared with the measured values of the other Rotgülden gold polished section (PM-RG-03). Although these polished sections both come from the Rotgülden district, they come from different dumps/mineralization veins within the Rotgülden district. The polished section with the electrum (PM-RG-01) comes from the Kupferkieskaverne, a copper-rich mineralization as the name suggests.

Compared to the other districts, Schellgaden shows the highest copper content in the electrum crystals with values of 88 cps to 333 cps. The measured pyrites, on the other hand, show no Cu content and chalcopyrite is also only found in very small quantities in the polished sections (estimated < 1 % for A1979 and < 5 % for A1980). The opposite is true for the samples that only contain small amounts of Cu in the gold, where low Cu contents can be seen in the pyrite. Often also very high values due to Ccp micro-inclusions in the pyrites. In addition, the Schellgaden district is the only one with Pd values measured in the electrum which rules out the possibility that this might be a remobilization of electrum from the other surrounding Tauern gold veins. As the element Pd was not part of the pyrite measurements, no comparisons can be made in this regard. These observations indicate that the fluids that led to this mineralization had a recognizably different composition than those of the other districts. This confirms that Schellgaden is not part of the typical Tauern mineralization.

5. CONCLUSION

The following conclusions can be drawn:

(1) Within many former mining districts there are still numerous indications of the former mining of the mineralized veins. The mineralized lode rocks found in the Pasterze area as well as the mineralized quartz veins indicate the presence of Tauern vein mineralization, the former mining (between 1446 and 1661) is probably still buried under the Pasterze glacier. The former mining areas Laserzen/Breitschitzen and Dösner Alm near Mallnitz marked in IRIS could not be confirmed as such.

(2) Two generations of pyrite were identified, both showing zonations with different zoning patterns. In both, elevated values of Au and As were found within the brighter zoning areas (BSE images). The correlations between As and Au within the pyrites support a solid solution of Au within the pyrites as a function of As content as found in Carlin-type deposits, except that the surrounding main mineral is quartz. In addition, two electrum generations could be identified, with the Ag-rich electrum as the younger generation and the Au-rich electrum as the older generation.

(3) A dependence of the mineralization on the host rock can be observed to a limited extent. In carbonate host rocks such as those found in Mesenatten, Fuscher Wegscheide and the upper section of Erzwies, gold mineralization cannot be observed. However, it seems that the hostrocks of the other districts do not have significant influence on the ore mineralization whether it is located within the orthogneisses or within metasedimentary rocks of the Penninic. No statement can be made about the Schellgaden district with regard to hostrock dependence, as this is not a typical Tauern mineralization.

(4) The results of the gold measurements support the commonly accepted interpretation that the Schellgaden district is a pre-variscan deposit with a different fluid composition than the classic (younger alpidic) Tauern gold veins. However, whether it is an older mineralization, as described in the literature, cannot be determined in this work.

(5) As there are many old mining districts in the Hohe Tauern and each mineralization within a district is very variable and different, more scientific investigations must be carried out for a more precise regional comparison. Many additional samples must be examined for each district in order to be able to make representative statements for each district and to minimize sources

of error. In particular, scientific studies of fluid inclusions would provide further information on the regional origin and composition of the fluids.

LITERATURE

AKK Ackerbau-Ministerium, 1895. Die Resultate der Untersuchung des Bergbau-Terrains in den Hohen Tauern. Wien, K. K. Hof- und Staatsdruckerei, Wien.

Amann, G., Daxner, G., Neubauer, F., Paar, W., Steyrer, H.-P., 1997. Structural evolution of the Schellgaden gold district, eastern Tauern window, Austria - a preliminary report 215–228.

Benvenuti, M., Mascaro, I., Corsini, F., Ferrari, M., Lattanzi, P., Parrini, P., Costagliola, P., Tanelli, G., 2000. Environmental mineralogy and geochemistry of waste dumps at the Pb(Zn)-Ag Bottino mine, Apuane Alps, Italy. ejm 12, 441–453. https://doi.org/10.1127/0935-1221/2000/0012-0441

Bergmaier, M., 1991. Lagerstättenkundliche Untersuchungen der Goldvererzungen im Siglitz-Pochkar-Revier bei Böckstein. (Unveröff. Diss.). Univ. Salzburg, Salzburg.

Bertrand, A., Rosenberg, C., Rabaute, A., Herman, F., Fügenschuh, B., 2017. Exhumation mechanisms of the Tauern Window (Eastern Alps) inferred from apatite and zircon fission track thermochronology: EXHUMATION OF THE TAUERN WINDOW. Tectonics 36, 207–228. https://doi.org/10.1002/2016TC004133

Bortnikov, N.S., Genkin, A.D., Dobrovol'skaya, M.G., Muravitskaya, G.N., Filimonova, A.A., 1991. The nature of chalcopyrite inclusions in sphalerite; exsolution, coprecipitation, or "disease"? Economic Geology 86, 1070–1082. https://doi.org/10.2113/gsecongeo.86.5.1070

Bowles, J., Howie, R., Vaughan, D., Zussman, J., 2011. Rock-forming minerals: Non-silicates: Oxides, hydroxides and sulphides. Geological Society.

Brandmaier, P., 1989. Gangförmige Gold - Silber - Mineralisation im Penninikum der Hohen Tauern: Die alten Goldbergbaue Hirzbach und Schiedalpe westlich von Fusch an der Glocknerstraße. (Unveröff. Diss.). Univ. Salzburg, Salzburg.

Canaval, R., 1896. Das Bergbau-Terrain in den Hohen Tauern. Jb. d. naturlristor, kandesmuseums v. Kiimten 24, 81–84.

Castroviejo, R., 2023a. A Practical Guide to Ore Microscopy—Volume 2: Ore Textures and Automated Ore Analysis. Springer International Publishing, Cham. https://doi.org/10.1007/978-3-031-18954-8

Castroviejo, R., 2023b. Pyrrhotite (po/pyrrhotite) Fe1- xS (x= 0 to 0.17): Hexagonal/Monoclinic, in: A Practical Guide to Ore Microscopy—Volume 1: Mineral Identification. Springer, pp. 613–620.

Cech, B., 2015. Tauerngold - Historische und montanarchäologische Zeugnisse zum Edelmetallbergbau in den Ostalpen, in: Bergauf Bergab. 10.000 Jahre Bergbau in Den Ostalpen. pp. 571–576.

Cook, N.J., Chryssoulis, S.L., 1990. Concentrations of invisible gold in the common sulfides. The Canadian Mineralogist 28, 1–16.

Cornelius, H., Clar, E., 1935. Erläuterungen zur geologischen Karte des Grossglocknergebietes: aufgenommen im Auftrage des Deutschen und Osterreichischen Alpenvereines. Geologische Bundesanstalt.

Cornelius, H.P., Clar, E., 1939. Geologie des Großglocknergebietes (I. Teil). Hollinek, Wien.

Craig, J.R., Vaughan, D.J., 1994. Ore microscopy and ore petrography, 2nd ed. ed. J. Wiley, New York Chichester Brisbane [etc.].

Craig, J.R., Vokes, F.M., Solberg, T.N., 1998. Pyrite: physical and chemical textures. Mineralium Deposita 34, 82–101. https://doi.org/10.1007/s001260050187

Deditius, A.P., Reich, M., Kesler, S.E., Utsunomiya, S., Chryssoulis, S.L., Walshe, J., Ewing, R.C., 2014. The coupled geochemistry of Au and As in pyrite from hydrothermal ore deposits. Geochimica et Cosmochimica Acta 140, 644–670. https://doi.org/10.1016/j.gca.2014.05.045

Deditius, A.P., Utsunomiya, S., Ewing, R.C., Kesler, S.E., 2009. Nanoscale “liquid” inclusions of As-Fe-S in arsenian pyrite. American Mineralogist 94, 391–394. https://doi.org/10.2138/am.2009.3116

Deditius, A.P., Utsunomiya, S., Reich, M., Kesler, S.E., Ewing, R.C., Hough, R., Walshe, J., 2011. Trace metal nanoparticles in pyrite. Ore Geology Reviews 42, 32–46. https://doi.org/10.1016/j.oregeorev.2011.03.003

Deditius, A.P., Utsunomiya, S., Renock, D., Ewing, R.C., Ramana, C.V., Becker, U., Kesler, S.E., 2008. A proposed new type of arsenian pyrite: Composition, nanostructure and geological significance. Geochimica et Cosmochimica Acta 72, 2919–2933. https://doi.org/10.1016/j.gca.2008.03.014

Deer, W.A., Howie, R.A., Zussman, J., 2013. An introduction to the rock-forming minerals, Third edition. ed. The Minerological Society, London.

Diamond, L.W., 1986. Hydrothermal geochemistry of late-metamorphic gold-quartz veins at Brusson, Val d’Ayas, Pennine Alps, NW. Italy. ETH Zurich. https://doi.org/10.3929/ETHZ-A-000468814

Durrant, S.F., 1999. Laser ablation inductively coupled plasma mass spectrometry: achievements, problems, prospects. J. Anal. At. Spectrom. 14, 1385–1403. https://doi.org/10.1039/a901765h

Ertl, R.F., 2007. Heiligenblut, das Glocknerdorf: eine Chronik der Gemeinde Heiligenblut. Eigenverl. d. Gemeinde Heiligenblut.

Exner, C., 1982. Geologie der zentralen Hafnergruppe (Hohe Tauern). Jahrbuch der Geologischen Bundesanstalt 125, 51–154.

Exner, C., 1971. Geologie der peripheren Hafnergruppe (Hohe Tauern). Jb. d. geol. Bundesanstalt 114, 1–119.

Exner, C., 1964. Erläuterungen zur Geologischen Karte der Sonnblickgruppe; Maßstab 1: 50.000, Wien: Geol. Bundesanstalt.

Favre, P., Stampfli, G.M., 1992. From rifting to passive margin: the examples of the Red Sea, Central Atlantic and Alpine Tethys. Tectonophysics 215, 69–97. https://doi.org/10.1016/0040-1951(92)90075-H

Feitzinger, G., 1989. Lagerstättenkundliche Untersuchungen an gangführenden Gold - Silber - Vererzungen der Sonnblickgruppe (Hohe Tauern, Kärnten). (Diss.). Univ. Salzburg, Salzburg.

Feitzinger, G., Paar, W.H., 1991. Gangförmige Gold-Silber-Vererzungen in der Sonnblickgruppe (Hohe Tauern, Kärnten). Archiv für Lagerstättenforschung der Geologischen Bundesanstalt 13, 17–50.

Fitzsimons, S.J., Veit, H., 2001. Geology and Geomorphology of the European Alps and the Southern Alps of New Zealand: A Comparison. Mountain Research and Development 21, 340–349. https://doi.org/10.1659/0276-4741(2001)021[0340:GAGOTE]2.0.CO;2

Foster, R., Seward, T., 1991. The hydrothermal geochemistry of gold. Gold metallogeny and exploration 37–62.

Frank, W., 1987. Metamorphic and Tectonic History of the Central Tauern Window / edited by H.W. Flugel and P. Faupl, in: Geodynamics of the Eastern Alps. F. Deuticke, pp. 34–54.

Friedrich, O.M., 1968. Die Vererzung der Ostaplen, gesehen als Glied des Gebiergsbaues. Archiv für Lagerstättenforschung in den Ostalpen 8. Bd., 1–136.

Friedrich, O.M., 1935. Zur Geologie der Goldlagerstättengruppe Schellgaden. Berg- und Hüttenmänn. Jb., 83, 34-39, 46-60; Wien.

Friedrich, O.M., 1934. Über den Vererzungstyp Rotgülden.- Sitz. Ber. Österr. Akad. d. Wiss., mathemat.-naturwiss. Kl., Abt. I, 143: 95–108.

Friedrich, O.M., Matz, K.B., 1939. Der Stüblbau zu Schellgaden. Berg- u. Hüttenmänn. Mh., 87, 3439; Wien.

Gammons, C.H., Williams-Jones, A.E., 1995. Hydrothermal geochemistry of electrum; thermodynamic constraints. Economic Geology 90, 420–432. https://doi.org/10.2113/gsecongeo.90.2.420

Gibert, F., Pascal, M.-L., Pichavant, M., 1998. Gold solubility and speciation in hydrothermal solutions: experimental study of the stability of hydrosulphide complex of gold (AuHS°) at 350 to 450°C and 500 bars. Geochimica et Cosmochimica Acta 62, 2931–2947. https://doi.org/10.1016/S0016-7037(98)00209-9

Gopon, P., Douglas, J.O., Auger, M.A., Hansen, L., Wade, J., Cline, J.S., Robb, L.J., Moody, M.P., 2019. A Nanoscale Investigation of Carlin-Type Gold Deposits: An Atom-Scale Elemental and Isotopic Perspective. Economic Geology 114, 1123–1133. https://doi.org/10.5382/econgeo.4676

Gribble, C., 2012. A practical introduction to optical mineralogy. Springer Science & Business Media.

Griesmeier, G., 2021. GEOFAST - Zusammenstellung ausgewählter Archivunterlagen der Geologischen Bundesanstalt 1:50.000: 154 Rauris: Stand 2021, Wien.

Guo, X., Zhou, T., Wang, F., Fan, Y., Fu, P., Kong, F., 2023. Distribution of Co, Se, Cd, In, Re and other critical metals in sulfide ores from a porphyry-skarn system: A case study of Chengmenshan Cu deposit, Jiangxi, China. Ore Geology Reviews 158, 105520. https://doi.org/10.1016/j.oregeorev.2023.105520

Hartmann, A., 1978. Ergebnisse spektralanalytischer Untersuchung späthallstatt-und laténezeitlicher Goldfunde vom Dürrnberg, aus Südwestdeutschland, Frankreich und der Schweiz. Der Dürrnberg bei Hallain. Münchner Beiträge zur Vorund Frühgeschichte.

Häusler, H., Demmer, W., Exner, C., Tollmann, A., 1995. Geologische Karte der Republik Österreich. 156 Muhr.

Höck, V., Koller, F., Seemann, R., 1994. Geologischer Werdegang der Hohen Tauern vom Ozean zum Hochgebirge. Mineral & Erz in den Hohen Tauern 29–48.

Horner, J., Neubauer, F., Paar, W., Hansmann, W., Koeppel, V., Robl, K., 1997. Structure, mineralogy, and Pb isotopic composition of the As-Au-Ag deposit Rotgülden, Eastern Alps (Austria): significance for formation of epigenetic ore deposits within metamorphic domes. Mineralium deposita 32, 555–568.

Keim, M.F., Markl, G., 2015. Weathering of galena: Mineralogical processes, hydrogeochemical fluid path modeling, and estimation of the growth rate of pyromorphite. American Mineralogist 100, 1584–1594. https://doi.org/10.2138/am-2015-5183

Keith, M., Häckel, F., Haase, K.M., Schwarz-Schampera, U., Klemd, R., 2016. Trace element systematics of pyrite from submarine hydrothermal vents. Ore Geology Reviews 72, 728–745. https://doi.org/10.1016/j.oregeorev.2015.07.012

Keith, M., Smith, D.J., Jenkin, G.R.T., Holwell, D.A., Dye, M.D., 2018. A review of Te and Se systematics in hydrothermal pyrite from precious metal deposits: Insights into ore-forming processes. Ore Geology Reviews 96, 269–282. https://doi.org/10.1016/j.oregeorev.2017.07.023

Koch, J., Günther, D., 2017. Laser Ablation Inductively Coupled Plasma Mass Spectrometry, in: Lindon, J.C., Tranter, G.E., Koppenaal, D.W. (Eds.), Encyclopedia of Spectroscopy and Spectrometry (Third Edition). Academic Press, Oxford, pp. 526–532. https://doi.org/10.1016/B978-0-12-803224-4.00024-8

Krenn, E., Putz, H., Finger, F., Paar, W.H., 2011. Sulfur-rich monazite with high common Pb in ore-bearing schists from the Schellgaden mining district (Tauern Window, Eastern Alps). Miner Petrol 102, 51–62. https://doi.org/10.1007/s00710-011-0170-x

Kreuss, O., 2021. GEOFAST - Zusammenstellung ausgewählter Archivunterlagen der Geologischen Bundesanstalt 1:50.000: 155 Bad Hofgastein: Stand 2021, Wien.

Lammerer, B., Weger, M., 1998. Footwall uplift in an orogenic wedge: the Tauern Window in the Eastern Alps of Europe. Tectonophysics 285, 213–230. https://doi.org/10.1016/S0040-1951(97)00272-2

Lara, R.H., Briones, R., Monroy, M.G., Mullet, M., Humbert, B., Dossot, M., Naja, G.M., Cruz, R., 2011. Galena weathering under simulated calcareous soil conditions. Science of The Total Environment S004896971100711X. https://doi.org/10.1016/j.scitotenv.2011.06.055

Marignac, Ch., 1989. Sphalerite stars in chalcopyrite: Are they always the result of an unmixing process? Mineral. Deposita 24, 176–182. https://doi.org/10.1007/BF00206440

Mokgalaka, N.S., Gardea-Torresdey, J.L., 2006. Laser Ablation Inductively Coupled Plasma Mass Spectrometry: Principles and Applications. Applied Spectroscopy Reviews 41, 131–150. https://doi.org/10.1080/05704920500510703

Moosleitner, F., 1994. Die Tauernregion in ur-und frühgeschichtlicher Zeit. Mineral Erz in den Hohen Tauern. Ausstellungskatalog des Naturhistorischen Museums Wien 2, 103–111.

Morrison, G.W., Rose, W.J., Jaireth, S., 1991. Geological and geochemical controls on the silver content (fineness) of gold in gold-silver deposits. Ore Geology Reviews 6, 333–364. https://doi.org/10.1016/0169-1368(91)90009-V

Mukherjee, I., Large, R.R., 2016. Pyrite trace element chemistry of the Velkerri Formation, Roper Group, McArthur Basin: Evidence for atmospheric oxygenation during the Boring Billion. Precambrian Research 281, 13–26. https://doi.org/10.1016/j.precamres.2016.05.003

Neumann, U., 2020. Guide for the microscopical identification of ore and gangue minerals. https://doi.org/10.15496/PUBLIKATION-38866

Onuk, P., Melcher, F., Mertz-Kraus, R., Gäbler, H.-E., Goldmann, S., 2017. Development of a matrix-matched sphalerite reference material (MUL-ZnS-1) for calibration of in situ trace element measurements by laser ablation-inductively coupled plasma-mass spectrometry. Geostandards and Geoanalytical Research 41, 263–272.

Paar, V.W.H., Chen, T.T., Günther, W., 1978. Extrem silberreicher Freibergit in Pb-Zn-Cu-Erzen des Bergbaues „Knappenstube", Hochtor, Salzburg. Carinthia II 35–42.

Paar, W., Topa, D., 1998. Mineralogie und Bildungsbedingungen von Glaserz der Tauerngoldgänge. Mitt. d. Österr. Min. Ges. 143.

Paar, W.H., Gunther, W., Gruber, F., 2006. Das Buch vom Tauerngold. Anton Pustet.

Palenik, C.S., Utsunomiya, S., Reich, M., Kesler, S.E., Wang, L., Ewing, R.C., 2004. "Invisible" gold revealed: Direct imaging of gold nanoparticles in a Carlin-type deposit. American Mineralogist 89, 1359–1366. https://doi.org/10.2138/am-2004-1002

Paton, C., Hellstrom, J., Paul, B., Woodhead, J., Hergt, J., 2011. Iolite: Freeware for the visualisation and processing of mass spectrometric data. J. Anal. At. Spectrom. 26, 2508. https://doi.org/10.1039/c1ja10172b

Pestal, G., 2005. Geologischer Bau des Tauernfensters – Erläuterungen zu Blatt 182 Spittal a.d. Drau. na.

Pfiffner, O.A., 1992. Alpine Orogeny, in: A Continent Revealed: The European Geotraverse Structure and Dynamic Evolution. Cambridge University Press, pp. 180–190.

Piaz, G.V.D., Bistacchi, A., Massironi, M., 2003. Geological outline of the Alps. Episodes 26, 175–180. https://doi.org/10.18814/epiiugs/2003/v26i3/004

Pohl, W., Belocky, R., 1999. Metamorphism and metallogeny in the Eastern Alps. Mineralium Deposita 34, 614–629. https://doi.org/10.1007/s001260050223

Pokrovski, G.S., Kokh, M.A., Proux, O., Hazemann, J.-L., Bazarkina, E.F., Testemale, D., Escoda, C., Boiron, M.-C., Blanchard, M., Aigouy, T., Gouy, S., De Parseval, P., Thibaut, M., 2019. The nature and partitioning of invisible gold in the pyrite-fluid system. Ore Geology Reviews 109, 545–563. https://doi.org/10.1016/j.oregeorev.2019.04.024

Posepny, F., 1880. Die Goldbergbaue der Hohen Tauern mit besonderer Berücksichtigung des Rauris Goldberges. Archiv f. praktische Geologie 1, 212–215.

Pownceby, M.I., MacRae, C.M., Wilson, N.C., 2007. Mineral characterisation by EPMA mapping. Minerals Engineering 20, 444–451. https://doi.org/10.1016/j.mineng.2006.10.014

Putz, H., 2000. Lagerstättenmineralogie von Edelmetallvererzungen im Altenbergtal, Silbereckformation, Lungau, Salzburg. (Unveröff. Dipl. Arb.). Univ. Salzburg.

Putz, H., Paar, W.H., Topa, D., Horner, J., L�ders, V., 2003. Structurally controlled gold and sulfosalt mineralization: the Altenberg example, Salzburg Province, Austria. Mineralogy and Petrology 78, 111–138. https://doi.org/10.1007/s00710-002-0230-3

Ramdohr, P., 1975. Die Erzmineralien und ihre Verwachsungen, 4., bearbeitete und erweiterte Auflage. ed. Akademie Verlag Berlin.

Ramdohr, P., Strunz, H., 1967. Klockmann’s lehrbuch der Mineralogie, 15. ed. Ferdinand Enke.

Reich, M., Deditius, A., Chryssoulis, S., Li, J.-W., Ma, C.-Q., Parada, M.A., Barra, F., Mittermayr, F., 2013. Pyrite as a record of hydrothermal fluid evolution in a porphyry copper system: A SIMS/EMPA trace element study. Geochimica et Cosmochimica Acta 104, 42–62. https://doi.org/10.1016/j.gca.2012.11.006

Reich, M., Kesler, S.E., Utsunomiya, S., Palenik, C.S., Chryssoulis, S.L., Ewing, R.C., 2005. Solubility of gold in arsenian pyrite. Geochimica et Cosmochimica Acta 69, 2781–2796. https://doi.org/10.1016/j.gca.2005.01.011

Rickard, D., Luther, G.W., 2007. Chemistry of Iron Sulfides. Chem. Rev. 107, 514–562. https://doi.org/10.1021/cr0503658

Robl, K., Paar, W.H., 1994. Fluid-Inclusion Untersuchungen an Golderzen der Goldzeche, Sonnblickgruppe,(Hohe Tauern, Kärnten). Mitt Österr Mineral Ges 139, 151–158.

Schmid, S.M., Fügenschuh, B., Kissling, E., Schuster, R., 2004. Tectonic map and overall architecture of the Alpine orogen. Eclogae geol. Helv. 97, 93–117. https://doi.org/10.1007/s00015-004-1113-x

Schmid, S.M., Scharf, A., Handy, M.R., Rosenberg, C.L., 2013. The Tauern Window (Eastern Alps, Austria): a new tectonic map, with cross-sections and a tectonometamorphic synthesis. Swiss J Geosci 106, 1–32. https://doi.org/10.1007/s00015-013-0123-y

Schuster, R., Kurz, W., Krenn, K., Fritz, H., 2013. Introduction to the Geology of the Eastern Alps. Berichte der Geologischen Bundes-Anstalt Wien 99, 121–133.

Schuster, R., Stüwe, K., 2010. Die Geologie der Alpen im Zeitraffer. Mitteilungen des naturwissenschaftlichen Vereins für Steiermark 140, 5–21.

Schwartz, M.O., 2000. Cadmium in Zinc Deposits: Economic Geology of a Polluting Element. International Geology Review 42, 445–469. https://doi.org/10.1080/00206810009465091

Sinclair, W.D., Kooiman, G.J.A., Martin, D.A., Kjarsgaard, I.M., 2006. Geology, geochemistry and mineralogy of indium resources at Mount Pleasant, New Brunswick, Canada. Ore Geology Reviews 28, 123–145. https://doi.org/10.1016/j.oregeorev.2003.03.001

Sindern, S., 2017. Analysis of Rare Earth Elements in Rock and Mineral Samples by ICP-MS and LA-ICP-MS. Physical Sciences Reviews 2. https://doi.org/10.1515/psr-2016-0066

Smith, A.H., Smith, M.M.H., 2004. Arsenic drinking water regulations in developing countries with extensive exposure. Toxicology 198, 39–44. https://doi.org/10.1016/j.tox.2004.02.024

Steadman, J.A., Large, R.R., Olin, P.H., Danyushevsky, L.V., Meffre, S., Huston, D., Fabris, A., Lisitsin, V., Wells, T., 2021. Pyrite trace element behavior in magmatic-hydrothermal environments: An LA-ICPMS imaging study. Ore Geology Reviews 128, 103878. https://doi.org/10.1016/j.oregeorev.2020.103878

Stefánsson, A., Seward, T.M., 2004. Gold(I) complexing in aqueous sulphide solutions to 500°C at 500 bar. Geochimica et Cosmochimica Acta 68, 4121–4143. https://doi.org/10.1016/j.gca.2004.04.006

Ulrich, T., Kamber, B.S., Jugo, P.J., Tinkham, D.K., 2009. IMAGING ELEMENT-DISTRIBUTION PATTERNS IN MINERALS BY LASER ABLATION - INDUCTIVELY COUPLED PLASMA - MASS SPECTROMETRY (LA-ICP-MS). The Canadian Mineralogist 47, 1001–1012. https://doi.org/10.3749/canmin.47.5.1001

Vavtar, F., 1982. Topomineralische Gold-Quarz-Gänge des Siglitz-Pochart-Erzwies-Revieres (Gastein, Hohe Tauern). Archiv für Lagerstättenforschung der Geologischen Bundesanstalt 2, 143.148.

Vernon-Parry, K.D., 2000. Scanning electron microscopy: an introduction. III-Vs review 13, 40–44.

Vlassopoulos, D., Wood, S.A., 1990. Gold speciation in natural waters: I. Solubility and hydrolysis reactions of gold in aqueous solution. Geochimica et Cosmochimica Acta 54, 3–12. https://doi.org/10.1016/0016-7037(90)90189-R

Walter, R., 2016. Erdgeschichte: die Geschichte der Kontinente, der Ozeane und des Lebens, 7., überarbeitete und verbesserte Auflage. ed. Schweizerbart, Stuttgart.

Warr, L.N., 2021. IMA–CNMNC approved mineral symbols. MinMag 1–30. https://doi.org/10.1180/mgm.2021.43

Weber, L., Schedl, A., Lipiarski, P., 2019. IRIS Online (Interaktives Rohstoff Informations System), ein Beispiel für ein weltweit einzigartiges digitales Rohstoff-Informationssystem. Berg Huettenmaenn Monatsh 164, 56–66. https://doi.org/10.1007/s00501-018-0810-0

Williams-Jones, A.E., Bowell, R.J., Migdisov, A.A., 2009. Gold in Solution. Elements 5, 281–287. https://doi.org/10.2113/gselements.5.5.281

Wilson, S., Ridley, W., Koenig, A., 2002. Development of sulfide calibration standards for the laser ablation inductively-coupled plasma mass spectrometry technique. Journal of Analytical Atomic Spectrometry 17, 406–409.

Xie, Z., Gopon, P., Xia, Y., Douglas, J.O., Cline, J., Liu, J., Tan, Q., Xiao, J., Wen, Y., Chen, Y., Li, P., Moody, M.P., 2024. Does SW China have Carlin-type gold deposits? A micro- to atomic-scale perspective. Miner Deposita 59, 757–772. https://doi.org/10.1007/s00126-023-01231-6

Yang, S.-Y., 2022. Electron Probe Microanalysis In Geosciences: Analytical Procedures And Recent Advances. At.Spectrosc. 43. https://doi.org/10.46770/AS.2021.912

Zhou, W., Wang, Z.L., 2007. Scanning microscopy for nanotechnology: techniques and applications. Springer science & business media.

Zhu, Y., An, F., Tan, J., 2011. Geochemistry of hydrothermal gold deposits: A review. Geoscience Frontiers 2, 367–374. https://doi.org/10.1016/j.gsf.2011.05.006

ABBREVIATIONS

Apy	Arsenopyrite
Ag	Silver
Ang	Anglesite
BH	Bockhart
Bou	Boulangerite
Brt	Barite
BSE	Back-scattered electron detector
Ccp	Chalcopyrite
Cer	Cerussite
Cst	Cassiterite
Cv	Covellite
El	Electrum
EW	Erzwies
FW	Fuscher Wegscheide
Gn	Galena
GZ	Goldzeche
HG	Hoher Goldberg
HW	Hochwurten
HZ	Hierzbach-Schiedalpe
LA-ICP-MS	Laser ablation inductively coupled plasma mass spectrometry
IM	Imhof-adit
Lm	Limonite
Mnz	Monazite
MS	Mesenatten
PA	Pasterze
Pyh	Pyrrhotite
Py	Pyrite
RB	Radhausberg
RG	Rotgülden
Rt	Rutile
SEM	Scanning electron microscope

SG	Schellgaden
Sp	Sphalerite
Stn	Stannite
SZ	Siglitz
WDS	Wavelength dispersive spectrometer
Xtm	Xenotime

(Mineral abbreviations after Warr, 2021)

LIST OF FIGURES

LIST OF TABLES

APPENDIX

I. Overview pictures of each sample

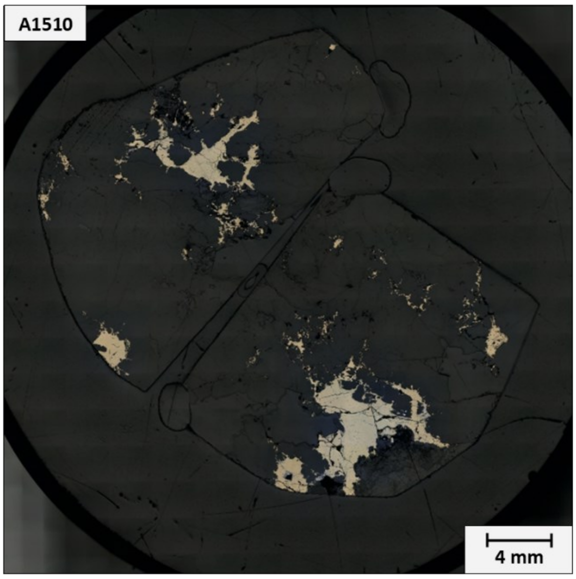

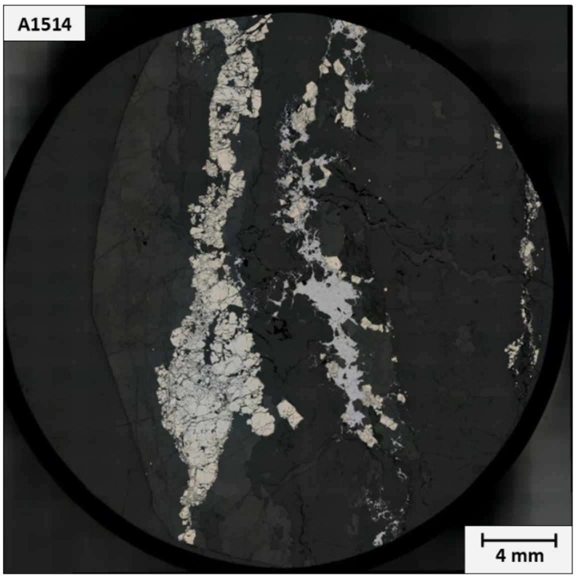

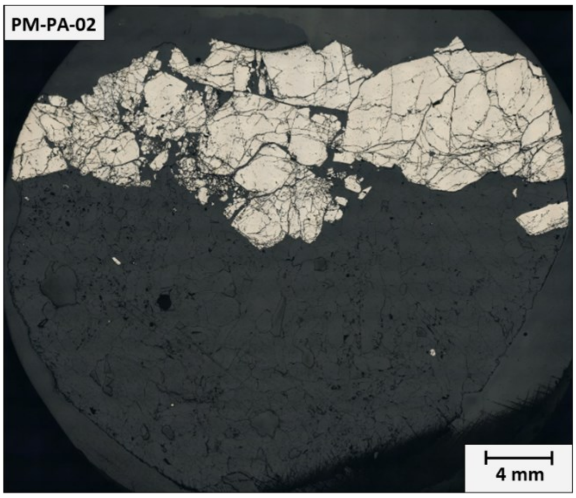

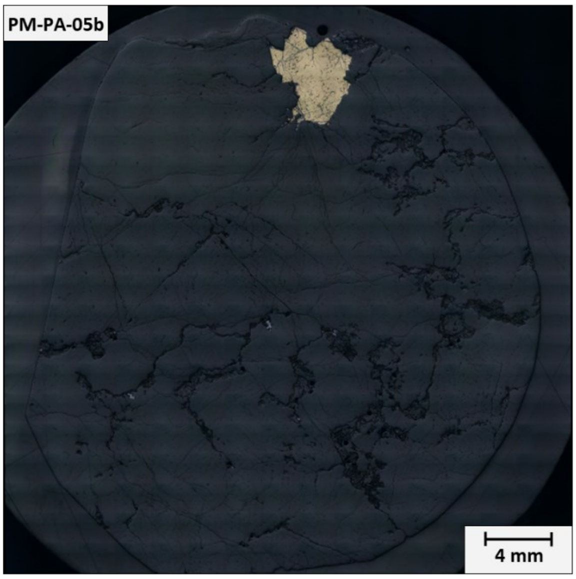

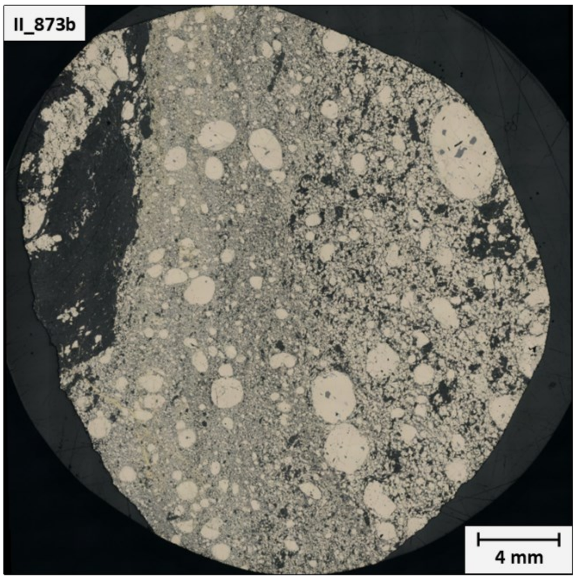
II_873b
4 mm

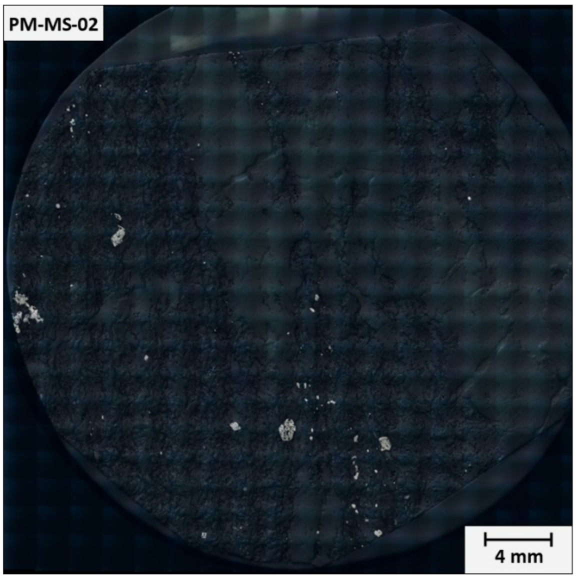
PM-MS-02
4 mm

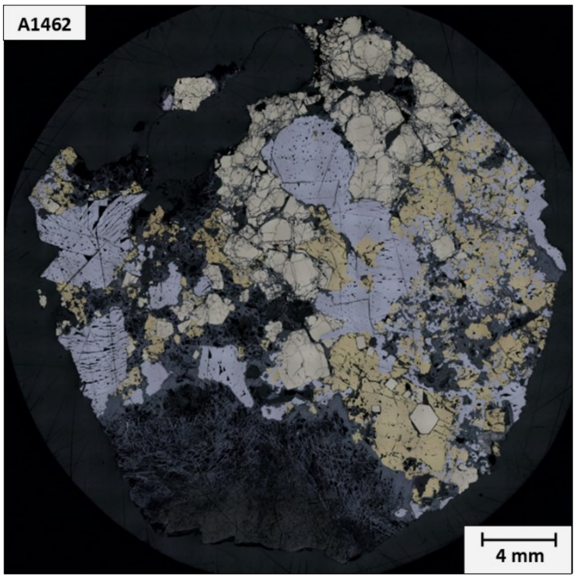
A1462
4 mm

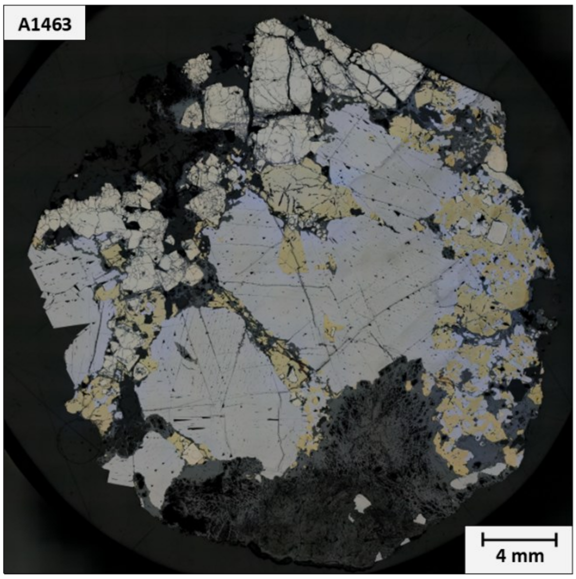
A1463
4 mm

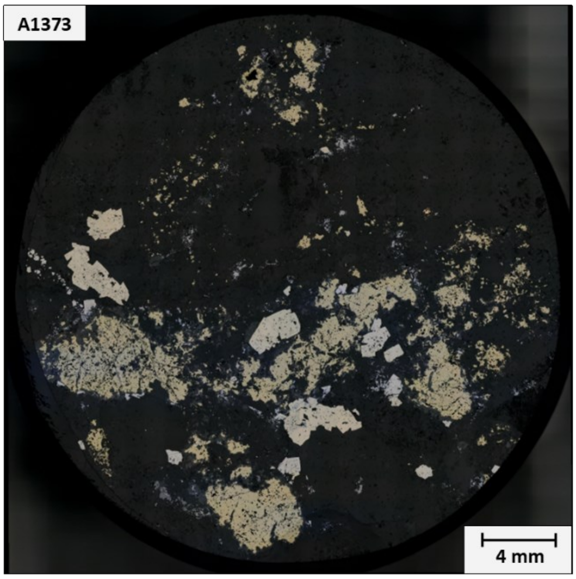
A1373
4 mm

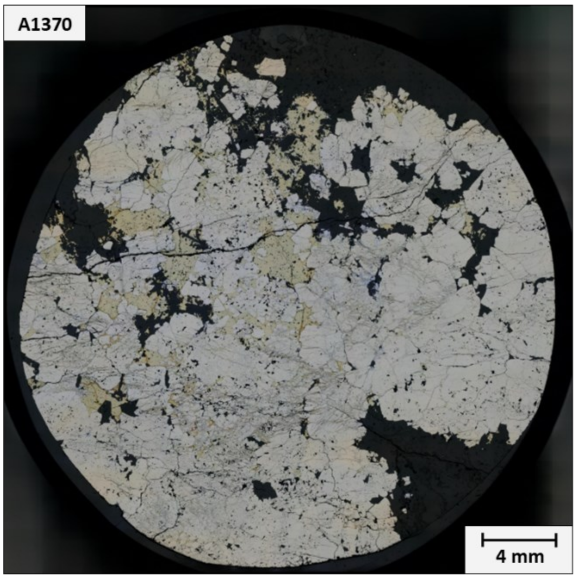
A1370
4 mm

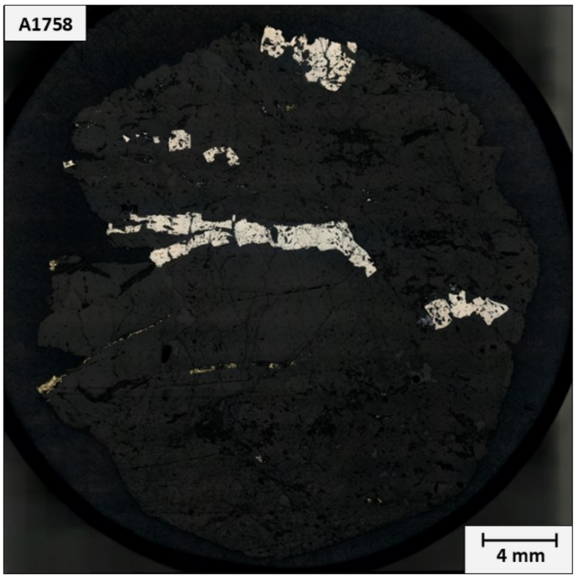
A1758
4 mm

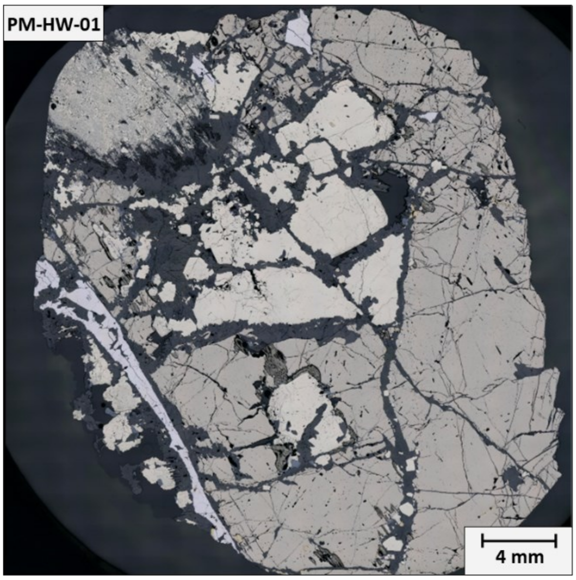
PM-HW-01
4 mm

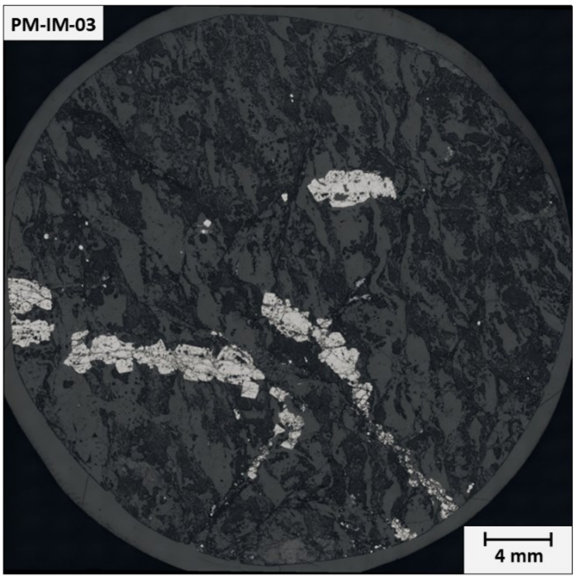
PM-IM-03
4 mm

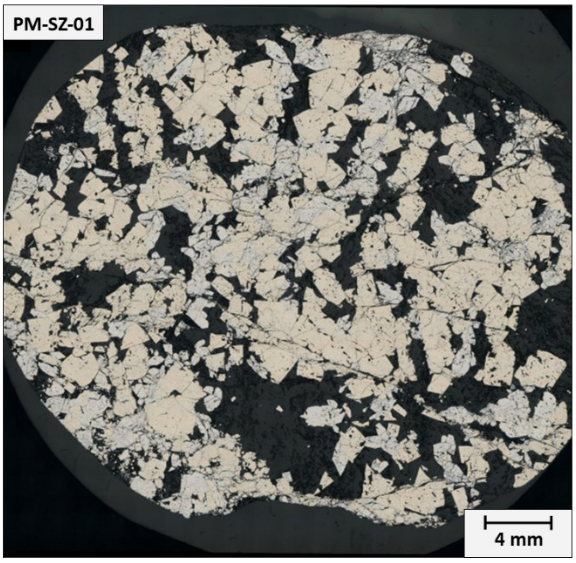
PM-SZ-01
4 mm

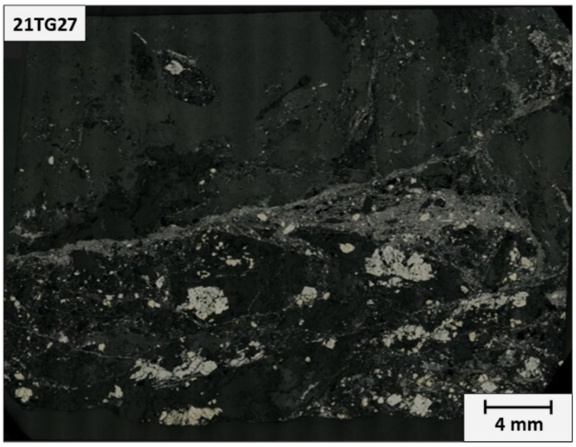
21TG27
4 mm

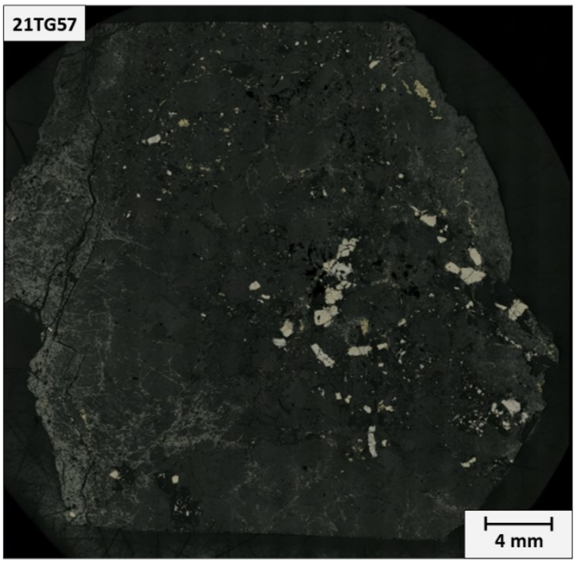
21TG57
4 mm

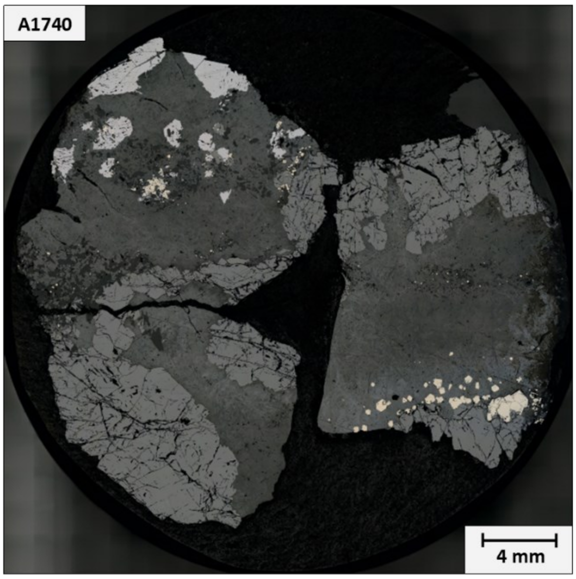
A1740
4 mm

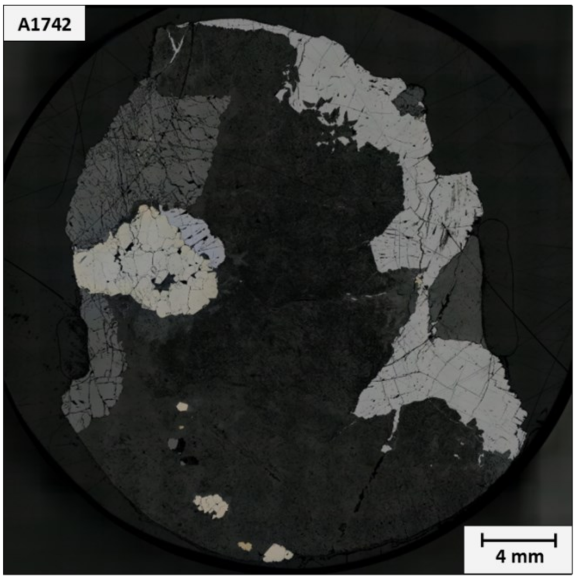
A1742
4 mm

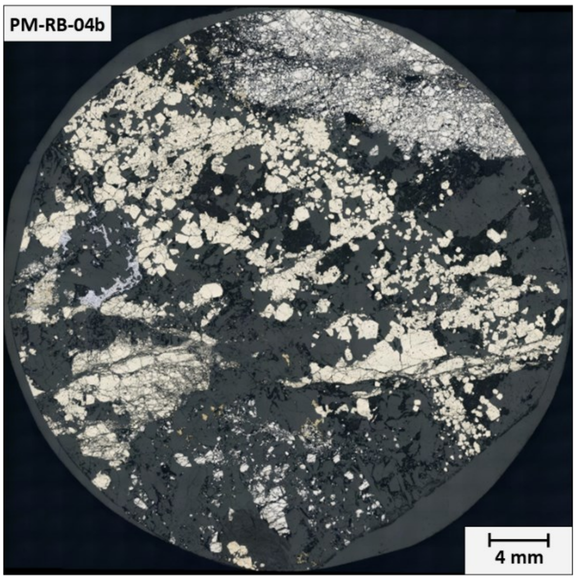
PM-RB-04b
4 mm

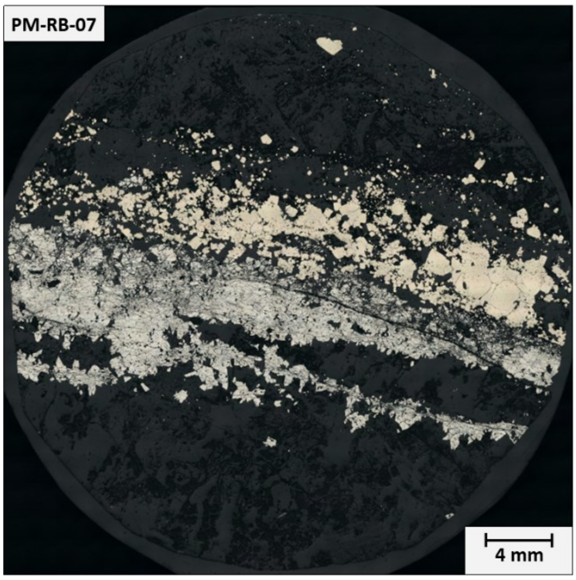
PM-RB-07
4 mm

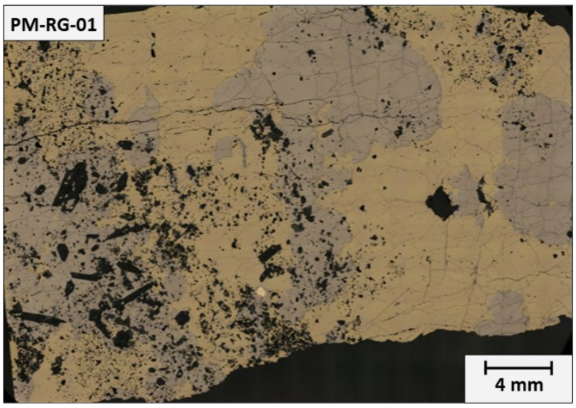
PM-RG-01
4 mm

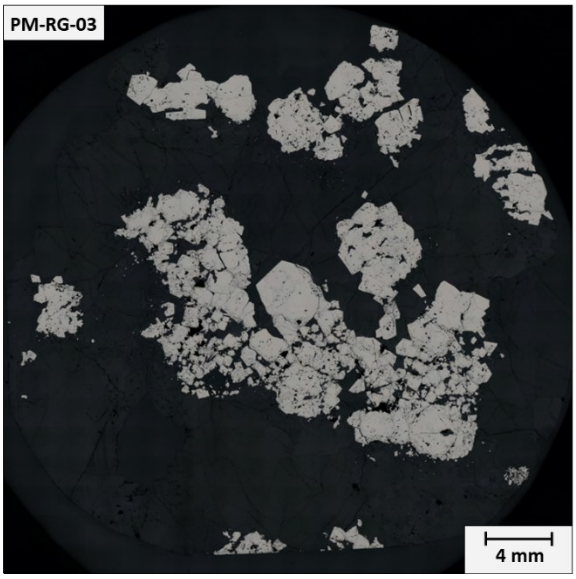
PM-RG-03
4 mm

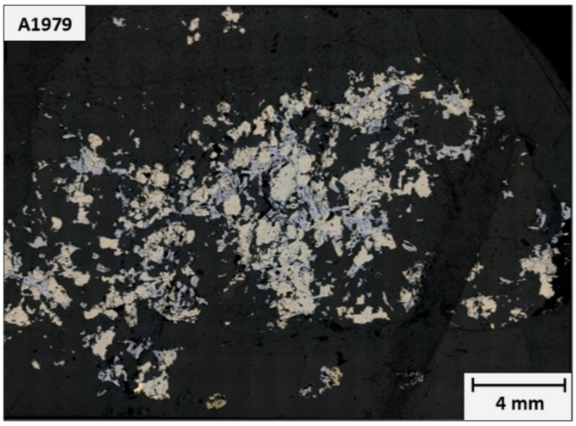
A1979
4 mm

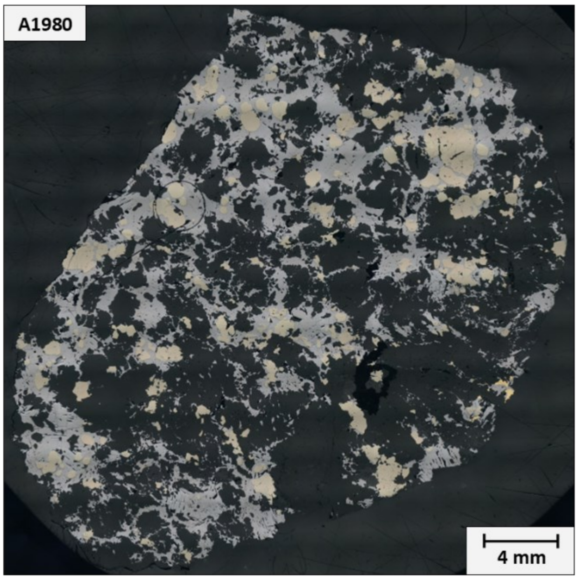
A1980
4 mm